

BANDPASS DEPENDENCE OF X-RAY TEMPERATURES IN GALAXY CLUSTERS

KENNETH W. CAVAGNOLO^{1,2}, MEGAN DONAHUE¹, G. MARK VOIT¹, AND MING SUN¹

(Accepted March 26, 2008)

ABSTRACT

We explore the band dependence of the inferred X-ray temperature of the intracluster medium (ICM) for 192 well-observed galaxy clusters selected from the *Chandra* Data Archive. If the hot ICM is nearly isothermal in the projected region of interest, the X-ray temperature inferred from a broad-band (0.7-7.0 keV) spectrum should be identical to the X-ray temperature inferred from a hard-band (2.0-7.0 keV) spectrum. However, if unresolved cool lumps of gas are contributing soft X-ray emission, the temperature of a best-fit single-component thermal model will be cooler for the broad-band spectrum than for the hard-band spectrum. Using this difference as a diagnostic, the ratio of best-fitting hard-band and broad-band temperatures may indicate the presence of cooler gas even when the X-ray spectrum itself may not have sufficient signal-to-noise to resolve multiple temperature components. To test this possible diagnostic, we extract X-ray spectra from core-excised annular regions for each cluster in our archival sample. We compare the X-ray temperatures inferred from single-temperature fits when the energy range of the fit is 0.7-7.0 keV (broad) and when the energy range is 2.0/(1+z)-7.0 keV (hard). We find that the hard-band temperature is significantly higher, on average, than the broad-band temperature. Upon further exploration, we find this temperature ratio is enhanced preferentially for clusters which are known merging systems. In addition, cool-core clusters tend to have best-fit hard-band temperatures that are in closer agreement with their best-fit broad-band temperatures. We show, using simulated spectra, that this diagnostic is sensitive to secondary cool components ($T_X = 0.5 - 3.0$ keV) with emission measures $\geq 10 - 30\%$ of the primary hot component.

Subject headings: catalogs – galaxies: clusters: general – X-rays: galaxies: clusters – cosmology: observations – methods: data analysis

1. INTRODUCTION

The normalization, shape, and evolution of the cluster mass function are useful for measuring cosmological parameters (e.g. Evrard 1989; Wang & Steinhardt 1998; Haiman et al. 2001; Wang et al. 2004). In particular, the evolution of large scale structure formation provides a complementary and distinct constraint on cosmological parameters to those tests which constrain them geometrically, such as supernovae (Riess et al. 1998, 2007) and baryon acoustic oscillations (Eisenstein et al. 2005). However, clusters are a useful cosmological tool only if we can infer cluster masses from observable properties such as X-ray luminosity, X-ray temperature, lensing shear, optical luminosity, or galaxy velocity dispersion. Empirically, the correlation of mass to these observable properties is well-established (see Voit (2005) for a review). But, there is non-negligible scatter in mass-observable scaling relations which must be accounted for if clusters are to serve as high-precision mass proxies necessary for using clusters to study cosmological parameters such as the dark energy equation of state. However, if we could identify a “2nd parameter” – possibly reflecting the degree of relaxation in the cluster – we could improve the utility of clusters as cosmological probes by parameterizing and reducing the scatter in mass-observable scaling relations.

Toward this end, we desire to quantify the dynamical state of a cluster beyond simply identifying which clusters appear relaxed and those which do not. Most clusters are likely to have a dynamical state which is somewhere in between (O’Hara et al. 2006; Kravtsov et al. 2006; Ventimiglia et al. 2008). The degree to which a cluster is virialized must first

be quantified within simulations that correctly predict the observable properties of the cluster. Then, predictions for quantifying cluster virialization may be tested, and possibly calibrated, with observations of an unbiased sample of clusters (e.g. REXCESS sample of Böhringer et al. 2007).

One study that examined how relaxation might affect the observable properties of clusters was conducted by Mathiesen & Evrard 2001 (hereafter ME01) using the ensemble of simulations by Mohr & Evrard 1997. ME01 found that most clusters which had experienced a recent merger were cooler than the cluster mass-observable scaling relations predicted. They attributed this to the presence of cool, spectroscopically unresolved accreting subclusters which introduce energy into the ICM and have a long timescale for dissipation. The consequence was an under-prediction of cluster binding masses of 15 – 30% (Mathiesen & Evrard 2001). It is important to note that the simulations of Mohr & Evrard (1997) included only gravitational processes. The intervening years have proven that radiative cooling is tremendously important in shaping the global properties of clusters (e.g. McCarthy et al. 2004, Poole et al. 2006, or Nagai et al. 2007). Therefore, the magnitude of the effect seen by ME01 could be somewhat different if radiative processes are included.

One empirical observational method of quantifying the degree of cluster relaxation involves using ICM substructure and employs the power in ratios of X-ray surface brightness moments (Buote & Tsai 1995, 1996; Jeltima et al. 2005). Although an excellent tool, power ratios suffer from being aspect-dependent (Jeltima et al. 2007; Ventimiglia et al. 2008). The work of ME01 suggested a complementary measure of substructure which does not depend on projected perspective. In their analysis, they found hard-band (2.0-9.0 keV) temperatures were $\sim 20\%$ hotter than broad-band (0.5-9.0 keV) temperatures. Their interpretation was that the cooler

¹ Michigan State University, Department of Physics and Astronomy, BPS Building, East Lansing, MI 48824

² cavagnolo@pa.msu.edu

broad-band temperature is the result of unresolved accreting cool subclusters which are contributing significant amounts of line emission to the soft band ($E < 2$ keV). This effect has been studied and confirmed by Mazzotta et al. (2004) and Vikhlinin (2006) using simulated *Chandra* and *XMM-Newton* spectra.

ME01 suggested that this temperature skewing, and consequently the fingerprint of mergers, could be detected utilizing the energy resolution and soft-band sensitivity of *Chandra*. They proposed selecting a large sample of clusters covering a broad dynamical range, fitting a single-component temperature to the hard-band and broad-band, and then checking for a net skew above unity in the hard-band to broad-band temperature ratio. In this paper we present the findings of just such a temperature-ratio test using *Chandra* archival data. We find the hard-band temperature exceeds the broad-band temperature, on average, by $\sim 16\%$ in multiple flux-limited samples of X-ray clusters from the *Chandra* archive. This mean excess is weaker than the 20% predicted by ME01, but is significant at the 12σ level nonetheless. Hereafter, we refer to the hard-band to broad-band temperature ratio as T_{HBR} . We also find that non-cool core systems and mergers tend to have higher values of T_{HBR} . Our findings suggest that T_{HBR} is an indicator of a cluster's temporal proximity to the most recent merger event.

This paper proceeds in the following manner: In §2 we outline sample-selection criteria and *Chandra* observations selected under these criteria. Data reduction and handling of the X-ray background is discussed in §3. Spectral extraction is discussed in §4, while fitting and simulated spectra are discussed in §5. Results and discussion of our analysis are presented in §6. A summary of our work is presented in §7. For this work we have assumed a flat Λ CDM Universe with cosmology $\Omega_M = 0.3$, $\Omega_\Lambda = 0.7$, and $H_0 = 70$ km s $^{-1}$ Mpc $^{-1}$. All quoted uncertainties are at the 1.6σ level (90% confidence).

2. SAMPLE SELECTION

Our sample was selected from observations publicly available in the *Chandra* X-ray Telescope's Data Archive (CDA). Our initial selection pass came from the *ROSAT* Brightest Cluster Sample (Ebeling et al. 1998), RBC Extended Sample (Ebeling et al. 2000), and *ROSAT* Brightest 55 Sample (Edge et al. 1990; Peres et al. 1998). The portion of our sample at $z \gtrsim 0.4$ can also be found in a combination of the *Einstein* Extended Medium Sensitivity Survey (Gioia et al. 1990), North Ecliptic Pole Survey (Henry et al. 2006), *ROSAT* Deep Cluster Survey (Rosati et al. 1995), *ROSAT* Serendipitous Survey (Vikhlinin et al. 1998), and Massive Cluster Survey (Ebeling et al. 2001). We later extended our sample to include clusters found in the REFLEX Survey (Böhringer et al. 2004). Once we had a master list of possible targets, we cross-referenced this list with the CDA and gathered observations where a minimum of R_{5000} (defined below) is fully within the CCD field of view.

R_{Δ_c} is defined as the radius at which the average cluster density is Δ_c times the critical density of the Universe, $\rho_c = 3H(z)^2/8\pi G$. For our calculations of R_{Δ_c} we adopt the relation from Arnaud et al. (2002):

$$R_{\Delta_c} = 2.71 \text{ Mpc } \beta_T^{1/2} \Delta_c^{-1/2} (1+z)^{-3/2} \left(\frac{kT_X}{10 \text{ keV}} \right)^{1/2} \quad (1)$$

$$\Delta_z = \frac{\Delta_c \Omega_M}{18\pi^2 \Omega_z}$$

$$\Omega_z = \frac{\Omega_M(1+z)^3}{[\Omega_M(1+z)^3] + [(1-\Omega_M-\Omega_\Lambda)(1+z)^2] + \Omega_\Lambda}$$

where R_{Δ_c} is in units of h_{70}^{-1} , Δ_c is the assumed density contrast of the cluster at R_{Δ_c} , and β_T is a numerically determined, cosmology-independent ($\lesssim \pm 20\%$) normalization for the virial relation $GM/2R = \beta_T kT_{vir}$. We use $\beta_T = 1.05$ taken from Evrard et al. (1996).

The result of our CDA search was a total of 374 observations of which we used 244 for 202 clusters. The clusters making up our sample cover a redshift range of $z = 0.045 - 1.24$, a temperature range of $T_X = 2.6 - 19.2$ keV, and bolometric luminosities of $L_{bol} = 0.12 - 100.4 \times 10^{44}$ ergs s $^{-1}$. The bolometric ($E = 0.1 - 100$ keV) luminosities for our sample clusters plotted as a function of redshift are shown in Figure 1. These L_{bol} values are calculated from our best-fit spectral models and are limited to the region of the spectral extraction (from $R = 70$ kpc to $R = R_{2500}$, or R_{5000} in the cases where no R_{2500} fit was possible). Basic properties of our sample are listed in Table 1.

For the sole purpose of defining extraction regions based on fixed overdensities as discussed in §4, fiducial temperatures (measured with *ASCA*) and redshifts were taken from the Ph.D. thesis of Don Horner³ (all redshifts confirmed with NED⁴). We will show later that the *ASCA* temperatures are sufficiently close to the *Chandra* temperatures such that R_{Δ_c} is reliably estimated to within 20%. Note that R_{Δ_c} is proportional to $T^{1/2}$, so that a 20% error in the temperature leads to only a 10% error in R_{Δ_c} , which in turn has no detectable effect on our final results. For clusters not listed in Horner's thesis, we used a literature search to find previously measured temperatures. If no published value could be located, we measured the global temperature by recursively extracting a spectrum in the region $0.1 < r < 0.2R_{500}$ fitting a temperature and recalculating R_{500} . This process was repeated until three consecutive iterations produced R_{500} values which differed by $\leq 1\sigma$. This method of temperature determination has been employed in other studies, see Sanderson et al. (2006) and Henry et al. (2006) as examples.

3. CHANDRA DATA

3.1. Reprocessing and Reduction

All datasets were reduced utilizing the *Chandra* Interactive Analysis of Observations package (CIAO) and accompanying Calibration Database (CALDB). Using CIAO v3.3.0.1 and CALDB v3.2.2, standard data analysis was followed for each observation to apply the most up-to-date time-dependent gain correction and when appropriate, charge transfer inefficiency correction (Townsend et al. 2000).

Point sources were identified in an exposure-corrected events file using the adaptive wavelet tool WAVDETECT (Freeman et al. 2002). A 2σ region surrounding each point source was automatically output by WAVDETECT to define an exclusion mask. All point sources were then visually confirmed and we added regions for point sources which were missed by WAVDETECT and deleted regions for spuriously detected "sources". Spurious sources are typically faint CCD features (chip gaps and chip edges) not fully removed after dividing by the exposure map. This process resulted in an events file (at "level 2") that has been cleaned of point sources.

³ <http://asd.gsfc.nasa.gov/Donald.Horner/thesis.html>

⁴ <http://nedwww.ipac.caltech.edu/>

To check for contamination from background flares or periods of excessively high background, light curve analysis was performed using Maxim Markevitch’s contributed CIAO script `LC_CLEAN.SL`⁵. Periods with count rates $\geq 3\sigma$ and/or a factor ≥ 1.2 of the mean background level of the observation were removed from the good time interval file. As prescribed by Markevitch’s cookbook⁶, ACIS front-illuminated (FI) chips were analyzed in the 0.3–12.0 keV range, and the 2.5–7.0 keV energy range for the ACIS back-illuminated (BI) chips.

When a FI and BI chip were both active during an observation, we compared light curves from both chips to detect long duration, soft-flares which can go undetected on the FI chips but show up on the BI chips. While rare, this class of flare must be filtered out of the data, as it introduces a spectral component which artificially increases the best-fit temperature via a high energy tail. We find evidence for a long duration soft flare in the observations of Abell 1758 (David & Kempner 2004), CL J2302.8+0844, and IRAS 09104+4109. These flares were handled by removing the time period of the flare from the GTI file.

Defining the cluster “center” is essential for the later purpose of excluding cool cores from our spectral analysis (see §4). To determine the cluster center, we calculated the centroid of the flare cleaned, point-source free level-2 events file filtered to include only photons in the 0.7–7.0 keV range. Before centroiding, the events file was exposure-corrected and “holes” created by excluding point sources were filled using interpolated values taken from a narrow annular region just outside the hole (holes are not filled during spectral extraction discussed in §4). Prior to centroiding, we defined the emission peak by heavily binning the image, finding the peak value within a circular region extending from the peak to the chip edge (defined by the radius R_{max}), reducing R_{max} by 5%, reducing the binning by a factor of two, and finding the peak again. This process was repeated until the image was unbinned (binning factor of one). We then returned to an unbinned image with an aperture centered on the emission peak with a radius R_{max} and found the centroid using CIAO’s `DMSTAT`. The centroid, (x_c, y_c) , for a distribution of N good pixels with coordinates (x_i, y_i) and values $f(x_i, y_i)$ is defined as:

$$Q = \sum_{i,j=1}^N f(x_i, y_i) \quad (2)$$

$$x_c = \frac{\sum_{i,j=1}^N x_i \cdot f(x_i, y_i)}{Q}$$

$$y_c = \frac{\sum_{i,j=1}^N y_i \cdot f(x_i, y_i)}{Q}.$$

If the centroid was within 70 kpc of the emission peak, the emission peak was selected as the center, otherwise the centroid was used as the center. This selection was made to ensure all “peaky” cool cores coincided with the cluster center, thus maximizing their exclusion later in our analysis. All cluster centers were additionally verified by eye.

3.2. X-ray Background

Because we measured a global cluster temperature, specifically looking for a temperature ratio shift in energy bands

which can be contaminated by the high-energy particle background or the soft local background, it was important to carefully analyze the background and subtract it from our source spectra. Below we outline three steps taken in handling the background: customization of blank-sky backgrounds, re-normalization of these backgrounds for variation of hard-particle count rates, and fitting of soft background residuals.

We used the blank-sky observations of the X-ray background from Markevitch et al. (2001) and supplied within the CXC CALDB. First, we compared the flux from the diffuse soft X-ray background of the *ROSAT* All-Sky Survey (*RASS*) combined bands *R12*, *R45*, and *R67* to the 0.7–2.0 keV flux in each extraction aperture for each observation. *RASS* combined bands give fluxes for energy ranges of 0.12–0.28 keV, 0.47–1.21 keV, and 0.76–2.04 keV respectively corresponding to *R12*, *R45*, and *R67*. For the purpose of simplifying subsequent analysis, we discarded observations with an *R45* flux $\geq 10\%$ of the total cluster X-ray flux.

The appropriate blank-sky dataset for each observation was selected from the CALDB, reprocessed exactly as the observation was, and then reprojected using the aspect solutions provided with each observation. For observations on the ACIS-I array, we reprojected blank-sky backgrounds for chips I0–I3 plus chips S2 and/or S3. For ACIS-S observations, we created blank-sky backgrounds for the target chip, plus chips I2 and/or I3. The additional off-aimpoint chips were included only if they were active during the observation and had available blank-sky data sets for the observation time period. Off-aimpoint chips were cleaned for point sources and diffuse sources using the method outlined in §3.1.

The additional off-aimpoint chips were included in data reduction since they contain data which is farther from the cluster center and are therefore more useful in analyzing the observation background. For observations which did not have a matching off-aimpoint blank-sky background, a source-free region of the active chips is located and used for background normalization. To normalize the hard particle component we measured fluxes for identical regions in the blank-sky field and target field in the 9.5–12.0 keV range. The effective area of the ACIS arrays above 9.5 keV is approximately zero, and thus the collected photons there are exclusively from the particle background.

A histogram of the ratios of the 9.5–12.0 keV count rate from an observation’s off-aimpoint chip to that of the observation specific blank-sky background are presented in Figure 2. The majority of the observations are in agreement to $\lesssim 20\%$ of the blank-sky background rate, which is small enough to not affect our analysis. Even so, we re-normalized all blank-sky backgrounds to match the observed background.

Normalization brings the observation background and blank-sky background into agreement for $E > 2$ keV, but even after normalization, typically, there may exist a soft excess/deficit associated with the spatially varying soft Galactic background. Following the technique detailed in Vikhlinin et al. (2005), we constructed and fit soft residuals for this component. For each observation we subtracted a spectrum of the blank-sky field from a spectrum of the off-aimpoint field to create a soft residual. The residual was fit with a solar abundance, zero-redshift MEKAL model (Mewe et al. 1985, 1986; Kaastra 1992; Liedahl et al. 1995) where the normalization was allowed to be negative. The resulting best-fit temperatures for all of the soft residuals identified here were between 0.2–1.0 keV, which is in agreement with results of Vikhlinin et al. (2005). The model normal-

⁵ <http://cxc.harvard.edu/contrib/maxim/acisbg/>

⁶ <http://cxc.harvard.edu/contrib/maxim/acisbg/COOKBOOK>

ization of this background component was then scaled to the cluster sky area. The re-scaled component was included as a fixed background component during fitting of a cluster's spectra.

4. SPECTRAL EXTRACTION

The simulated spectra calculated by ME01 were analyzed in a broad energy band of 0.5–9.0 keV and a hard energy band of 2.0_{rest}–9.0 keV, but to make a reliable comparison with *Chandra* data we used narrower energy ranges of 0.7–7.0 keV for the broad energy band and 2.0_{rest}–7.0 keV for the hard energy band. We excluded data below 0.7 keV to avoid the effective area and quantum efficiency variations of the ACIS detectors, and excluded energies above 7.0 keV in which diffuse source emission is dominated by the background and where *Chandra*'s effective area is small. We also accounted for cosmic redshift by shifting the lower energy boundary of the hard-band from 2.0 keV to 2.0/(1+z) keV (henceforth, the 2.0 keV cut is in the rest frame).

ME01 calculated the relation between $T_{0.5-9.0}$ and $T_{2.0-9.0}$ using apertures of R_{200} and R_{500} in size. While it is trivial to calculate a temperature out to R_{200} or R_{500} for a simulation, such a measurement at these scales is extremely difficult with *Chandra* observations (see Vikhlinin et al. (2005) for a detailed example). Thus, we chose to extract spectra from regions with radius R_{5000} , and R_{2500} when possible. Clusters analyzed only within R_{5000} are denoted in Table 1 by a double dagger (‡).

The cores of some clusters are dominated by gas at $\lesssim T_{\text{virial}}/2$ which can greatly affect the global best-fit temperature; therefore, we excised the central 70 kpc of each aperture. These excised apertures are denoted by “-CORE” in the text. Recent work by Maughan (2007) has shown excising 0.15 R_{500} rather than a static 70 kpc reduces scatter in mass-observable scaling relations. However, our smaller excised region seems sufficient for this investigation because for cool core clusters the average radial temperature at $r > 70$ kpc is approximately isothermal (Vikhlinin et al. 2005). Indeed, we find that cool core clusters have smaller than average T_{HBR} when the 70 kpc region has been excised (§6.3.1).

Although some clusters are not circular in projection, but rather are elliptical or asymmetric, we found that assuming spherical symmetry and extracting spectra from a circular annulus did not significantly change the best-fit values. For another such example see Bauer et al. (2005).

After defining annular apertures, we extracted source spectra from the target cluster and background spectra from the corresponding normalized blank-sky dataset. By standard CIAO means we created weighted effective area functions (WARFs) and redistribution matrices (WRMFs) for each cluster using a flux-weighted map (WMAP) across the entire extraction region. The WMAP was calculated over the energy range 0.3–2.0 keV to weight calibrations that vary as a function of position on the chip. The CCD characteristics which affect the analysis of extended sources, such as energy dependent vignetting, are contained within these files. Each spectrum was then binned to contain a minimum of 25 counts per channel.

5. SPECTRAL ANALYSIS

5.1. Fitting

Spectra were fit with XSPEC 11.3.2AG (Arnaud 1996) using a single-temperature MEKAL model in combination with the photoelectric absorption model WABS

(Morrison & McCammon 1983) to account for Galactic absorption. Galactic absorption values, N_{HI} , are taken from Dickey & Lockman (1990). The potentially free parameters of the absorbed thermal model are N_{HI} , X-ray temperature (T_X), metal abundance normalized to solar (elemental ratios taken from Anders & Grevesse 1989), and a normalization proportional to the integrated emission measure of the cluster. Results from the fitting are presented in Tables 5 and 6. No systematic error is added during fitting, and thus all quoted errors are statistical only. The statistic used during fitting was χ^2 (XSPEC statistics package CH1). Every cluster analyzed was found to have greater than 1500 background-subtracted source counts in the spectrum.

For some clusters, more than one observation was available in the archive. We utilized the power of the combined exposure time by first extracting independent spectra, WARFs, WRMFs, normalized background spectra, and soft residuals for each observation. Then, these independent spectra were read into XSPEC simultaneously and fit with one spectral model which had all parameters, except normalization, tied among the spectra. The simultaneous fit is what is reported for these clusters, denoted by a star (*), in Tables 5 and 6.

Additional statistical error was introduced into the fits because of uncertainty associated with the soft local background component discussed in §3.2. To estimate the sensitivity of our best-fit temperatures to this uncertainty, we used the differences between T_X for a model using the best-fit soft background normalization and T_X for models using $\pm 1\sigma$ of the soft background normalization. The statistical uncertainty of the original fit and the additional uncertainty inferred from the range of normalizations to the soft X-ray background component were then added in quadrature to produce a final error. In all cases this additional background error on the temperature was less than 10% of the total statistical error, and therefore represents a minor inflation of the error budget.

When comparing fits with fixed Galactic column density with those where it was a free parameter, we found that neither the goodness of fit per free parameter nor the best-fit T_X were significantly different. Thus, N_{HI} was fixed at the Galactic value with the exception of three cases: Abell 399 (Sakelliou & Ponman 2004), Abell 520, and Hercules A. For these three clusters N_{HI} is a free parameter. In all fits, the metal abundance was a free parameter.

After fitting we rejected several datasets as their best-fit $T_{2.0-7.0}$ had no upper bound in the 90% confidence interval and thus were insufficient for our analysis. All fits for the clusters Abell 781, Abell 1682, CL J1213+0253, CL J1641+4001, IRAS 09104+4109, Lynx E, MACS J1824.3+4309, MS 0302.7+1658, and RX J1053+5735 were rejected. We also removed Abell 2550 from our sample after finding it to be an anomalously cool ($T_X \sim 2$ keV) “cluster”. In fact, Abell 2550 is a line-of-sight set of groups, as discussed by Martini et al. (2004). After these rejections, we are left with a final sample of 166 clusters which have R_{2500} -CORE fits and 192 clusters which have R_{5000} -CORE fits.

5.2. Simulated Spectra

To quantify the effect a second, cooler gas component would have on the fit of a single-component spectral model, we created an ensemble of simulated spectra for each real spectrum in our entire sample using XSPEC. With these simulated spectra we sought to answer the question: Given the count level in each observation of our sample, how bright must a second temperature component be for it to affect the

observed temperature ratio? Put another way, we asked at what flux ratio a second gas phase produces a temperature ratio, T_{HBR} , of greater than unity with 90% confidence.

We began by adding the observation-specific background to a convolved, absorbed thermal model with two temperature components observed for a time period equal to the actual observation's exposure time and adding Poisson noise. For each realization of an observation's simulated spectrum, we defined the primary component to have the best-fit temperature and metallicity of the $R_{2500-CORE}$ 0.7-7.0 keV fit, or $R_{5000-CORE}$ if no $R_{2500-CORE}$ fit was performed. We then incremented the secondary component temperature over the values 0.5, 0.75, 1.0, 2.0, and 3.0 keV. The metallicity of the secondary component was fixed and set equal to the metallicity of the primary component.

We adjusted the normalization of the simulated two-component spectra to achieve equivalent count rates to those in the real spectra. The sum of normalizations can be expressed as $N = N_1 + \xi \cdot N_2$. We set the secondary component normalization to $N_2 = \xi \cdot N_{bf}$ where N_{bf} is the best-fit normalization of the appropriate 0.7-7.0 keV fit and ξ is a preset factor taking the values 0.4, 0.3, 0.2, 0.15, 0.1, and 0.05. The primary component normalization, N_1 , was determined through an iterative process to make real and simulated spectral count rates match. The parameter ξ therefore represents the fractional contribution of the cooler component to the overall count rate.

There are many systematics at work in the full ensemble of observation specific simulated spectra, such as redshift, column density, and metal abundance. Thus as a further check of spectral sensitivity to the presence of a second gas phase, we simulated additional spectra for the case of an idealized observation. We followed a similar procedure to that outlined above, but in this instance we used a finer temperature and ξ grid of $T_2 = 0.5 \rightarrow 3.0$ in steps of 0.25 keV, and $\xi = 0.02 \rightarrow 0.4$ in steps of 0.02. The input spectral model was $N_{HI} = 3.0 \times 10^{20} \text{ cm}^{-2}$, $T_1 = 5 \text{ keV}$, $Z/Z_\odot = 0.3$ and $z = 0.1$. We also varied the exposure times such that the total number of counts in the 0.7-7.0 keV band was 15K, 30K, 60K, or 120K. For these spectra we used the on-axis sample response files provided to Cycle 10 proposers⁷. Poisson noise is added, but no background is considered.

We also simulated a control sample of single-temperature models. The control sample is simply a simulated version of the best-fit model. This control provides us with a statistical test of how often the actual hard-component temperature might differ from a broad-band temperature fit if calibration effects are under control. Fits for the control sample are shown in the far right panels of Figure 3.

For each observation, we have 65 total simulated spectra: 35 single-temperature control spectra and 30 two-component simulated spectra (five second temperatures, each with six different ξ). Our resulting ensemble of simulated spectra contains 12,765 spectra. After generating all the spectra we followed the same fitting routine detailed in §5.1.

With the ensemble of simulated spectra we then asked the question: for each T_2 and ΔT_X (defined as the difference between the primary and secondary temperature components) what is the minimum value of ξ , called ξ_{min} , that produces $T_{HBR} \geq 1.1$ at 90% confidence? From our analysis of these simulated spectra we have found these important results:

1. In the control sample, a single-temperature model rarely ($\sim 2\%$ of the time) gives a significantly different $T_{0.7-7.0}$ and $T_{2.0-7.0}$. The weighted average (right panels of Fig. 3) for the control sample is 1.002 ± 0.001 and the standard deviation is ± 0.044 . The T_{HBR} distribution for the control sample appears to have an intrinsic width which is likely associated with statistical noise of fitting in XSPEC (Dupke, private communication). This result indicates that our remaining set of observations is statistically sound, e.g. our finding that T_{HBR} significantly differs from 1.0 cannot result from statistical fluctuations alone.
2. Shown in Table 2 are the contributions a second cooler component must make in the case of the idealized spectra in order to produce $T_{HBR} \geq 1.1$ at 90% confidence. In general, the contribution of cooler gas must be $> 10\%$ for $T_2 < 2 \text{ keV}$ to produce T_{HBR} as large as 1.1. The increase in percentages at $T_2 < 1.0 \text{ keV}$ is owing to the energy band we consider (0.7-7.0 keV) as gas cooler than 0.7 keV must be brighter than at 1.0 keV in order to make an equivalent contribution to the soft end of the spectrum at 0.7 keV.
3. In the full ensemble of observation-specific simulated spectra, we find a great deal of statistical scatter in ξ_{min} at any given ΔT_X . This was expected as the full ensemble is a superposition of spectra with a broad range of total counts, N_{HI} , redshifts, abundance, and backgrounds. But using the idealized simulated spectra as a guide, we find for those spectra with $N_{counts} \gtrsim 15000$, producing $T_{HBR} \geq 1.1$ at 90% confidence again requires the cooler gas to be contributing $> 10\%$ of the emission. These results are also summarized in Table 2. The good agreement between the idealized and observation-specific simulated spectra indicates that while many more factors are in play for the observation-specific spectra, they do not degrade our ability to reliably measure $T_{HBR} > 1.1$. The trend here of a common soft component sufficient to change the temperature measurement in a single-temperature model is statistical, a result that comes from an aggregate view of the sample rather than any individual fit.
4. As redshift increases, gas cooler than 1.0 keV is slowly redshifted out of the observable X-ray band. As expected, we find from our simulated spectra that for $z \geq 0.6$, T_{HBR} is no longer statistically distinguishable from unity. In addition, the $T_{2.0-7.0}$ lower boundary nears convergence with the $T_{0.7-7.0}$ lower boundary as z increases, and for $z = 0.6$, the hard-band lower limit is 1.25 keV, while at the highest redshift considered, $z = 1.2$, the hard-band lower limit is only 0.91 keV. For the 14 clusters with $z \geq 0.6$ in our real sample we are most likely underestimating the actual amount of temperature inhomogeneity. We have tested the effect of excluding these clusters on our results, and find a negligible change in the overall skew of T_{HBR} to greater than unity.

6. RESULTS AND DISCUSSION

6.1. Temperature Ratios

For each cluster we have measured a ratio of the hard-band to broad-band temperature defined as $T_{HBR} = T_{2.0-7.0}/T_{0.7-7.0}$.

⁷ http://cxc.harvard.edu/caldb/prop_plan/imaging/index.html

We find that the mean T_{HBR} for our entire sample is greater than unity at more than 12σ significance. The weighted mean values for our sample are shown in Table 3. Presented in Figure 3 are the binned weighted means and raw T_{HBR} values for $R_{2500-CORE}$, $R_{5000-CORE}$, and the simulated control sample. The peculiar points with $T_{HBR} < 1$ are all statistically consistent with unity. The presence of clusters with $T_{HBR} = 1$ suggests that systematic calibration uncertainties are not the sole reason for deviations of T_{HBR} from 1. We also find that the temperature ratio does not depend on the best-fit broad-band temperature, and that the observed dispersion of T_{HBR} is greater than the predicted dispersion arising from systematic uncertainties.

The uncertainty associated with each value of T_{HBR} is dominated by the larger error in $T_{2.0-7.0}$, and on average, $\Delta T_{2.0-7.0} \approx 2.3 \Delta T_{0.7-7.0}$. This error interval discrepancy naturally results from excluding the bulk of a cluster’s emission which occurs below 2 keV. While choosing a temperature-sensitive cut-off energy for the hard-band (other than 2.0 keV) might maintain a more consistent error budget across our sample, we do not find any systematic trend in T_{HBR} or the associated errors with cluster temperature.

6.2. Systematics

In this study we have found the average value of T_{HBR} is significantly greater than one and that $\sigma_{HBR} > \sigma_{control}$, with the latter result being robust against systematic uncertainties. As predicted by ME01, both of these results are expected to arise naturally from the hierarchical formation of clusters. But systematic uncertainty related to *Chandra* instrumentation or other sources could shift the average value of T_{HBR} one would get from “perfect” data. In this section we consider some additional sources of uncertainty.

First, the disagreement between *XMM-Newton* and *Chandra* cluster temperatures has been noted in several independent studies, i.e. Vikhlinin et al. (2005) and Snowden et al. (2007). But the source of this discrepancy is not well understood and efforts to perform cross-calibration between *XMM-Newton* and *Chandra* have thus far not been conclusive. One possible explanation is poor calibration of *Chandra* at soft X-ray energies which may arise from a hydrocarbon contaminant on the High Resolution Mirror Assembly (HRMA) similar in nature to the contaminant on the ACIS detectors (Marshall et al. 2004). We have assessed this possibility by looking for systematic trends in T_{HBR} with time or temperature, as such a contaminant would most likely have a temperature and/or time dependence.

As noted in §6.1 and seen in Figure 3, we find no systematic trend with temperature either for the full sample or for a sub-sample of single-observation clusters with $> 75\%$ of the observed flux attributable to the source (higher signal-to-noise observations will be more affected by calibration uncertainty). Plotted in the lower-left pane of Figures 4 and 5 is T_{HBR} versus time for single observation clusters (clusters with multiple observations are fit simultaneously and any time effect would be washed out) where the spectral flux is $> 75\%$ from the source. We find no significant systematic trend in T_{HBR} with time, which suggests that if T_{HBR} is affected by any contamination of *Chandra*’s HRMA, then the contaminant is most likely not changing with time. Our conclusion on this matter is that the soft calibration uncertainty is not playing a dominant role in our results.

Aside from instrumental and calibration effects, some other possible sources of systematic error are signal-to-noise (S/N),

redshift selection, Galactic absorption, and metallicity. Also presented in Figures 4 and 5 are three of these parameters versus T_{HBR} for $R_{2500-CORE}$ and $R_{5000-CORE}$, respectively. The trend in T_{HBR} with redshift is expected as the $2.0/(1+z)$ keV hard-band lower boundary nears convergence with the 0.7 keV broad-band lower boundary at $z \approx 1.85$. We find no systematic trends of T_{HBR} with S/N or Galactic absorption, which might occur if the skew in T_{HBR} were a consequence of poor count statistics, inaccurate Galactic absorption, or very poor calibration. In addition, the ratio of T_{HBR} for $R_{2500-CORE}$ to $R_{5000-CORE}$ for every cluster in our sample does not significantly deviate from unity. Our results are robust to changes in aperture size.

Also shown in Figures 4 and 5 are the ratios of *ASCA* temperatures taken from Don Horner’s thesis to *Chandra* temperatures derived in this work. The spurious point below 0.5 with very large error bars is MS 2053.7-0449, which has a poorly constrained *ASCA* temperature of $10.03^{+8.73}_{-3.52}$. Our value of ~ 3.5 keV for this cluster is in agreement with the recent work of Maughan et al. (2007). Not all our sample clusters have an *ASCA* temperature, but a sufficient number (53) are available to make this comparison reliable. Apertures used in the extraction of *ASCA* spectra had no core region removed and were substantially larger than R_{2500} . *ASCA* spectra were also fit over a broader energy range (0.6-10 keV) than we use here. Nonetheless, our temperatures are in good agreement with those from *ASCA*, but we do note a trend of comparatively hotter *Chandra* temperatures for $T_{Chandra} > 10$ keV. For both apertures, the clusters with $T_{Chandra} > 10$ keV are Abell 1758, Abell 2163, Abell 2255, and RX J1347.5-1145. Based on this trend, we test excluding the hottest clusters ($T_{Chandra} > 10$ keV where *ASCA* and *Chandra* disagree) from our sample. The mean temperature ratio for $R_{2500-CORE}$ remains 1.16 and the error of the mean increases from ± 0.014 to ± 0.015 , while for $R_{5000-CORE}$ T_{HBR} increases by a negligible 0.9% to 1.15 ± 0.014 . Our results are not being influenced by the inclusion of hot clusters.

The temperature range of the clusters we’ve analyzed ($T_X \sim 3 - 20$ keV) is broad enough that the effect of metal abundance on the inferred spectral temperature is clearly not negligible. In Figure 6 we have plotted T_{HBR} versus abundance in solar units. Despite covering a factor of seven in temperature and metal abundances ranging from $Z/Z_\odot \approx 0$ to solar, we find no trend in T_{HBR} with metallicity. The slight trend in the $R_{2500-CORE}$ aperture (top panel of Figure 6) is insignificant, while there is no trend at all in the control sample or $R_{5000-CORE}$ aperture.

6.3. Using T_{HBR} as a Test of Relaxation

6.3.1. Cool Core Versus Non-Cool Core

As discussed in §1, ME01 gives us reason to believe the observed skewing of T_{HBR} to greater than unity is related to the dynamical state of a cluster. It has also been suggested that the process of cluster formation and relaxation may robustly result in the formation of a cool core (Ota et al. 2006; Burns et al. 2007). Depending upon classification criteria, completeness, and possible selection biases, studies of flux-limited surveys have placed the prevalence of cool cores at 34 – 60% (White et al. 1997; Peres et al. 1998; Bauer et al. 2005; Chen et al. 2007). It has thus become rather common to divide up the cluster population into two distinct classes, cool core (CC) and non-cool core (NCC), for the purpose of discussing their different formation or merger histories. We

thus sought to identify which clusters in our sample have cool cores, which do not, and if the presence or absence of a cool core is correlated with T_{HBR} . It is very important to recall that we excluded the core during spectral extraction and analysis.

To classify the core of each cluster, we extracted a spectrum for the 50 kpc region surrounding the cluster center and then defined a temperature decrement,

$$T_{dec} = T_{50}/T_{cluster} \quad (3)$$

where T_{50} is the temperature of the inner 50 kpc and $T_{cluster}$ is either the $R_{2500-CORE}$ or $R_{5000-CORE}$ temperature. If T_{dec} was 2σ less than unity, we defined the cluster as having a CC, otherwise the cluster was defined as NCC. We find CCs in 35% of our sample and when we lessen the significance needed for CC classification from 2σ to 1σ , we find 46% of our sample clusters have CCs. It is important to note that the frequency of CCs in our study is consistent with other more detailed studies of CC/NCC populations.

When fitting for T_{50} , we altered the method outlined in §5.1 to use XSPEC's modified Cash statistic (Cash 1979), CSTAT, on ungrouped spectra. This choice was made because the distribution of counts per bin in low count spectra is not Gaussian but instead Poisson. As a result, the best-fit temperature using χ^2 is typically cooler (Nousek & Shue 1989; Balestra et al. 2007). We have explored this systematic in *all* of our fits and found it to be significant only in the lowest count spectra of the inner 50 kpc apertures discussed here. But, for consistency, we fit all inner 50 kpc spectra using the modified Cash statistic.

With each cluster core classified, we then took cuts in T_{HBR} and asked how many CC and NCC clusters were above these cuts. Figure 7 shows the normalized number of CC and NCC clusters as a function of cuts in T_{HBR} . If T_{HBR} were insensitive to the state of the cluster core, we expect, for normally distributed T_{HBR} values, to see the number of CC and NCC clusters decreasing in the same way. However, the number of CC clusters falls off more rapidly than the number of NCC clusters. If the presence of a CC is indicative of a cluster's advancement towards complete virialization, then the significantly steeper decline in the percent of CC clusters versus NCC as a function of increasing T_{HBR} indicates higher values of T_{HBR} are associated with a less relaxed state. This result is insensitive to our choice of significance level in the core classification, i.e. the result is the same whether using 1σ or 2σ significance when considering T_{dec} .

Because of the CC/NCC definition we selected, our identification of CCs and NCCs was only as robust as the errors on T_{50} allowed. One can thus ask the question, did our definition bias us towards finding more NCCs than CCs? To explore this question we simulated 20 spectra for each observation following the method outlined in §5.2 for the control sample but using the inner 50 kpc spectral best-fit values as input. For each simulated spectrum, we calculated a temperature decrement (Eqn. 3) and re-classified the cluster as having a CC or NCC. Using the new set of mock classifications we assigned a reliability factor, ψ , to each real classification, which is simply the fraction of mock classifications which agree with the real classification. A value of $\psi = 1.0$ indicates complete agreement, and $\psi = 0.0$ indicating no agreement. When we removed clusters with $\psi < 0.9$ and repeated the analysis above, we found no significant change in the trend of a steeper decrease in the relative number of CC versus NCC clusters as a function of T_{HBR} .

Recall that the coolest ICM gas is being redshifted out of

the observable band as z increases and becomes a significant effect at $z \geq 0.6$ (§5.2). Thus, we are likely not detecting "weak" CCs in the highest redshift clusters of our sample and consequently these cores are classified as NCCs and are artificially increasing the NCC population. When we excluded the 14 clusters at $z \geq 0.6$ from this portion of our analysis and repeated the calculations, we found no significant change in the results.

6.3.2. Mergers Versus Non-Mergers

Looking for a correlation between cluster relaxation and a skewing in T_{HBR} was the primary catalyst of this work. The result that increasing values of T_{HBR} are more likely to be associated with clusters harboring non-cool cores gives weight to that hypothesis. But, the simplest relation to investigate is if T_{HBR} is preferentially higher in merger systems. Thus, we now discuss clusters with the highest significant values of T_{HBR} and attempt to establish, via literature based results, the dynamic state of these systems.

The subsample of clusters on which we focus have a $T_{HBR} > 1.1$ at 90% confidence for both their $R_{2500-CORE}$ and $R_{5000-CORE}$ apertures. These clusters are listed in Table 4 and are sorted by the lower limit of T_{HBR} . The clusters with only a $R_{5000-CORE}$ analysis are listed separately at the bottom of the table. All 33 clusters listed have a core classification of $\psi > 0.9$ (see §6.3.1). The choice of the $T_{HBR} > 1.1$ threshold was arbitrary and intended to limit the number of clusters to which we pay individual attention, but which is still representative of mid- to high- T_{HBR} values. Only two clusters – Abell 697 and MACS J2049.9-3217 – do not have a $T_{HBR} > 1.1$ in one aperture and not the other. In both cases though, this was the result of the lower boundary narrowly missing the cut, but both clusters still have T_{HBR} significantly greater than unity.

For those clusters which have been individually studied, they are listed as mergers based on the conclusions of the literature authors (cited in Table 4). Many different techniques were used to determine if a system is a merger: bimodal galaxy velocity distributions, morphologies, highly asymmetric temperature distributions, ICM substructure correlated with subclusters, or disagreement of X-ray and lensing masses. From Table 4 we can see clusters exhibiting the highest significant values of T_{HBR} tend to be ongoing or recent mergers. At the 2σ level, we find increasing values of T_{HBR} favor merger systems with NCCs over relaxed, CC clusters. It appears mergers have left a spectroscopic imprint on the ICM which was predicted by ME01 and which we observe in our sample.

Of the 33 clusters with T_{HBR} significantly > 1.1 , only seven have CCs. Three of those – MKW3S, 3C 28.0, and RX J1720.1+2638 – have their apertures centered on the bright, dense cores in confirmed mergers. Two more clusters – Abell 2384 and RX J1525+0958 – while not confirmed mergers, have morphologies which are consistent with powerful ongoing mergers. Abell 2384 has a long gas tail extending toward a gaseous clump which we assume has recently passed through the cluster. RXJ1525 has a core shaped like a rounded arrowhead and is reminiscent of the bow shock seen in 1E0657-56. Abell 907 has no signs of being a merger system, but the highly compressed surface brightness contours to the west of the core are indicative of a prominent cold front, a tell-tale signature of a subcluster merger event (Markevitch & Vikhlinin 2007). Abell 2029 presents a very interesting and curious case because of its seemingly high state of relaxation and prominent cool core. There are no

complementary indications it has experienced a merger event. Yet its core hosts a wide-angle tail radio source. It has been suggested that such sources might be attributable to cluster merger activity (Sakelliou & Merrifield 2000). Moreover, the X-ray isophotes to the west of the bright, peaked core are slightly more compressed and may be an indication of past gas sloshing resulting from the merger of a small subcluster. Both of these features have been noted previously, specifically by Clarke et al. (2004, 2005). We suggest the elevated T_{HBR} value for this cluster lends more weight to the argument that A2029 has indeed experienced a merger recently, but how long ago we do not know.

The remaining systems we could not verify as mergers – RX J0439.0+0715, MACS J2243.3-0935, MACS J0547.0-3904, Zwicky 1215, MACS J2311+0338, Abell 267, and NGC 6338 – have NCCs and X-ray morphologies consistent with an ongoing or post-merger scenario. Abell 1204 shows no signs of recent or ongoing merger activity; however, it resides at the bottom of the arbitrary T_{HBR} cut, and as evidenced by Abell 401 and Abell 1689, exceptional spherical symmetry is no guarantee of relaxation. Our analysis here is partially at the mercy of morphological assessment, and only a more stringent study of a carefully selected subsample or analysis of simulated clusters can better determine how closely correlated T_{HBR} is with the timeline of merger events.

7. SUMMARY AND CONCLUSIONS

We have explored the band dependence of the inferred X-ray temperature of the ICM for 192 well-observed ($N_{counts} > 1500$) clusters of galaxies selected from the *Chandra* Data Archive.

We extracted spectra from the annulus between $R = 70$ kpc and $R = R_{2500}$, R_{5000} for each cluster. We compared the X-ray temperatures inferred for single-component fits to global spectra when the energy range of the fit was 0.7-7.0 keV (broad) and when the energy range was $2.0/(1+z)$ -7.0 keV (hard). We found that, on average, the hard-band temperature is significantly higher than the broad-band temperature. For the R_{2500} -CORE aperture we measured a weighted average of $T_{HBR} = 1.16$ with $\sigma = \pm 0.10$ and $\sigma_{mean} = \pm 0.01$ for the R_{5000} -CORE aperture, and $T_{HBR} = 1.14$ with $\sigma = \pm 0.12$ and $\sigma_{mean} = \pm 0.01$. We also found no systematic trends in the value of T_{HBR} , or the dispersion of T_{HBR} , with signal-to-noise, redshift, Galactic absorption, metallicity, observation date, or broad-band temperature.

In addition, we simulated an ensemble of 12,765 spectra which contained observation-specific and idealized two-temperature component models, plus a control sample of single-temperature models. From analysis of these simulations we found the statistical fluctuations for a single temperature model are inadequate to explain the significantly different $T_{0.7-7.0}$ and $T_{2.0-7.0}$ we measure in our sample. We also found that the observed scatter, σ_{HBR} , is consistent with the presence of unresolved cool ($T_X < 2.0$ keV) gas contributing a minimum of $> 10\%$ of the total emission. The simu-

lations also show the measured observational scatter in T_{HBR} is greater than the statistical scatter, $\sigma_{control}$. These results are consistent with the process of hierarchical cluster formation.

Upon further exploration, we found that T_{HBR} is enhanced preferentially for clusters which are known merger systems and for clusters without cool cores. Clusters with temperature decrements in their cores (known as cool-core clusters) tend to have best-fit hard-band temperatures that are consistently closer to their best-fit broad-band temperatures. The correlation of T_{HBR} with the type of cluster core is insensitive to our choice of classification scheme and is robust against redshift effects. Our results qualitatively support the finding by ME01 that the temperature ratio, T_{HBR} , might therefore be useful for statistically quantifying the degree of cluster relaxation/virialization.

An additional robust test of the ME01 finding should be made with simulations by tracking T_{HBR} during hierarchical assembly of a cluster. If T_{HBR} is tightly correlated with a cluster's degree of relaxation, then it, along with other methods of substructure measure, may provide a powerful metric for predicting (and therefore reducing) a cluster's deviation from mean mass-scaling relations. The task of reducing scatter in scaling relations will be very important if we are to reliably and accurately measure the mass of clusters.

Kenneth Cavagnolo was supported in this work by the National Aeronautics and Space Administration through *Chandra* X-ray Observatory Archive grants AR-6016X and AR-4017A, with additional support from a start-up grant for Megan Donahue from Michigan State University. Megan Donahue and Michigan State University acknowledge support from the NASA LTSA program NNG-05GD82G. Mark Voit thanks NASA for support through theory grant NNG-04GI89G. The *Chandra* X-ray Observatory Center is operated by the Smithsonian Astrophysical Observatory for and on behalf of the National Aeronautics Space Administration under contract NAS8-03060. This research has made use of software provided by the *Chandra* X-ray Center (CXC) in the application packages CIAO, CHIPS, and SHERPA. We thank Alexey Vikhlinin for helpful insight and expert advice. KWC also thanks attendees of the “Eight Years of Science with *Chandra* Calibration Workshop” for stimulating discussion regarding *XMM-Chandra* cross-calibration. KWC especially thanks Keith Arnaud for personally providing support and advice for mastering XSPEC. This research has made use of the NASA/IPAC Extragalactic Database (NED) which is operated by the Jet Propulsion Laboratory, California Institute of Technology, under contract with the National Aeronautics and Space Administration. This research has also made use of NASA's Astrophysics Data System. *ROSAT* data and software were obtained from the High Energy Astrophysics Science Archive Research Center (HEASARC), provided by NASA's Goddard Space Flight Center.

REFERENCES

- Akritas, M. G. & Bershad, M. A. 1996, *ApJ*, 470, 706
 Anders, E., & Grevesse, N. 1989, *Geochim. Cosmochim. Acta*, 53, 197
 Andersson, K. E., & Madejski, G. M. 2004, *ApJ*, 607, 190
 Arnaud, K. A. 1996, in *ASP Conf. Ser. 101: Astronomical Data Analysis Software and Systems V*, ed. G. H. Jacoby & J. Barnes, 17–+
 Arnaud, M., Aghanim, N., & Neumann, D. M. 2002, *A&A*, 389, 1
 Bagchi, J., Durret, F., Neto, G. B. L., & Paul, S. 2006, *Science*, 314, 791
 Balestra, I., Tozzi, P., Ettori, S., Rosati, P., Borgani, S., Mainieri, V., Norman, C., & Viola, M. 2007, *A&A*, 462, 429
 Barrena, R., Boschin, W., Girardi, M., & Spolaor, M. 2007, *A&A*, 467, 37
 Bauer, F. E., Fabian, A. C., Sanders, J. S., Allen, S. W., & Johnstone, R. M. 2005, *MNRAS*, 359, 1481
 Bliton, M., Rizza, E., Burns, J. O., Owen, F. N., & Ledlow, M. J. 1998, *MNRAS*, 301, 609

- Böhringer, H., Schuecker, P., Pratt, G. W., Arnaud, M., Ponman, T. J., Croston, J. H., Borgani, S., Bower, R. G., Briel, U. G., Collins, C. A., Donahue, M., Forman, W. R., Finoguenov, A., Geller, M. J., Guzzo, L., Henry, J. P., Kneissl, R., Mohr, J. J., Matsushita, K., Mullis, C. R., Ohashi, T., Pedersen, K., Pierini, D., Quintana, H., Raychaudhury, S., Reiprich, T. H., Romer, A. K., Rosati, P., Sabirli, K., Temple, R. F., Viana, P. T. P., Vikhlinin, A., Voit, G. M., & Zhang, Y.-Y. 2007, *A&A*, 469, 363
- Böhringer, H., Schuecker, P., Guzzo, L., Collins, C. A., Voges, W., Cruddace, R. G., Ortiz-Gil, A., Chincarini, G., De Grandi, S., Edge, A. C., MacGillivray, H. T., Neumann, D. M., Schindler, S., & Shaver, P. 2004, *A&A*, 425, 367
- Buote, D. A., & Tsai, J. C. 1995, *ApJ*, 452, 522
- . 1996, *ApJ*, 458, 27
- Burns, J. O., Hallman, E. J., Gantner, B., Motl, P. M., & Norman, M. L. 2007, *ArXiv e-prints*, 708
- Burns, J. O., Roettiger, K., Pinkney, J., Perley, R. A., Owen, F. N., & Voges, W. 1995, *ApJ*, 446, 583
- Cash, W. 1979, *ApJ*, 228, 939
- Chen, Y., Reiprich, T. H., Böhringer, H., Ikebe, Y., & Zhang, Y.-Y. 2007, *A&A*, 466, 805
- Clarke, T. E., Blanton, E. L., & Sarazin, C. L. 2004, *ApJ*, 616, 178
- Clarke, T. E., Blanton, E. L., & Sarazin, C. L. 2005, *X-Ray and Radio Connections*, ed. 7
- Dahle, H., Kaiser, N., Irgens, R. J., Lilje, P. B., & Maddox, S. J. 2002, *ApJS*, 139, 313
- David, L. P., & Kempner, J. 2004, *ApJ*, 613, 831
- Dickey, J. M., & Lockman, F. J. 1990, *ARA&A*, 28, 215
- Ebeling, H., Edge, A. C., Allen, S. W., Crawford, C. S., Fabian, A. C., & Huchra, J. P. 2000, *MNRAS*, 318, 333
- Ebeling, H., Edge, A. C., Böhringer, H., Allen, S. W., Crawford, C. S., Fabian, A. C., Voges, W., & Huchra, J. P. 1998, *MNRAS*, 301, 881
- Ebeling, H., Edge, A. C., & Henry, J. P. 2001, *ApJ*, 553, 668
- Edge, A. C., Stewart, G. C., Fabian, A. C., & Arnaud, K. A. 1990, *MNRAS*, 245, 559
- Eisenstein, D. J., Zehavi, I., Hogg, D. W., Scoccamarro, R., Blanton, M. R., Nichol, R. C., Scranton, R., Seo, H.-J., Tegmark, M., Zheng, Z., Anderson, S. F., Annis, J., Bahcall, N., Brinkmann, J., Burles, S., Castander, F. J., Connolly, A., Csabai, I., Doi, M., Fukugita, M., Frieman, J. A., Glazebrook, K., Gunn, J. E., Hendry, J. S., Hennessy, G., Ivezić, Z., Kent, S., Knapp, G. R., Lin, H., Loh, Y.-S., Lupton, R. H., Margon, B., McKay, T. A., Meiksin, A., Munn, J. A., Pope, A., Richmond, M. W., Schlegel, D., Schneider, D. P., Shimasaku, K., Stoughton, C., Strauss, M. A., SubbaRao, M., Szalay, A. S., Szapudi, I., Tucker, D. L., Yanny, B., & York, D. G. 2005, *ApJ*, 633, 560
- Evrard, A. E. 1989, *ApJ*, 341, L71
- Evrard, A. E., Metzler, C. A., & Navarro, J. F. 1996, *ApJ*, 469, 494
- Feretti, L., Böhringer, H., Giovannini, G., & Neumann, D. 1997, *A&A*, 317, 432
- Freeman, P. E., Kashyap, V., Rosner, R., & Lamb, D. Q. 2002, *ApJS*, 138, 185
- Gioia, I. M., Maccacaro, T., Geller, M. J., Huchra, J. P., Stocke, J., & Steiner, J. E. 1982, *ApJ*, 255, L17
- Gioia, I. M., Maccacaro, T., Schild, R. E., Wolter, A., Stocke, J. T., Morris, S. L., & Henry, J. P. 1990, *ApJS*, 72, 567
- Gioia, I. M., & Luppino, G. A. 1994, *ApJS*, 94, 583
- Girardi, M., Fadda, D., Escalera, E., Giuricin, G., Mardirossian, F., & Mezzetti, M. 1997, *ApJ*, 490, 56
- Gómez, P. L., Hughes, J. P., & Birkinshaw, M. 2000, *ApJ*, 540, 726
- Govoni, F., Taylor, G. B., Dallacasa, D., Feretti, L., & Giovannini, G. 2001, *A&A*, 379, 807
- Gutierrez, K., & Krawczynski, H. 2005, *ApJ*, 619, 161
- Haiman, Z., Mohr, J. J., & Holder, G. P. 2001, *ApJ*, 553, 545
- Hallman, E. J., & Markevitch, M. 2004, *ApJ*, 610, L81
- Henry, J. P., Mullis, C. R., Voges, W., Böhringer, H., Briel, U. G., Gioia, I. M., & Huchra, J. P. 2006, *ApJS*, 162, 304
- Jeltema, T. E., Canizares, C. R., Bautz, M. W., & Buote, D. A. 2005, *ApJ*, 624, 606
- Jeltema, T. E., Hallman, E. J., Burns, J. O., & Motl, P. M. 2007, *ArXiv e-prints*, 708
- Juett, A. M., Sarazin, C. L., Clarke, T. E., Andernach, H., Ehle, M., Fujita, Y., Kempner, J. C., Roy, A. L., Rudnick, L., & Slee, O. B. 2008, *ApJ*, 672, 138
- Kaastra, J. S. 1992
- Kempner, J. C., Sarazin, C. L., & Markevitch, M. 2003, *ApJ*, 593, 291
- Kravtsov, A. V., Vikhlinin, A., & Nagai, D. 2006, *ApJ*, 650, 128
- Krempec-Krygier, J., & Krygier, B. 1999, *Acta Astronomica*, 49, 403
- Liedahl, D. A., Osterheld, A. L., & Goldstein, W. H. 1995, *ApJ*, 438, L115
- Markevitch, M., Forman, W. R., Sarazin, C. L., & Vikhlinin, A. 1998, *ApJ*, 503, 77
- Markevitch, M., & Vikhlinin, A. 2007, *Phys. Rep.*, 443, 1
- Markevitch, M., Vikhlinin, A., & Mazzotta, P. 2001, *ApJ*, 562, L153
- Markevitch, M. L., Sarazin, C. L., & Irwin, J. A. 1996, *ApJ*, 472, L17+
- Marshall, H. L., Tennant, A., Grant, C. E., Hitchcock, A. P., O'Dell, S. L., & Plucinsky, P. P. 2004, in *Presented at the Society of Photo-Optical Instrumentation Engineers (SPIE) Conference*, Vol. 5165, *X-Ray and Gamma-Ray Instrumentation for Astronomy XIII*. Edited by Flanagan, Kathryn A.; Siegmund, Oswald H. W. *Proceedings of the SPIE*, Volume 5165, pp. 497-508 (2004), ed. K. A. Flanagan & O. H. W. Siegmund, 497-508
- Martini, P., Kelson, D. D., Mulchaey, J. S., & Athey, A. 2004, in *Clusters of Galaxies: Probes of Cosmological Structure and Galaxy Evolution*, ed. J. S. Mulchaey, A. Dressler, & A. Oemler
- Mathiesen, B. F., & Evrard, A. E. 2001, *ApJ*, 546, 100 (ME01)
- Maughan, B. J. 2007, *ArXiv Astrophysics e-prints*
- Maughan, B. J., Jones, C., Forman, W., & Van Speybroeck, L. 2007, *ArXiv Astrophysics e-prints*
- Mazzotta, P., Markevitch, M., Forman, W. R., Jones, C., Vikhlinin, A., & VanSpeybroeck, L. 2001a, *ArXiv Astrophysics e-prints*
- Mazzotta, P., Markevitch, M., Vikhlinin, A., Forman, W. R., David, L. P., & VanSpeybroeck, L. 2001b, *ApJ*, 555, 205
- Mazzotta, P., Rasia, E., Moscardini, L., & Tormen, G. 2004, *MNRAS*, 354, 10
- McCarthy, I. G. and Balogh, M. L. and Babul, A. and Poole, G. B. & Horner, D. J., 2004, *ApJ*, 613, 811
- Mercurio, A., Massarotti, M., Merluzzi, P., Girardi, M., La Barbera, F., & Busarello, G. 2003, *A&A*, 408, 57
- Metzger, M. R., & Ma, C.-P. 2000, *AJ*, 120, 2879
- Mewe, R., Gronenschild, E. H. B. M., & van den Oord, G. H. J. 1985, *A&AS*, 62, 197
- Mewe, R., Lemen, J. R., & van den Oord, G. H. J. 1986, *A&AS*, 65, 511
- Mohr, J. J., & Evrard, A. E. 1997, *ApJ*, 491, 38
- Molendi, S., De Grandi, S., & Fusco-Femiano, R. 2000, *ApJ*, 534, L43
- Morrison, R., & McCammon, D. 1983, *ApJ*, 270, 119
- Nagai, D., Kravtsov, A. V., & Vikhlinin, A., 2007, *ApJ*, 668, 1
- Nousek, J. A., & Shue, D. R. 1989, *ApJ*, 342, 1207
- Poole, G. B., Fardal, M. A., Babul, A., McCarthy, I. G., Quinn, T., & Wadsley, J. 2006, *MNRAS*, 373, 881
- O'Hara, T. B., Mohr, J. J., Bialek, J. J., & Evrard, A. E. 2006, *ApJ*, 639, 64
- Ohta, Y., Kumai, Y., Watanabe, M., Furuzawa, A., Akimoto, F., Tawara, Y., Sato, S., Yamashita, K., Arai, K., Shiratori, Y., Miyoshi, S., & Mazure, A. 2001, in *Astronomical Society of the Pacific Conference Series*, Vol. 251, *New Century of X-ray Astronomy*, ed. H. Inoue & H. Kunieda, 474+
- Ota, N., Kitayama, T., Masai, K., & Mitsuda, K. 2006, *ApJ*, 640, 673
- Peres, C. B., Fabian, A. C., Edge, A. C., Allen, S. W., Johnstone, R. M., & White, D. A. 1998, *MNRAS*, 298, 416
- Riess, A. G., Filippenko, A. V., Challis, P., Clocchiatti, A., Diercks, A., Garnavich, P. M., Gilliland, R. L., Hogan, C. J., Jha, S., Kirshner, R. P., Leibundgut, B., Phillips, M. M., Reiss, D., Schmidt, B. P., Schommer, R. A., Smith, R. C., Spyromilio, J., Stubbs, C., Suntzeff, N. B., & Tonry, J. 1998, *AJ*, 116, 1009
- Riess, A. G., Strolger, L.-G., Casertano, S., Ferguson, H. C., Mobasher, B., Gold, B., Challis, P. J., Filippenko, A. V., Jha, S., Li, W., Tonry, J., Foley, R., Kirshner, R. P., Dickinson, M., MacDonald, E., Eisenstein, D., Livio, M., Younger, J., Xu, C., Dahlen, T., & Stern, D. 2007, *ApJ*, 659, 98
- Rosati, P., della Ceca, R., Burg, R., Norman, C., & Giacconi, R. 1995, *ApJ*, 445, L11
- Sakellou, I., & Ponman, T. J. 2004, *MNRAS*, 351, 1439
- Sakellou, I., & Merrifield, M. R. 2000, *MNRAS*, 311, 649
- Sanderson, A. J. R., Ponman, T. J., & O'Sullivan, E. 2006, *MNRAS*, 1068
- Smith, G. P., Kneib, J.-P., Smail, I., Mazzotta, P., Ebeling, H., & Czoske, O. 2005, *MNRAS*, 359, 417
- Snowden, S. L., Mushotzky, R. M., Kuntz, K. D., & Davis, D. S. 2007, *ArXiv e-prints*, 710
- Teague, P. F., Carter, D., & Gray, P. M. 1990, *ApJS*, 72, 715
- Townsend, L. K., Broos, P. S., Garmire, G. P., & Nousek, J. A. 2000, *ApJ*, 534, L139
- Tucker, W., Blanco, P., Rappoport, S., David, L., Fabricant, D., Falco, E. E., Forman, W., Dressler, A., & Ramella, M. 1998, *ApJ*, 496, L5+
- Ventimiglia, D., Voit, G. M., Borgani, S., & Donahue, M. 2008, *ApJ Submitted*
- Vikhlinin, A. 2006, *ApJ*, 640, 710
- Vikhlinin, A., Markevitch, M., Murray, S. S., Jones, C., Forman, W., & Van Speybroeck, L. 2005, *ApJ*, 628, 655
- Vikhlinin, A., McNamara, B. R., Forman, W., Jones, C., Quintana, H., & Hornstrup, A. 1998, *ApJ*, 502, 558
- Voit, G. M. 2005, *Reviews of Modern Physics*, 77, 207
- Wang, L., & Steinhardt, P. J. 1998, *ApJ*, 508, 483
- Wang, S., Khoury, J., Haiman, Z., & May, M. 2004, *Phys. Rev. D*, 70, 123008
- White, D. A., Jones, C., & Forman, W. 1997, *MNRAS*, 292, 419
- Yang, Y., Huo, Z., Zhou, X., Xue, S., Mao, S., Ma, J., & Chen, J. 2004, *ApJ*, 614, 692
- Yuan, Q.-R., Yan, P.-F., Yang, Y.-B., & Zhou, X. 2005, *Chinese Journal of Astronomy and Astrophysics*, 5, 126

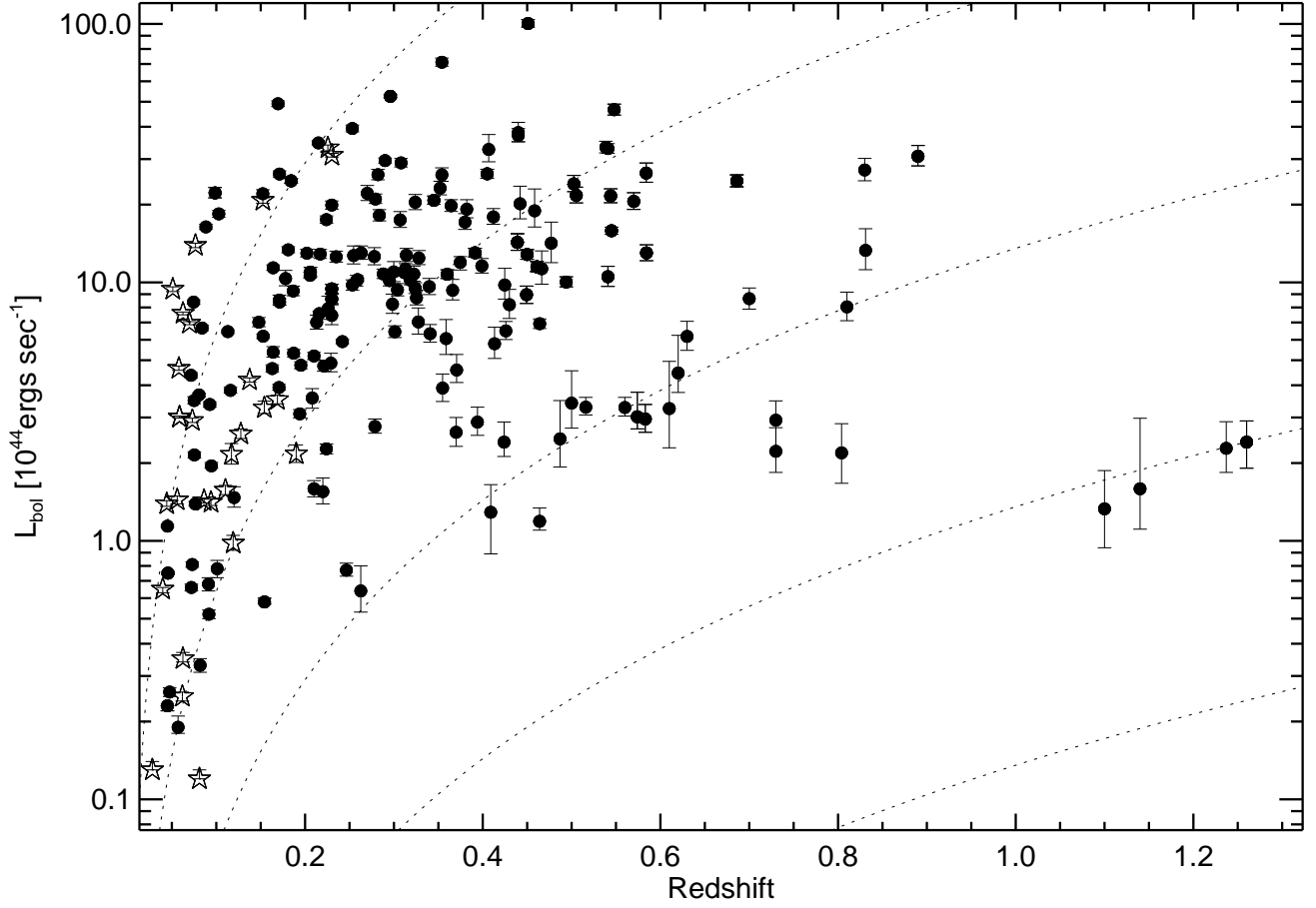


FIG. 1.— Bolometric luminosity ($E = 0.1 - 100$ keV) plotted as a function of redshift for the 202 clusters which make up the initial sample. L_{bol} values are limited to the region of spectral extraction, $R = R_{2500-CORE}$. For clusters without $R_{2500-CORE}$ fits, $R = R_{5000-CORE}$ fits were used and are denoted in the figure by empty stars. Dotted lines represent constant fluxes of 3.0×10^{-15} , 10^{-14} , 10^{-13} , and 10^{-12} ergs sec $^{-1}$ cm $^{-2}$.

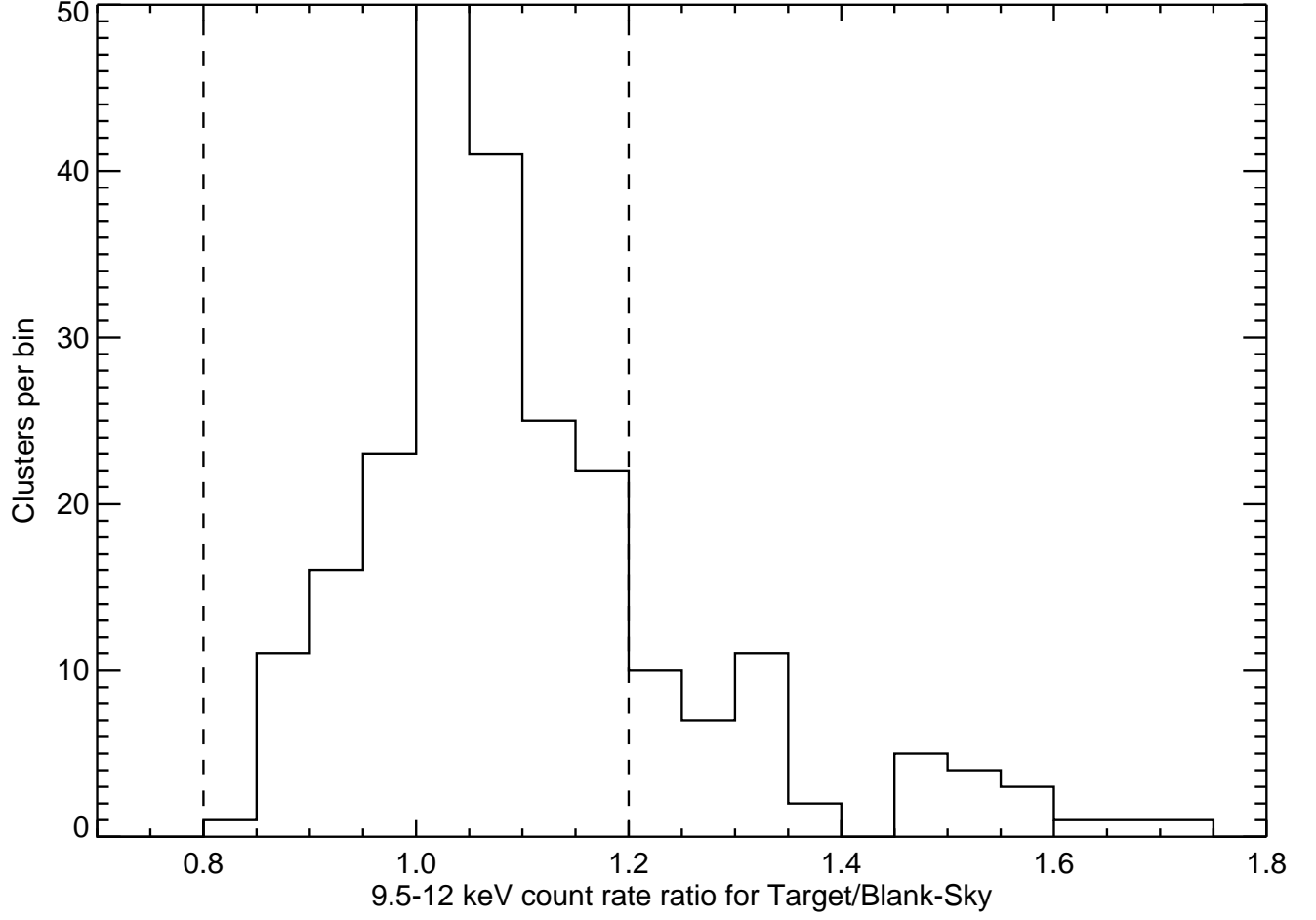


FIG. 2.— Ratio of target field and blank-sky field count rates in the 9.5-12.0 keV band for all 244 observations in our initial sample. Vertical dashed lines represent $\pm 20\%$ of unity. Despite the good agreement between the blank-sky background and observation count rates for most observations, all backgrounds are normalized.

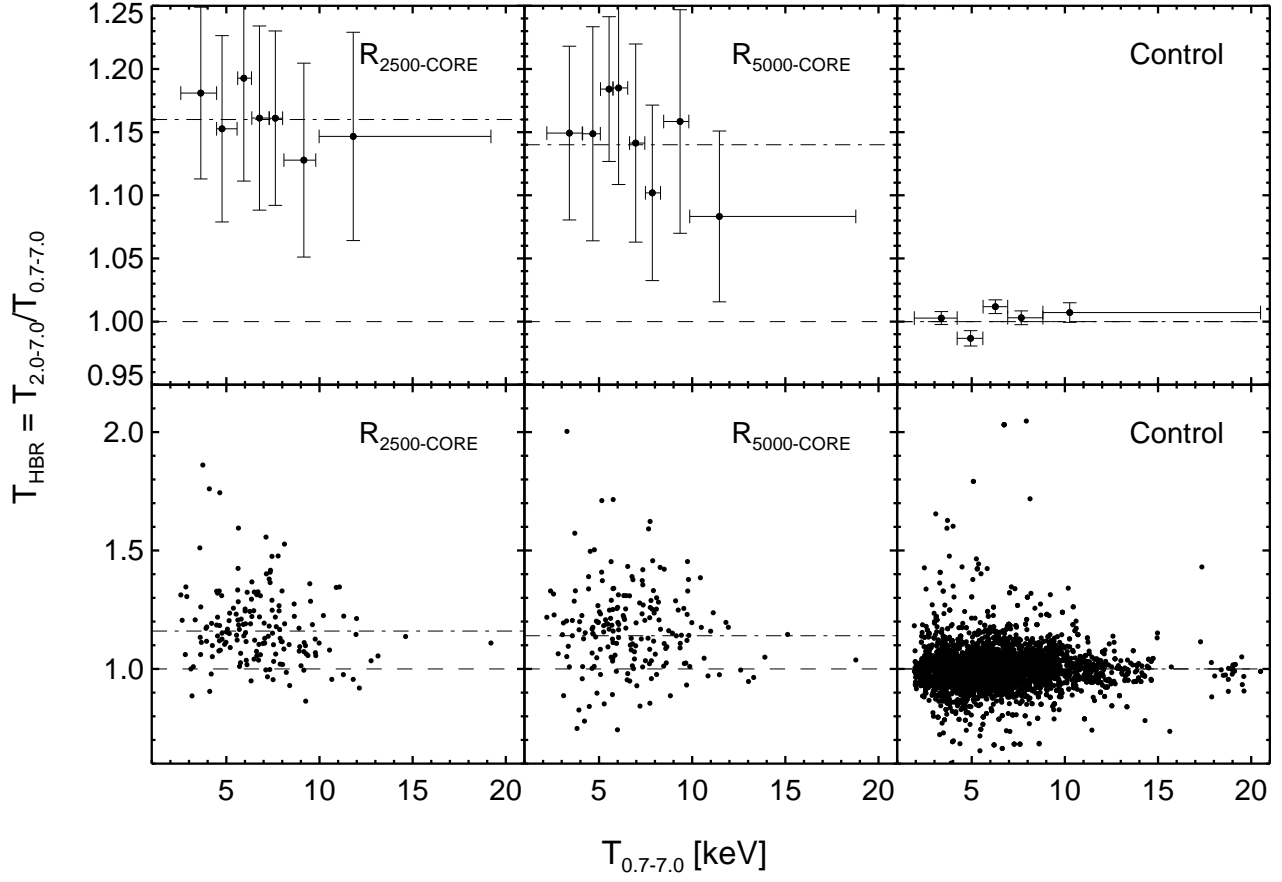


FIG. 3.— Best-fit temperatures for the hard-band, $T_{2.0-7.0}$, divided by the broad-band, $T_{0.7-7.0}$, and plotted against the broad-band temperature. For binned data, each bin contains 25 clusters, with the exception of the highest temperature bins which contain 16 and 17 for $R_{2500\text{-CORE}}$ and $R_{5000\text{-CORE}}$, respectively. The simulated data bins contain 1000 clusters with the last bin having 780 clusters. The line of equality is shown as a dashed line and the weighted mean for the full sample is shown as a dashed-dotted line. Error bars are omitted in the unbinned data for clarity. Note the net skewing of T_{HBR} to greater than unity for both apertures with no such trend existing in the simulated data. The dispersion of T_{HBR} for the real data is also much larger than the dispersion of the simulated data.

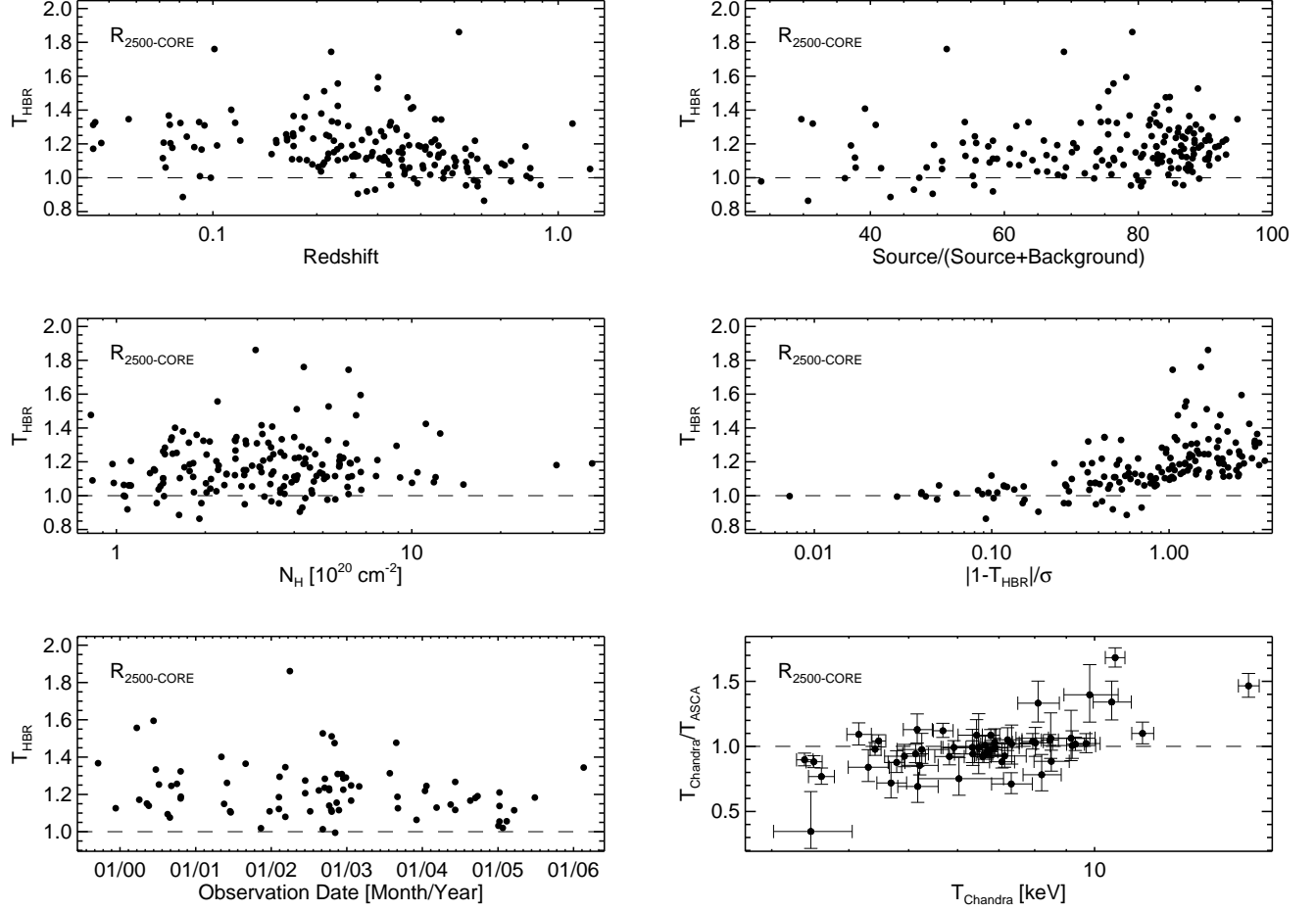


FIG. 4.— Plotted here are a few possible sources of systematic uncertainty versus T_{HBR} calculated for the $R_{2500-CORE}$ apertures (166 clusters). Error bars have been omitted in several plots for clarity. The line of equality is shown as a dashed line in all panels. (**Upper-left:**) T_{HBR} versus redshift for the entire sample. The trend in T_{HBR} with redshift is expected as the $T_{2.0-7.0}$ lower boundary nears convergence with the $T_{0.7-7.0}$ lower boundary at $z \approx 1.85$. Weighted values of T_{HBR} are consistent with unity starting at $z \sim 0.6$. (**Upper-right:**) T_{HBR} versus percentage of spectrum flux which is attributed to the source. We find no trend with signal-to-noise which suggests calibration uncertainty not is playing a major role in our results. (**Middle-left:**) T_{HBR} versus Galactic column density. We find no trend in absorption which would result if N_{HI} values are inaccurate or if we had improperly accounted for local soft contamination. (**Middle-right:**) T_{HBR} versus the deviation from unity in units of measurement uncertainty. Recall that we have used 90% confidence (1.6σ) for our analysis. (**Lower-left:**) T_{HBR} plotted versus observation start date. The plotted points are culled from the full sample and represent only clusters which have a single observation and where the spectral flux is $> 75\%$ from the source. We note no systematic trend with time. (**Lower-right:**) Ratio of *Chandra* temperatures derived in this work to *ASCA* temperatures taken from Don Horner's thesis. We note a trend of comparatively hotter *Chandra* temperatures for clusters > 10 keV, otherwise our derived temperatures are in good agreement with those of *ASCA*.

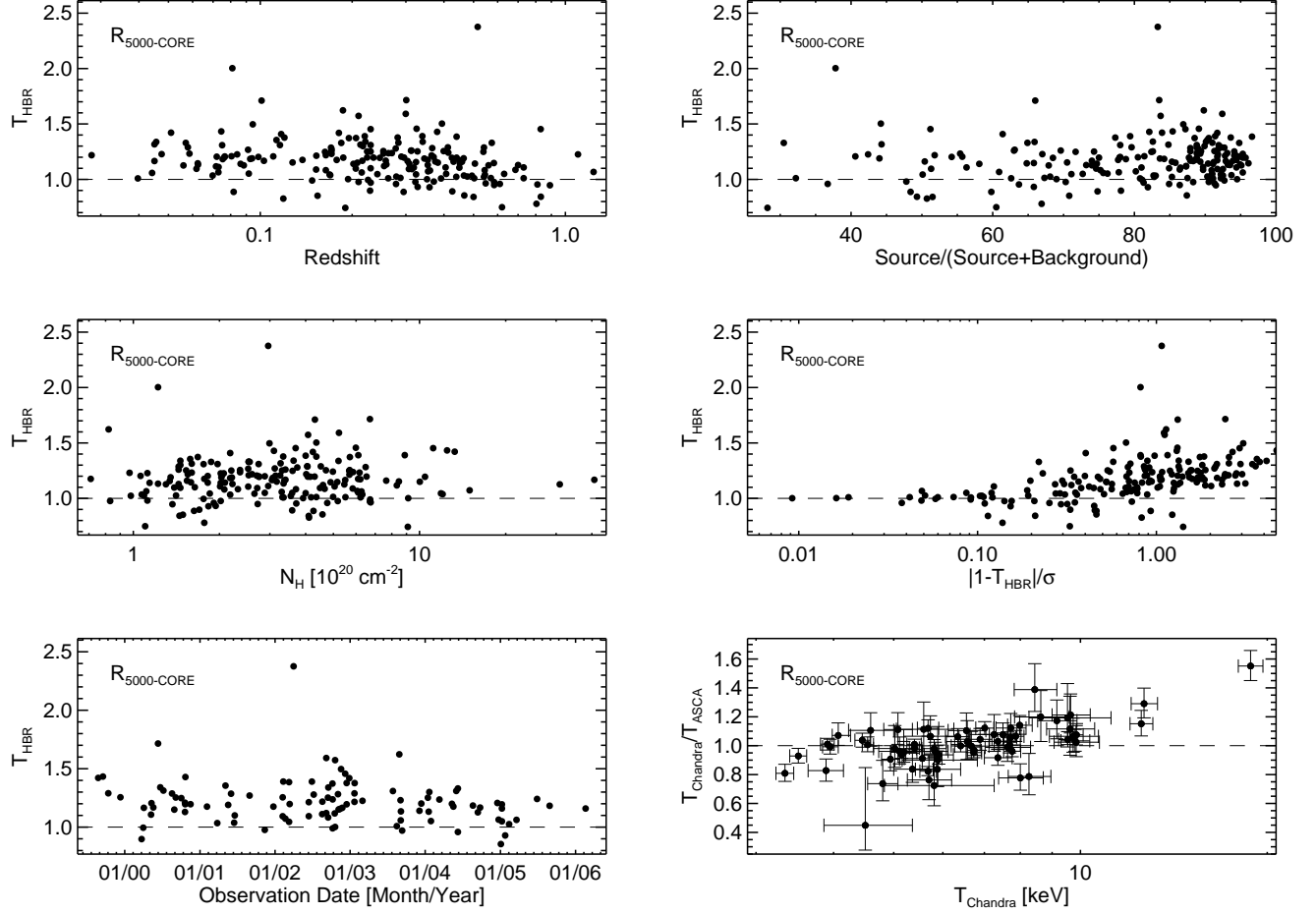


FIG. 5.— Plotted here are a few possible sources of systematic uncertainty versus T_{HBR} calculated for the R_{5000} -CORE apertures (192 clusters). Error bars have been omitted in several plots for clarity. The line of equality is shown as a dashed line in all panels. (**Upper-left:**) T_{HBR} versus redshift for the entire sample. The trend in T_{HBR} with redshift is expected as the $T_{2.0-7.0}$ lower boundary nears convergence with the $T_{0.7-7.0}$ lower boundary at $z \approx 1.85$. Weighted values of T_{HBR} are consistent with unity starting at $z \sim 0.6$. (**Upper-right:**) T_{HBR} versus percentage of spectrum flux which is attributed to the source. We find no trend with signal-to-noise which suggests calibration uncertainty is not playing a major role in our results. (**Middle-left:**) T_{HBR} versus Galactic column density. We find no trend in absorption which would result if N_{HI} values are inaccurate or if we had improperly accounted for local soft contamination. (**Middle-right:**) T_{HBR} versus the deviation from unity in units of measurement uncertainty. Recall that we have used 90% confidence (1.6σ) for our analysis. (**Lower-left:**) T_{HBR} plotted versus observation start date. The plotted points are culled from the full sample and represent only clusters which have a single observation and where the spectral flux is $> 75\%$ from the source. We note no systematic trend with time. (**Lower-right:**) Ratio of *Chandra* temperatures derived in this work to *ASCA* temperatures taken from Don Horner's thesis. We note a trend of comparatively hotter *Chandra* temperatures for clusters > 10 keV, otherwise our derived temperatures are in good agreement with those of *ASCA*.

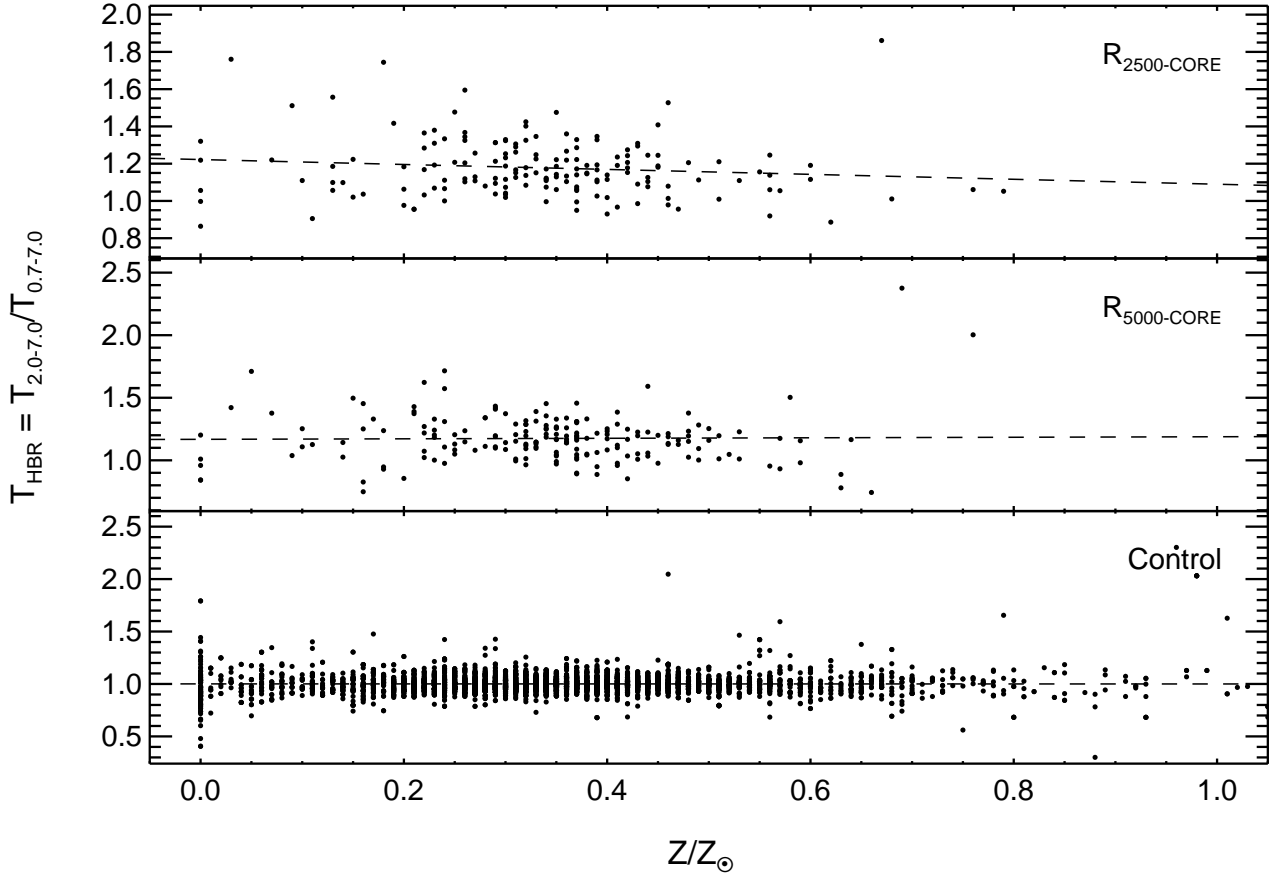


FIG. 6.— Plotted here is T_{HBR} as a function of metal abundance for $R_{2500-CORE}$, $R_{5000-CORE}$, and the Control sample (see discussion of control sample in §5.2). Error bars are omitted for clarity. The dashed-line represents the linear best-fit using the bivariate correlated error and intrinsic scatter (BCES) method of Akritas & Bershady (1996) which takes into consideration errors on both T_{HBR} and abundance when performing the fit. We note no trend in T_{HBR} with metallicity (the apparent trend in the top panel is not significant) and also note the low dispersion in the control sample relative to the observations. The striation of abundance arises from our use of two decimal places in recording the best-fit values from XSPEC.

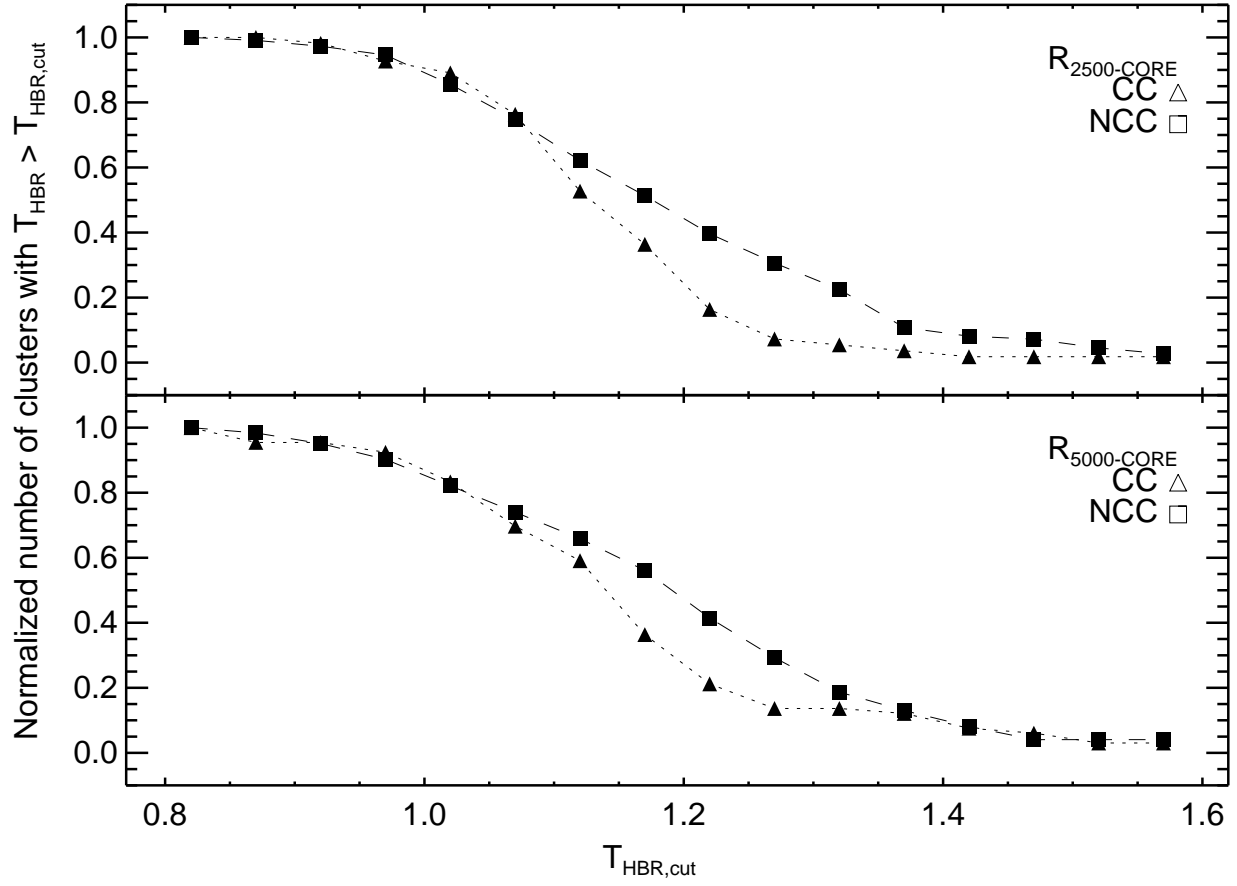


FIG. 7.— Plotted here is the normalized number of cool core (CC) and non-cool core (NCC) clusters as a function of cuts in T_{HBR} . There are 166 clusters plotted in the top panel and 192 in the bottom panel. We have defined a cluster as having a cool core (CC) when the temperature for the 50 kpc region around the cluster center divided by the temperature for $R_{2500-CORE}$, or $R_{5000-CORE}$, was less than one at the 2σ level. We then take cuts in T_{HBR} at the 1σ level and ask how many CC and NCC clusters are above these cuts. The number of CC clusters falls off more rapidly than NCC clusters in this classification scheme suggesting higher values of T_{HBR} prefer less relaxed systems which do not have cool cores. This result is insensitive to our choice of significance level in both the core classification and T_{HBR} cuts.

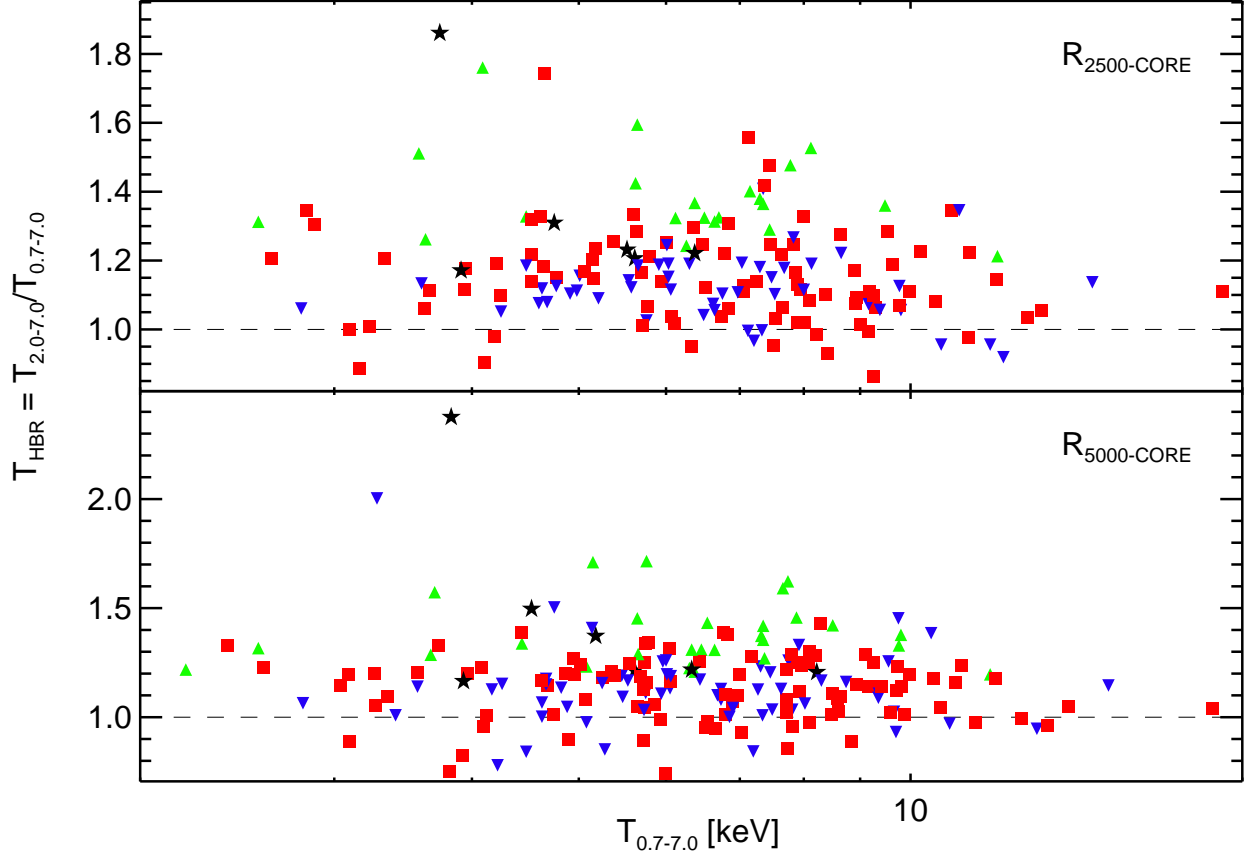


FIG. 8.— T_{HBR} plotted against $T_{0.7-7.0}$ for the $R_{2500-CORE}$ and $R_{5000-CORE}$ apertures. Note the vertical scales for both panels are not the same. The top and bottom panes contain 166 and 192 clusters respectively. Only two clusters – Abell 697 and MACS J2049.9-3217 – do not have a $T_{HBR} > 1.1$ in one aperture and not the other. In both cases though, it was a result of narrowly missing the cut. The dashed lines are the lines of equivalence. Symbols and color coding are based on two criteria: 1) presence of a cool core (CC) and 2) value of T_{HBR} . Black stars (6 top, 7 bottom) are clusters with a CC and T_{HBR} significantly greater than 1.1. Green upright-triangles (21 top, 27 bottom) are NCC clusters with T_{HBR} significantly greater than 1.1. Blue down-facing triangles (49 top, 60 bottom) are CC clusters and red squares (90 top, 98 bottom) are NCC clusters. We have found most, if not all, of the clusters with $T_{HBR} \gtrsim 1.1$ are merger systems. Note that the cut at $T_{HBR} > 1.1$ is arbitrary and there are more merger systems in our sample than just those highlighted in this figure. However it is rather suggestive that clusters with the highest values of T_{HBR} appear to be merging systems.

TABLE 1
SUMMARY OF SAMPLE

Cluster	Obs.ID	R.A. hr:min:sec	Dec. ° : ' : ''	ExpT ksec	Mode	ACIS	z	L_{bol} 10^{44} ergs s $^{-1}$
(1)	(2)	(3)	(4)	(5)	(6)	(7)	(8)	(9)
1E0657 56	3184	06:58:29.622	-55:56:39.79	87.5	VF	I3	0.296	52.48
1E0657 56	5356	06:58:29.619	-55:56:39.78	97.2	VF	I2	0.296	52.48
1E0657 56	5361	06:58:29.620	-55:56:39.80	82.6	VF	I3	0.296	52.48
1RXS J2129.4-0741	3199	21:29:26.274	-07:41:29.38	19.9	VF	I3	0.570	20.58
1RXS J2129.4-0741	3595	21:29:26.281	-07:41:29.36	19.9	VF	I3	0.570	20.58
2PIGG J0011.5-2850	5797	00:11:21.623	-28:51:14.44	19.9	VF	I3	0.075	2.15
2PIGG J0311.8-2655 ‡	5799	03:11:33.904	-26:54:16.48	39.6	VF	I3	0.062	0.25
2PIGG J2227.0-3041	5798	22:27:54.560	-30:34:34.84	22.3	VF	I2	0.073	0.81
3C 220.1	839	09:32:40.218	+79:06:29.46	18.9	F	S3	0.610	3.25
3C 28.0	3233	00:55:50.401	+26:24:36.47	49.7	VF	I3	0.195	4.78
3C 295	2254	14:11:20.280	+52:12:10.55	90.9	VF	I3	0.464	6.92
3C 388	5295	18:44:02.365	+45:33:29.31	30.7	VF	I3	0.092	0.52
4C 55.16	4940	08:34:54.923	+55:34:21.15	96.0	VF	S3	0.242	5.90
ABELL 0013 ‡	4945	00:13:37.883	-19:30:09.10	55.3	VF	S3	0.094	1.41
ABELL 0068	3250	00:37:06.309	+09:09:32.28	10.0	VF	I3	0.255	12.70
ABELL 0119 ‡	4180	00:56:15.150	-01:14:59.70	11.9	VF	I3	0.044	1.39
ABELL 0168	3203	01:14:57.909	+00:24:42.55	40.6	VF	I3	0.045	0.23
ABELL 0168	3204	01:14:57.925	+00:24:42.73	37.6	VF	I3	0.045	0.23
ABELL 0209	3579	01:31:52.585	-13:36:39.29	10.0	VF	I3	0.206	10.96
ABELL 0209	522	01:31:52.595	-13:36:39.25	10.0	VF	I3	0.206	10.96
ABELL 0267	1448	01:52:29.181	+00:57:34.43	7.9	F	I3	0.230	8.62
ABELL 0267	3580	01:52:29.180	+00:57:34.23	19.9	VF	I3	0.230	8.62
ABELL 0370	515	02:39:53.169	-01:34:36.96	88.0	F	S3	0.375	11.95
ABELL 0383	2321	02:48:03.364	-03:31:44.69	19.5	F	S3	0.187	5.32
ABELL 0399	3230	02:57:54.931	+13:01:58.41	48.6	VF	I0	0.072	4.37
ABELL 0401	518	02:58:56.896	+13:34:14.48	18.0	F	I3	0.074	8.39
ABELL 0478	6102	04:13:25.347	+10:27:55.62	10.0	VF	I3	0.088	16.39
ABELL 0514	3578	04:48:19.229	-20:30:28.79	44.5	VF	I3	0.072	0.66
ABELL 0520	4215	04:54:09.711	+02:55:23.69	66.3	VF	I3	0.202	12.97
ABELL 0521	430	04:54:07.004	-10:13:26.72	39.1	VF	S3	0.253	9.77
ABELL 0586	530	07:32:20.339	+31:37:58.59	10.0	VF	I3	0.171	8.54
ABELL 0611	3194	08:00:56.832	+36:03:24.09	36.1	VF	S3	0.288	10.78
ABELL 0644 ‡	2211	08:17:25.225	-07:30:40.03	29.7	VF	I3	0.070	6.95
ABELL 0665	3586	08:30:59.231	+65:50:37.78	29.7	VF	I3	0.181	13.37
ABELL 0697	4217	08:42:57.549	+36:21:57.65	19.5	VF	I3	0.282	26.10
ABELL 0773	5006	09:17:52.566	+51:43:38.18	19.8	VF	I3	0.217	12.87
ABELL 0781	534	09:20:25.431	+30:30:07.56	9.9	VF	I3	0.298	8.24
ABELL 0907	3185	09:58:21.880	-11:03:52.20	48.0	VF	I3	0.153	6.19
ABELL 0963	903	10:17:03.744	+39:02:49.17	36.3	F	S3	0.206	10.65
ABELL 1063S	4966	22:48:44.294	-44:31:48.37	26.7	VF	I3	0.354	71.09
ABELL 1068 ‡	1652	10:40:44.520	+39:57:10.28	26.8	F	S3	0.138	4.19
ABELL 1201 ‡	4216	11:12:54.489	+13:26:08.76	39.7	VF	S3	0.169	3.52
ABELL 1204	2205	11:13:20.419	+17:35:38.45	23.6	VF	I3	0.171	3.92
ABELL 1361 ‡	2200	11:43:39.827	+46:21:21.40	16.7	F	S3	0.117	2.16
ABELL 1423	538	11:57:17.026	+33:36:37.44	9.8	VF	I3	0.213	7.01
ABELL 1651	4185	12:59:22.830	-04:11:45.86	9.6	VF	I3	0.084	6.66
ABELL 1664 ‡	1648	13:03:42.478	-24:14:44.55	9.8	VF	S3	0.128	2.59
ABELL 1682	3244	13:06:50.764	+46:33:19.86	9.8	VF	I3	0.226	7.92
ABELL 1689	1663	13:11:29.612	-01:20:28.69	10.7	F	I3	0.184	24.71
ABELL 1689	5004	13:11:29.606	-01:20:28.61	19.9	VF	I3	0.184	24.71
ABELL 1689	540	13:11:29.595	-01:20:28.47	10.3	F	I3	0.184	24.71
ABELL 1758	2213	13:32:42.978	+50:32:44.83	58.3	VF	S3	0.279	21.01
ABELL 1763	3591	13:35:17.957	+40:59:55.80	19.6	VF	I3	0.187	9.26
ABELL 1795 ‡	5289	13:48:52.829	+26:35:24.01	15.0	VF	I3	0.062	7.59
ABELL 1835	495	14:01:01.951	+02:52:43.18	19.5	F	S3	0.253	39.38
ABELL 1914	3593	14:26:01.399	+37:49:27.83	18.9	VF	I3	0.171	26.25
ABELL 1942	3290	14:38:21.878	+03:40:12.97	57.6	VF	I2	0.224	2.27
ABELL 1995	906	14:52:57.758	+58:02:51.34	0.0	F	S3	0.319	10.19
ABELL 2029 ‡	6101	15:10:56.163	+05:44:40.89	9.9	VF	I3	0.076	13.90
ABELL 2034	2204	15:10:11.003	+33:30:46.46	53.9	VF	I3	0.113	6.45
ABELL 2065 ‡	31821	15:22:29.220	+27:42:46.54	0.0	VF	I3	0.073	2.92
ABELL 2069	4965	15:24:09.181	+29:53:18.05	55.4	VF	I2	0.116	3.82
ABELL 2111	544	15:39:41.432	+34:25:12.26	10.3	F	I3	0.230	7.45
ABELL 2125	2207	15:41:14.154	+66:15:57.20	81.5	VF	I3	0.246	0.77
ABELL 2163	1653	16:15:45.705	-06:09:00.62	71.1	VF	I1	0.170	49.11
ABELL 2204 ‡	499	16:32:45.437	+05:34:21.05	10.1	F	S3	0.152	20.77
ABELL 2204	6104	16:32:45.428	+05:34:20.89	9.6	VF	I3	0.152	22.03
ABELL 2218	1666	16:35:50.831	+66:12:42.31	48.6	VF	I0	0.171	8.39
ABELL 2219 ‡	896	16:40:21.069	+46:42:29.07	42.3	F	S3	0.226	33.15
ABELL 2255	894	17:12:40.385	+64:03:50.63	39.4	F	I3	0.081	3.67
ABELL 2256 ‡	1386	17:03:44.567	+78:38:11.51	12.4	F	I3	0.058	4.65
ABELL 2259	3245	17:20:08.299	+27:40:11.53	10.0	VF	I3	0.164	5.37
ABELL 2261	5007	17:22:27.254	+32:07:58.60	24.3	VF	I3	0.224	17.49
ABELL 2294	3246	17:24:10.149	+85:53:09.77	10.0	VF	I3	0.178	10.35

TABLE 1 — *Continued*

Cluster	Obs.ID	R.A. hr:min:sec	Dec. ° : ' : "	ExpT ksec	Mode	ACIS	z	L_{bol} . 10^{44} ergs s $^{-1}$
(1)	(2)	(3)	(4)	(5)	(6)	(7)	(8)	(9)
ABELL 2384	4202	21:52:21.178	-19:32:51.90	31.5	VF	I3	0.095	1.95
ABELL 2390 ‡	4193	21:53:36.825	+17:41:44.38	95.1	VF	S3	0.230	31.02
ABELL 2409	3247	22:00:52.567	+20:58:34.11	10.2	VF	I3	0.148	7.01
ABELL 2537	4962	23:08:22.313	-02:11:29.88	36.2	VF	S3	0.295	10.16
ABELL 2550	2225	23:11:35.806	-21:44:46.70	59.0	VF	S3	0.154	0.58
ABELL 2554 ‡	1696	23:12:19.939	-21:30:09.84	19.9	VF	S3	0.110	1.57
ABELL 2556 ‡	2226	23:13:01.413	-21:38:04.47	19.9	VF	S3	0.086	1.43
ABELL 2631	3248	23:37:38.560	+00:16:28.64	9.2	VF	I3	0.278	12.59
ABELL 2667	2214	23:51:39.395	-26:05:02.75	9.6	VF	S3	0.230	19.91
ABELL 2670	4959	23:54:13.687	-10:25:08.85	39.6	VF	I3	0.076	1.39
ABELL 2717	6974	00:03:11.996	-35:56:08.01	19.8	VF	I3	0.048	0.26
ABELL 2744	2212	00:14:14.396	-30:22:40.04	24.8	VF	S3	0.308	29.00
ABELL 3128 ‡	893	03:29:50.918	-52:34:51.04	19.6	F	I3	0.062	0.35
ABELL 3158 ‡	3201	03:42:54.675	-53:37:24.36	24.8	VF	I3	0.059	3.01
ABELL 3158 ‡	3712	03:42:54.683	-53:37:24.37	30.9	VF	I3	0.059	3.01
ABELL 3164	6955	03:46:16.839	-57:02:11.38	13.5	VF	I3	0.057	0.19
ABELL 3376	3202	06:02:05.122	-39:57:42.82	44.3	VF	I3	0.046	0.75
ABELL 3376	3450	06:02:05.162	-39:57:42.87	19.8	VF	I3	0.046	0.75
ABELL 3391 ‡	4943	06:26:21.511	-53:41:44.81	18.4	VF	I3	0.056	1.44
ABELL 3921	4973	22:49:57.829	-64:25:42.17	29.4	VF	I3	0.093	3.37
AC 114	1562	22:58:48.196	-34:47:56.89	72.5	F	S3	0.312	10.90
CL 0024+17	929	00:26:35.996	+17:09:45.37	39.8	F	S3	0.394	2.88
CL 1221+4918	1662	12:21:26.709	+49:18:21.60	79.1	VF	I3	0.700	8.65
CL J0030+2618	5762	00:30:34.339	+26:18:01.58	17.9	VF	I3	0.500	3.41
CL J0152-1357	913	01:52:42.141	-13:57:59.71	36.5	F	I3	0.831	13.30
CL J0542.8-4100	914	05:42:49.994	-40:59:58.50	50.4	F	I3	0.630	6.18
CL J0848+4456	1708	08:48:48.255	+44:56:17.11	61.4	VF	I1	0.574	3.02
CL J0848+4456	927	08:48:48.252	+44:56:17.13	125.1	VF	I1	0.574	3.02
CL J1113.1-2615	915	11:13:05.167	-26:15:40.43	104.6	F	I3	0.730	2.22
CL J1213+0253	4934	12:13:34.948	+02:53:45.45	18.9	VF	I3	0.409	1.29
CL J1226.9+3332	3180	12:26:58.373	+33:32:47.36	31.7	VF	I3	0.890	30.76
CL J1226.9+3332	5014	12:26:58.372	+33:32:47.38	32.7	VF	I3	0.890	30.76
CL J1641+4001	3575	16:41:53.704	+40:01:44.40	46.5	VF	I3	0.464	1.19
CL J2302.8+0844	918	23:02:48.156	+08:43:52.74	108.6	F	I3	0.730	2.93
DLS J0514-4904	4980	05:14:40.037	-49:03:15.07	19.9	VF	I3	0.091	0.68
EXO 0422-086 ‡	4183	04:25:51.271	-08:33:36.42	10.0	VF	I3	0.040	0.65
HERCULES A ‡	1625	16:51:08.161	+04:59:32.44	14.8	VF	S3	0.154	3.27
IRAS 09104+4109	509	09:13:45.481	+40:56:27.49	9.1	F	S3	0.442	20.15
LYNX E	17081	08:48:58.851	+44:51:51.44	61.4	VF	I2	1.260	2.10
LYNX E	9271	08:48:58.858	+44:51:51.46	125.1	VF	I2	1.260	2.10
MACS J0011.7-1523	3261	00:11:42.965	-15:23:20.79	21.6	VF	I3	0.360	10.75
MACS J0011.7-1523	6105	00:11:42.957	-15:23:20.76	37.3	VF	I3	0.360	10.75
MACS J0025.4-1222	3251	00:25:29.398	-12:22:38.15	19.3	VF	I3	0.584	13.00
MACS J0025.4-1222	5010	00:25:29.399	-12:22:38.10	24.8	VF	I3	0.584	13.00
MACS J0035.4-2015	3262	00:35:26.573	-20:15:46.06	21.4	VF	I3	0.364	19.79
MACS J0111.5+0855	3256	01:11:31.515	+08:55:39.21	19.4	VF	I3	0.263	0.64
MACS J0152.5-2852	3264	01:52:34.479	-28:53:38.01	17.5	VF	I3	0.341	6.33
MACS J0159.0-3412	5818	01:59:00.366	-34:13:00.23	9.4	VF	I3	0.458	18.92
MACS J0159.8-0849	3265	01:59:49.453	-08:50:00.90	17.9	VF	I3	0.405	26.31
MACS J0159.8-0849	6106	01:59:49.452	-08:50:00.92	35.3	VF	I3	0.405	26.31
MACS J0242.5-2132	3266	02:42:35.906	-21:32:26.30	11.9	VF	I3	0.314	12.74
MACS J0257.1-2325	1654	02:57:09.150	-23:26:06.25	19.8	F	I3	0.505	21.72
MACS J0257.1-2325	3581	02:57:09.152	-23:26:06.21	18.5	VF	I3	0.505	21.72
MACS J0257.6-2209	3267	02:57:41.024	-22:09:11.12	20.5	VF	I3	0.322	10.77
MACS J0308.9+2645	3268	03:08:55.927	+26:45:38.34	24.4	VF	I3	0.324	20.42
MACS J0329.6-0211	3257	03:29:41.681	-02:11:47.67	9.9	VF	I3	0.450	12.82
MACS J0329.6-0211	3582	03:29:41.688	-02:11:47.81	19.9	VF	I3	0.450	12.82
MACS J0329.6-0211	6108	03:29:41.681	-02:11:47.57	39.6	VF	I3	0.450	12.82
MACS J0404.6+1109	3269	04:04:32.491	+11:08:02.10	21.8	VF	I3	0.355	3.90
MACS J0417.5-1154	3270	04:17:34.686	-11:54:32.71	12.0	VF	I3	0.440	37.99
MACS J0429.6-0253	3271	04:29:36.088	-02:53:09.02	23.2	VF	I3	0.399	11.58
MACS J0451.9+0006	5815	04:51:54.291	+00:06:20.20	10.2	VF	I3	0.430	8.20
MACS J0455.2+0657	5812	04:55:17.426	+06:57:47.15	9.9	VF	I3	0.425	9.77
MACS J0520.7-1328	3272	05:20:42.052	-13:28:49.38	19.2	VF	I3	0.340	9.63
MACS J0547.0-3904	3273	05:47:01.582	-39:04:28.24	21.7	VF	I3	0.210	1.59
MACS J0553.4-3342	5813	05:53:27.200	-33:42:53.02	9.9	VF	I3	0.407	32.68
MACS J0717.5+3745	1655	07:17:31.654	+37:45:18.52	19.9	F	I3	0.548	46.58
MACS J0717.5+3745	4200	07:17:31.651	+37:45:18.46	59.2	VF	I3	0.548	46.58
MACS J0744.8+3927	3197	07:44:52.802	+39:27:24.43	20.2	VF	I3	0.686	24.67
MACS J0744.8+3927	3585	07:44:52.809	+39:27:24.41	19.9	VF	I3	0.686	24.67
MACS J0744.8+3927	6111	07:44:52.800	+39:27:24.42	49.5	VF	I3	0.686	24.67
MACS J0911.2+1746	3587	09:11:11.325	+17:46:31.02	17.9	VF	I3	0.541	10.52
MACS J0911.2+1746	5012	09:11:11.329	+17:46:30.99	23.8	VF	I3	0.541	10.52
MACS J0949+1708	3274	09:49:51.824	+17:07:05.62	14.3	VF	I3	0.382	19.19
MACS J1006.9+3200	5819	10:06:54.668	+32:01:34.61	10.9	VF	I3	0.359	6.06

TABLE 1 — *Continued*

Cluster	Obs.ID	R.A. hr:min:sec	Dec. ° : ' : "	ExpT ksec	Mode	ACIS	z	L_{bol} . 10^{44} ergs s $^{-1}$
(1)	(2)	(3)	(4)	(5)	(6)	(7)	(8)	(9)
MACS J1105.7-1014	5817	11:05:46.462	-10:14:37.20	10.3	VF	I3	0.466	11.29
MACS J1108.8+0906	3252	11:08:55.393	+09:05:51.16	9.9	VF	I3	0.449	8.96
MACS J1108.8+0906	5009	11:08:55.402	+09:05:51.14	24.5	VF	I3	0.449	8.96
MACS J1115.2+5320	3253	11:15:15.632	+53:20:03.71	8.8	VF	I3	0.439	14.29
MACS J1115.2+5320	5008	11:15:15.636	+53:20:03.74	18.0	VF	I3	0.439	14.29
MACS J1115.2+5320	5350	11:15:15.632	+53:20:03.77	6.9	VF	I3	0.439	14.29
MACS J1115.8+0129	3275	11:15:52.048	+01:29:56.56	15.9	VF	I3	0.120	1.47
MACS J1131.8-1955	3276	11:31:56.011	-19:55:55.85	13.9	VF	I3	0.307	17.45
MACS J1149.5+2223	1656	11:49:35.856	+22:23:55.02	18.5	VF	I3	0.544	21.60
MACS J1149.5+2223	3589	11:49:35.858	+22:23:55.05	20.0	VF	I3	0.544	21.60
MACS J1206.2-0847	3277	12:06:12.276	-08:48:02.40	23.5	VF	I3	0.440	37.02
MACS J1226.8+2153	3590	12:26:51.207	+21:49:55.22	19.0	VF	I3	0.370	2.63
MACS J1311.0-0310	3258	13:11:01.685	-03:10:39.70	14.9	VF	I3	0.494	10.03
MACS J1311.0-0310	6110	13:11:01.680	-03:10:39.75	63.2	VF	I3	0.494	10.03
MACS J1319+7003	3278	13:20:08.370	+70:04:33.81	21.6	VF	I3	0.328	7.03
MACS J1427.2+4407	6112	14:27:16.175	+44:07:30.33	9.4	VF	I3	0.477	14.18
MACS J1427.6-2521	3279	14:27:39.389	-25:21:04.66	16.9	VF	I3	0.220	1.55
MACS J1621.3+3810	3254	16:21:25.552	+38:09:43.56	9.8	VF	I3	0.461	11.49
MACS J1621.3+3810	3594	16:21:25.558	+38:09:43.54	19.7	VF	I3	0.461	11.49
MACS J1621.3+3810	6109	16:21:25.555	+38:09:43.54	37.5	VF	I3	0.461	11.49
MACS J1621.3+3810	6172	16:21:25.559	+38:09:43.53	29.8	VF	I3	0.461	11.49
MACS J1731.6+2252	3281	17:31:39.902	+22:52:00.55	20.5	VF	I3	0.366	9.32
MACS J1824.3+4309	3255	18:24:18.444	+43:09:43.39	14.9	VF	I3	0.487	2.48
MACS J1931.8-2634	3282	19:31:49.656	-26:34:33.99	13.6	VF	I3	0.352	23.14
MACS J2046.0-3430	5816	20:46:00.522	-34:30:15.50	10.0	VF	I3	0.413	5.79
MACS J2049.9-3217	3283	20:49:56.245	-32:16:52.30	23.8	VF	I3	0.325	8.71
MACS J2211.7-0349	3284	22:11:45.856	-03:49:37.24	17.7	VF	I3	0.270	22.11
MACS J2214.9-1359	3259	22:14:57.487	-14:00:09.35	19.5	VF	I3	0.503	24.05
MACS J2214.9-1359	5011	22:14:57.481	-14:00:09.39	18.5	VF	I3	0.503	24.05
MACS J2228+2036	3285	22:28:33.241	+20:37:11.42	19.9	VF	I3	0.412	17.92
MACS J2229.7-2755	3286	22:29:45.358	-27:55:38.41	16.4	VF	I3	0.324	9.49
MACS J2243.3-0935	3260	22:43:21.537	-09:35:44.30	20.5	VF	I3	0.101	0.78
MACS J2245.0+2637	3287	22:45:04.547	+26:38:07.88	16.9	VF	I3	0.304	9.36
MACS J2311+0338	3288	23:11:33.213	+03:38:06.51	13.6	VF	I3	0.300	10.98
MKW3S	900	15:21:51.930	+07:42:31.97	57.3	VF	I3	0.045	1.14
MS 0016.9+1609	520	00:18:33.503	+16:26:12.99	67.4	VF	I3	0.541	32.94
MS 0302.7+1658	525	03:05:31.614	+17:10:02.06	10.0	VF	I3	0.424	2.41
MS 0440.5+0204 ‡	4196	04:43:09.952	+02:10:18.70	59.4	VF	S3	0.190	2.17
MS 0451.6-0305	902	04:54:11.004	-03:00:52.19	44.2	F	S3	0.539	33.32
MS 0735.6+7421	4197	07:41:44.245	+74:14:38.23	45.5	VF	S3	0.216	7.57
MS 0839.8+2938	2224	08:42:55.969	+29:27:26.97	29.8	F	S3	0.194	3.10
MS 0906.5+1110	924	09:09:12.753	+10:58:32.00	29.7	VF	I3	0.163	4.64
MS 1006.0+1202	925	10:08:47.194	+11:47:55.99	29.4	VF	I3	0.221	4.75
MS 1008.1-1224	926	10:10:32.312	-12:39:56.80	44.2	VF	I3	0.301	6.44
MS 1054.5-0321	512	10:56:58.499	-03:37:32.76	89.1	F	S3	0.830	27.22
MS 1455.0+2232	4192	14:57:15.088	+22:20:32.49	91.9	VF	I3	0.259	10.25
MS 1621.5+2640	546	16:23:35.522	+26:34:25.67	30.1	F	I3	0.426	6.49
MS 2053.7-0449	1667	20:56:21.295	-04:37:46.81	44.5	VF	I3	0.583	2.96
MS 2053.7-0449	551	20:56:21.297	-04:37:46.80	44.3	F	I3	0.583	2.96
MS 2137.3-2353	4974	21:40:15.178	-23:39:40.71	57.4	VF	S3	0.313	11.28
MS J1157.3+5531 ‡	4964	11:59:52.295	+55:32:05.61	75.1	VF	S3	0.081	0.12
NGC 6338 ‡	4194	17:15:23.036	+57:24:40.29	47.3	VF	I3	0.028	0.13
PKS 0745-191	6103	07:47:31.469	-19:17:40.01	10.3	VF	I3	0.103	18.41
RBS 0797	2202	09:47:12.971	+76:23:13.90	11.7	VF	I3	0.354	26.07
RDCS 1252-29	4198	12:52:54.221	-29:27:21.01	163.4	VF	I3	1.237	2.28
RX J0232.2-4420	4993	02:32:18.771	-44:20:46.68	23.4	VF	I3	0.284	18.17
RX J0340-4542	6954	03:40:44.765	-45:41:18.41	17.9	VF	I3	0.082	0.33
RX J0439+0520	527	04:39:02.218	+05:20:43.11	9.6	VF	I3	0.208	3.57
RX J0439.0+0715	1449	04:39:00.710	+07:16:07.65	6.3	F	I3	0.230	9.44
RX J0439.0+0715	3583	04:39:00.710	+07:16:07.63	19.2	VF	I3	0.230	9.44
RX J0528.9-3927	4994	05:28:53.039	-39:28:15.53	22.5	VF	I3	0.263	12.99
RX J0647.7+7015	3196	06:47:50.029	+70:14:49.66	19.3	VF	I3	0.584	26.48
RX J0647.7+7015	3584	06:47:50.024	+70:14:49.69	20.0	VF	I3	0.584	26.48
RX J0819.6+6336 ‡	2199	08:19:26.007	+63:37:26.53	14.9	F	S3	0.119	0.98
RX J0910+5422	2452	09:10:44.478	+54:22:03.77	65.3	VF	I3	1.100	1.33
RX J1053+5735	4936	10:53:39.844	+57:35:18.42	92.2	F	S3	1.140	1.59
RX J1347.5-1145	3592	13:47:30.593	-11:45:10.25	57.7	VF	I3	0.451	100.36
RX J1347.5-1145	507	13:47:30.598	-11:45:10.27	10.0	F	S3	0.451	100.36
RX J1350+6007	2229	13:50:48.038	+60:07:08.39	58.3	VF	I3	0.804	2.19
RX J1423.8+2404	1657	14:23:47.759	+24:04:40.65	18.5	VF	I3	0.545	15.84
RX J1423.8+2404	4195	14:23:47.763	+24:04:40.63	115.6	VF	S3	0.545	15.84
RX J1504.1-0248	5793	15:04:07.415	-02:48:15.70	39.2	VF	I3	0.215	34.64
RX J1525+0958	1664	15:24:39.729	+09:57:44.42	50.9	VF	I3	0.516	3.29
RX J1532.9+3021	1649	15:32:55.642	+30:18:57.69	9.4	VF	S3	0.345	20.77
RX J1532.9+3021	1665	15:32:55.641	+30:18:57.61	10.0	VF	I3	0.345	20.77

TABLE 1 — *Continued*

Cluster	Obs.ID	R.A. hr:min:sec	Dec. ° : ' : "	ExpT ksec	Mode	ACIS	z	L_{bol} . 10^{44} ergs s $^{-1}$
(1)	(2)	(3)	(4)	(5)	(6)	(7)	(8)	(9)
RX J1716.9+6708	548	17:16:49.015	+67:08:25.80	51.7	F	I3	0.810	8.04
RX J1720.1+2638	4361	17:20:09.941	+26:37:29.11	25.7	VF	I3	0.164	11.39
RX J1720.2+3536	3280	17:20:16.953	+35:36:23.63	20.8	VF	I3	0.391	13.02
RX J1720.2+3536	6107	17:20:16.949	+35:36:23.68	33.9	VF	I3	0.391	13.02
RX J1720.2+3536	7225	17:20:16.947	+35:36:23.69	2.0	VF	I3	0.391	13.02
RX J2011.3-5725	4995	20:11:26.889	-57:25:09.08	24.0	VF	I3	0.279	2.77
RX J2129.6+0005	552	21:29:39.944	+00:05:18.83	10.0	VF	I3	0.235	12.56
S0463	6956	04:29:07.040	-53:49:38.02	29.3	VF	I3	0.099	22.19
S0463	7250	04:29:07.063	-53:49:38.11	29.1	VF	I3	0.099	22.19
TRIANG AUSTR ‡	1281	16:38:22.712	-64:21:19.70	11.4	F	I3	0.051	9.41
V 1121.0+2327	1660	11:20:57.195	+23:26:27.60	71.3	VF	I3	0.560	3.28
ZWCL 1215	4184	12:17:40.787	+03:39:39.42	12.1	VF	I3	0.075	3.49
ZWCL 1358+6245	516	13:59:50.526	+62:31:04.57	54.1	F	S3	0.328	12.42
ZWCL 1953	1659	08:50:06.677	+36:04:16.16	24.9	F	I3	0.380	17.11
ZWCL 3146	909	10:23:39.735	+04:11:08.05	46.0	F	I3	0.290	29.59
ZWCL 5247	539	12:34:21.928	+09:47:02.83	9.3	VF	I3	0.229	4.87
ZWCL 7160	543	14:57:15.158	+22:20:33.85	9.9	F	I3	0.258	10.14
ZWICKY 2701	3195	09:52:49.183	+51:53:05.27	26.9	VF	S3	0.210	5.19
ZwCL 1332.8+5043	5772	13:34:20.698	+50:31:04.64	19.5	VF	I3	0.620	4.46
ZwCL 0848.5+3341	4205	08:51:38.873	+33:31:08.00	11.4	VF	S3	0.371	4.58

NOTE. — (1) Cluster name, (2) CDA observation identification number, (3) R.A. of cluster center, (4) Dec. of cluster center, (5) nominal exposure time, (6) observing mode, (7) CCD location of centroid, (8) redshift, (9) bolometric luminosity. A (‡) indicates a cluster analyzed within R_{5000} only. Italicized cluster names indicate a cluster which was excluded from our analysis (discussed in §5.1). For clusters with multiple observations, the X-ray centers differ by < 0.5 kpc.

TABLE 2
SUMMARY OF TWO-COMPONENT SIMULATIONS

T_2 keV	ξ_{min} —	T_2 keV	ξ_{min} —
Idealized Spectra		Observation-Specific Spectra	
0.50	$\geq 12\% \pm 4\%$	0.50	$\geq 14.5\% \pm 0.1\%$
0.75	$\geq 12\% \pm 4\%$	0.75	$\geq 11.7\% \pm 0.1\%$
1.00	$\geq 8\% \pm 3\%$	1.00	$\geq 11.6\% \pm 0.1\%$
1.25	$\geq 17\% \pm 3\%$
1.50	$\geq 23\% \pm 5\%$
1.75	$\geq 28\% \pm 4\%$
2.00	none	2.00	$\geq 25.5\% \pm 0.1\%$
3.00	none	3.00	$\geq 28.9\% \pm 0.1\%$

NOTE. — This table summarizes the results of the two temperature component spectra simulations for the ideal and observation-specific cases (see §5.2 for details). The parameter ξ_{min} represents the minimum fractional contribution of the cooler component, T_2 , to the overall count rate in order to produce $T_{HBR} \geq 1.1$ at 90% confidence. The results for the observation-specific spectra are for spectra with $N_{counts} > 15,000$.

TABLE 3
WEIGHTED AVERAGES FOR VARIOUS APERTURES

	[0.7-7.0] keV	[2.0-7.0] keV	T_{HBR}	[0.7-7.0] keV	[2.0-7.0] keV	T_{HBR}
Aperture	Without Core			With Core		
R ₂₅₀₀	4.93±0.03	6.24±0.07	1.16±0.01	4.47±0.02	5.45±0.05	1.13±0.01
R ₅₀₀₀	4.75±0.02	5.97±0.07	1.14±0.01	4.27±0.02	5.29±0.05	1.14±0.01
Simulated	3.853±0.004	4.457±0.009	1.131±0.002
Control	4.208±0.003	4.468±0.006	1.002±0.001

NOTE. — Quoted errors are standard deviation of the mean calculated using an unbiased estimator for weighted samples. Simulated sample has been culled to include only $T_2=0.75$ keV.

TABLE 4
CLUSTERS WITH $T_{HBR} > 1.1$ WITH 90% CONFIDENCE.

Name	T_{HBR}	Merger?	Core Class	T_{dec}	X-ray Morphology	Ref.
RX J1525+0958	1.86 $^{+0.83}_{-0.51}$	Y	CC	0.42 $^{+0.14}_{-0.08}$	Arrowhead shape & no discernible core	[29]
MS 1008.1-1224 ...	1.59 $^{+0.37}_{-0.14}$	Y	NCC	0.93 $^{+0.19}_{-0.14}$	Wide gas tail extending ≈ 550 kpc north	[1]
ABELL 2034	1.40 $^{+0.27}_{-0.11}$	Y	NCC	1.07 $^{+0.17}_{-0.09}$	Prominent cold front & gas tail extending south	[2]
ABELL 401	1.37 $^{+0.12}_{-0.10}$	Y	NCC	1.13 $^{+0.12}_{-0.10}$	Highly spherical & possible cold front to north	[3]
ABELL 1689	1.36 $^{+0.14}_{-0.12}$	Y	NCC	0.95 $^{+0.09}_{-0.07}$	Exceptionally spherical & bright central core	[6],[7]
RX J0439.0+0715 ..	1.42 $^{+0.24}_{-0.18}$	Unknown	NCC	0.98 $^{+0.11}_{-0.09}$	Bright core & possible cold front to north	[29]
ABELL 3376	1.33 $^{+0.11}_{-0.10}$	Y	NCC	0.97 $^{+0.07}_{-0.07}$	Highly disturbed & broad gas tail to west	[4],[5]

TABLE 4 — *Continued*

Name	T_{HBR}	Merger?	Core Class	T_{dec}	X-ray Morphology	Ref.
ABELL 2255	$1.32^{+0.12}_{-0.19}$	Y	NCC	$1.48^{+0.32}_{-0.23}$	Spherical & compressed isophotes west of core	[8],[9]
ABELL 2218	$1.36^{+0.15}_{-0.15}$	Y	NCC	$1.39^{+0.19}_{-0.19}$	Spherical, core of cluster elongated NW-SE	[10]
ABELL 1763	$1.48^{+0.39}_{-0.26}$	Y	NCC	$0.83^{+0.17}_{-0.13}$	Elongated ENE-SSW & cold front to west of core	[11],[12]
MACS J2243.3-0935	$1.76^{+0.42}_{-0.57}$	Unknown	NCC	$1.73^{+0.44}_{-0.32}$	No core & highly flattened along WNW-ESE axis	[29]
ABELL 2069	$1.32^{+0.17}_{-0.14}$	Y	NCC	$1.00^{+0.18}_{-0.14}$	No core & highly elongated NNW-SSE	[13]
ABELL 2384	$1.31^{+0.16}_{-0.14}$	Unknown	CC	$0.59^{+0.03}_{-0.03}$	Gas tail extending 1.1 Mpc from core	[29]
ABELL 168	$1.31^{+0.16}_{-0.14}$	Y	NCC	$1.16^{+0.14}_{-0.10}$	Highly disrupted & irregular	[14],[15]
ABELL 209	$1.38^{+0.23}_{-0.22}$	Y	NCC	$1.08^{+0.10}_{-0.17}$	Asymmetric core structure & possible cold front	[16]
ABELL 665	$1.29^{+0.15}_{-0.13}$	Y	NCC	$1.14^{+0.19}_{-0.15}$	Wide, broad gas tail to north & cold front	[17]
1E0657-56	$1.21^{+0.06}_{-0.05}$	Y	NCC	$1.04^{+0.08}_{-0.08}$	The famous “Bullet Cluster”	[18]
MACS J0547.0-3904	$1.51^{+0.50}_{-0.36}$	Unknown	NCC	$0.77^{+0.14}_{-0.18}$	Bright core & gas spur extending NW	[29]
ZWCL 1215	$1.31^{+0.21}_{-0.18}$	Unknown	NCC	$0.95^{+0.15}_{-0.12}$	No core, flattened along NE-SW axis	[29]
ABELL 1204	$1.26^{+0.14}_{-0.05}$	Unknown	NCC	$0.96^{+0.05}_{-0.05}$	Highly spherical & bright centralized core	[29]
MKW3S	$1.17^{+0.05}_{-0.05}$	Y	CC	$0.87^{+0.02}_{-0.02}$	High mass group, egg shaped & bright core	[19]
MACS J2311+0338	$1.53^{+0.69}_{-0.37}$	Unknown	NCC	$0.69^{+0.20}_{-0.20}$	Elongated N-S & disc-like core	[29]
ABELL 267	$1.33^{+0.21}_{-0.21}$	Unknown	NCC	$1.09^{+0.20}_{-0.16}$	Elongated NNE-SSW & cold front to north	[29]
RX J1720.1+2638	$1.22^{+0.12}_{-0.11}$	Y	CC	$0.73^{+0.04}_{-0.04}$	Very spherical, bright peaky core, & cold front	[20]
ABELL 907	$1.21^{+0.10}_{-0.08}$	Unknown	CC	$0.76^{+0.03}_{-0.03}$	NW-SW elongation & western cold front	[29]
ABELL 514	$1.26^{+0.19}_{-0.15}$	Y	NCC	$1.56^{+1.07}_{-0.40}$	Very diffuse & disrupted	[21]
ABELL 1651	$1.24^{+0.16}_{-0.13}$	Y	NCC	$1.07^{+0.10}_{-0.08}$	Spherical & compressed isophotes to SW	[22]
3C 28.0	$1.23^{+0.14}_{-0.12}$	Y	CC	$0.54^{+0.03}_{-0.03}$	Obvious merger & ~ 1 Mpc gas tail	[23]
R_{5000}-CORE Only						
TRIANG AUSTR ..	$1.42^{+0.14}_{-0.05}$	Y	NCC	$0.90^{+0.06}_{-0.05}$	Highly diffuse & no bright core	[24]
ABELL 3158	$1.23^{+0.05}_{-0.05}$	Y	NCC	$1.15^{+0.05}_{-0.05}$	Large centroid variation	[25]
ABELL 2256	$1.29^{+0.13}_{-0.12}$	Y	NCC	$1.40^{+0.15}_{-0.04}$	Spiral shaped & distinct NW edge	[26]
NGC 6338	$1.22^{+0.10}_{-0.12}$	Unknown	NCC	$0.96^{+0.03}_{-0.03}$	Disrupted group companion to north	[29]
ABELL 2029	$1.21^{+0.12}_{-0.10}$	Y	CC	$0.86^{+0.04}_{-0.04}$	Possible cold front to W & WAT radio source	[27],[28]

NOTE. — Clusters ordered by lower limit of T_{HBR} . Listed T_{HBR} values are for the R_{2500} -CORE aperture, with the exception of the “ R_{5000} -CORE Only” clusters listed at the end of the table. Excluding the “ R_{5000} -CORE Only” clusters, all clusters listed here had T_{HBR} significantly greater than 1.1 and the same core classification for both the R_{2500} -CORE and R_{5000} -CORE apertures. [1] Gioia & Luppino (1994), [2] Kempner et al. (2003), [3] Yuan et al. (2005), [4] Markevitch et al. (1998), [5] Bagchi et al. (2006), [6] Teague et al. (1990), [7] Andersson & Madejski (2004), [8] Burns et al. (1995), [9] Feretti et al. (1997), [10] Girardi et al. (1997), [11] Dahle et al. (2002), [12] Smith et al. (2005), [13] Gioia et al. (1982), [14] Hallman & Markevitch (2004), [15] Yang et al. (2004), [16] Mercurio et al. (2003), [17] Gómez et al. (2000), [18] Tucker et al. (1998), [19] Krepec-Krygier & Krygier (1999), [20] Mazzotta et al. (2001b), [21] Govoni et al. (2001), [22] Bliton et al. (1998), [23] Gutiérrez & Krawczynski (2005), [24] Markevitch et al. (1996), [25] Ohta et al. (2001), [26] Molendi et al. (2000), [27] Clarke et al. (2004), [28] Clarke et al. (2005), [29] this work.

TABLE 5
SUMMARY OF EXCISED R_{2500} SPECTRAL FITS

Cluster	R_{CORE}	R_{2500}	N_{HI}	T_{77}	T_{27}	T_{HBR}	Z_{77}	$\chi^2_{red,77}$	$\chi^2_{red,27}$	% Source
(1)	kpc	kpc	10^{20} cm^{-2}	keV	keV	(7)	Z_{\odot}	(9)	(10)	(11)
1E0657 56 *	69	688	6.53	$11.99^{+0.27}_{-0.26}$	$14.54^{+0.67}_{-0.53}$	$1.21^{+0.06}_{-0.05}$	$0.29^{+0.03}_{-0.02}$	1.24	1.11	92
1RXS J2129.4-0741 *	71	526	4.36	$8.22^{+1.18}_{-0.95}$	$8.10^{+1.47}_{-1.0}$	$0.99^{+0.23}_{-0.18}$	$0.43^{+0.18}_{-0.16}$	1.07	1.05	80
2PIGG J0011.5-2850	69	547	2.18	$5.15^{+0.25}_{-0.24}$	$6.20^{+0.40}_{-0.65}$	$1.20^{+0.14}_{-0.14}$	$0.26^{+0.09}_{-0.08}$	1.09	1.00	70
2PIGG J2227.0-3041	69	378	1.11	$2.80^{+0.15}_{-0.14}$	$2.97^{+0.34}_{-0.27}$	$1.06^{+0.13}_{-0.11}$	$0.35^{+0.09}_{-0.08}$	1.16	1.15	69
3C 220.1	71	456	1.91	$9.26^{+14.71}_{-9.8}$	$8.00^{+17.66}_{-10.5}$	$0.86^{+2.35}_{-0.57}$	$0.00^{+0.59}_{-0.08}$	1.20	1.40	30
3C 28.0	70	420	5.71	$5.53^{+0.29}_{-0.27}$	$6.81^{+0.60}_{-0.60}$	$1.23^{+0.14}_{-0.12}$	$0.30^{+0.08}_{-0.07}$	0.98	0.88	87
3C 295	69	465	1.35	$5.16^{+0.42}_{-0.38}$	$5.93^{+0.84}_{-0.69}$	$1.15^{+0.19}_{-0.16}$	$0.38^{+0.12}_{-0.11}$	0.91	0.93	79
3C 388	69	420	6.11	$3.23^{+0.23}_{-0.21}$	$3.26^{+0.49}_{-0.40}$	$1.01^{+0.17}_{-0.09}$	$0.51^{+0.16}_{-0.07}$	0.95	0.95	68
4C 55.16	69	426	4.00	$4.98^{+0.17}_{-0.17}$	$5.54^{+0.36}_{-0.36}$	$1.11^{+0.08}_{-0.08}$	$0.49^{+0.07}_{-0.07}$	0.89	0.80	58
ABELL 0068	70	680	4.60	$9.01^{+1.53}_{-1.14}$	$9.13^{+2.60}_{-1.71}$	$1.01^{+0.34}_{-0.23}$	$0.46^{+0.24}_{-0.22}$	1.15	1.13	79
ABELL 0168 *	70	398	3.27	$2.56^{+0.11}_{-0.08}$	$3.36^{+0.37}_{-0.35}$	$1.31^{+0.16}_{-0.14}$	$0.29^{+0.06}_{-0.04}$	1.07	1.03	40
ABELL 0209 *	70	609	1.68	$7.30^{+0.59}_{-0.51}$	$10.07^{+1.91}_{-1.41}$	$1.38^{+0.28}_{-0.22}$	$0.23^{+0.10}_{-0.09}$	1.12	1.11	82
ABELL 0267 *	70	545	2.74	$6.70^{+0.56}_{-0.47}$	$8.88^{+1.68}_{-1.27}$	$1.33^{+0.27}_{-0.27}$	$0.32^{+0.11}_{-0.11}$	1.18	1.15	82
ABELL 0370	69	516	3.37	$7.35^{+0.84}_{-0.84}$	$10.35^{+2.27}_{-2.27}$	$1.41^{+0.35}_{-0.35}$	$0.45^{+0.06}_{-0.23}$	1.08	1.04	39
ABELL 0383	69	423	4.07	$4.91^{+0.29}_{-0.27}$	$5.42^{+0.74}_{-0.59}$	$1.10^{+0.16}_{-0.13}$	$0.44^{+0.11}_{-0.11}$	0.97	0.90	64
ABELL 0399	69	546	$7.57^{+0.71}_{-0.71}$	$7.95^{+0.35}_{-0.19}$	$8.87^{+0.55}_{-0.50}$	$1.12^{+0.08}_{-0.08}$	$0.30^{+0.05}_{-0.05}$	1.12	0.99	82
ABELL 0401	69	643	12.48	$6.37^{+0.19}_{-0.19}$	$8.71^{+0.92}_{-0.61}$	$1.37^{+0.98}_{-0.10}$	$0.26^{+0.05}_{-0.06}$	1.44	1.05	78
ABELL 0478	69	598	30.90	$7.30^{+0.26}_{-0.24}$	$8.62^{+0.58}_{-0.54}$	$1.18^{+0.09}_{-0.08}$	$0.45^{+0.06}_{-0.05}$	1.05	0.95	91
ABELL 0514	71	516	3.14	$3.33^{+0.16}_{-0.16}$	$4.02^{+0.54}_{-0.46}$	$1.21^{+0.17}_{-0.12}$	$0.25^{+0.08}_{-0.07}$	1.07	0.97	53
ABELL 0520	70	576	$1.06^{+1.06}_{-1.05}$	$9.29^{+0.67}_{-0.60}$	$9.88^{+0.85}_{-0.73}$	$1.06^{+0.12}_{-0.10}$	$0.37^{+0.09}_{-0.07}$	1.11	1.04	87
ABELL 0521	70	558	6.17	$7.03^{+0.59}_{-0.53}$	$8.39^{+1.62}_{-1.46}$	$1.19^{+0.25}_{-0.20}$	$0.39^{+0.13}_{-0.17}$	1.10	1.15	49
ABELL 0586	70	635	4.71	$6.47^{+0.47}_{-0.47}$	$8.06^{+1.11}_{-1.11}$	$1.25^{+0.30}_{-0.19}$	$0.56^{+0.17}_{-0.16}$	0.91	0.81	82
ABELL 0611	70	523	4.99	$7.06^{+0.55}_{-0.48}$	$7.97^{+1.09}_{-0.91}$	$1.13^{+0.18}_{-0.15}$	$0.35^{+0.11}_{-0.10}$	0.97	0.98	54
ABELL 0665	69	617	4.24	$7.45^{+0.38}_{-0.34}$	$9.61^{+1.02}_{-0.85}$	$1.29^{+0.15}_{-0.13}$	$0.31^{+0.06}_{-0.07}$	1.02	0.93	87
ABELL 0697	69	612	3.34	$9.52^{+0.87}_{-0.76}$	$12.24^{+2.05}_{-1.63}$	$1.29^{+0.23}_{-0.20}$	$0.37^{+0.12}_{-0.11}$	1.08	1.02	89
ABELL 0773	69	615	1.46	$7.83^{+0.66}_{-0.57}$	$9.75^{+1.65}_{-1.27}$	$1.25^{+0.24}_{-0.19}$	$0.44^{+0.12}_{-0.12}$	1.06	1.09	84

TABLE 5 — *Continued*

Cluster	R _{CORE}	R ₂₅₀₀	N _H	T ₇₇	T ₂₇	T _{HBR}	Z ₇₇	$\chi^2_{red,77}$	$\chi^2_{red,27}$	% Source
(1)	kpc (2)	kpc (3)	10 ²⁰ cm ⁻² (4)	keV (5)	keV (6)	(7)	Z _⊙ (8)	(9)	(10)	(11)
ABELL 0907	69	488	5.69	5.62 ^{+0.18} _{-0.17}	6.78 ^{+0.49} _{-0.43}	1.21 ^{+0.10} _{-0.08}	0.42 ^{+0.06} _{-0.05}	1.13	1.00	88
ABELL 0963	69	543	1.39	6.73 ^{+0.32} _{-0.30}	6.98 ^{+0.66} _{-0.57}	1.04 ^{+0.11} _{-0.10}	0.29 ^{+0.07} _{-0.08}	1.06	1.02	64
ABELL 1063S	69	648	1.77	11.96 ^{+0.88} _{-0.79}	13.70 ^{+1.68} _{-1.38}	1.15 ^{+0.16} _{-0.16}	0.38 ^{+0.09} _{-0.09}	1.02	0.98	90
ABELL 1204	70	419	1.44	3.63 ^{+0.18} _{-0.16}	4.58 ^{+0.57} _{-0.45}	1.26 ^{+0.17} _{-0.14}	0.31 ^{+0.09} _{-0.09}	1.06	0.90	88
ABELL 1423	70	614	1.60	6.01 ^{+0.75} _{-0.64}	7.53 ^{+2.35} _{-1.5}	1.25 ^{+0.42} _{-0.29}	0.30 ^{+0.18} _{-0.17}	0.87	0.65	78
ABELL 1651	70	596	2.02	6.26 ^{+0.30} _{-0.27}	7.78 ^{+0.90} _{-0.76}	1.24 ^{+0.16} _{-0.13}	0.42 ^{+0.09} _{-0.09}	1.19	1.20	86
ABELL 1689 *	70	679	1.87	9.48 ^{+0.38} _{-0.35}	12.89 ^{+1.23} _{-1.01}	1.36 ^{+0.14} _{-0.12}	0.36 ^{+0.06} _{-0.05}	1.13	1.02	91
ABELL 1758	69	574	1.09	12.14 ^{+0.92} _{-0.92}	11.16 ^{+3.08} _{-2.14}	0.92 ^{+0.27} _{-0.19}	0.56 ^{+0.13} _{-0.13}	1.21	1.09	58
ABELL 1763	69	561	0.82	7.78 ^{+0.67} _{-0.60}	11.49 ^{+2.89} _{-1.84}	1.48 ^{+0.39} _{-0.26}	0.25 ^{+0.11} _{-0.10}	1.12	0.92	84
ABELL 1835	70	570	2.36	9.77 ^{+0.57} _{-0.52}	11.00 ^{+1.23} _{-1.03}	1.13 ^{+0.14} _{-0.12}	0.31 ^{+0.08} _{-0.07}	0.98	1.02	86
ABELL 1914	70	698	0.97	9.62 ^{+0.55} _{-0.49}	11.42 ^{+1.26} _{-1.06}	1.19 ^{+0.15} _{-0.13}	0.30 ^{+0.08} _{-0.07}	1.07	1.03	92
ABELL 1942	69	473	2.75	4.77 ^{+0.38} _{-0.35}	5.49 ^{+0.98} _{-0.74}	1.15 ^{+0.22} _{-0.18}	0.33 ^{+0.12} _{-0.14}	1.06	1.04	70
ABELL 1995	71	381	1.44	8.37 ^{+0.70} _{-0.61}	9.23 ^{+1.44} _{-1.13}	1.10 ^{+0.20} _{-0.16}	0.39 ^{+0.12} _{-0.11}	1.02	0.96	74
ABELL 2034	69	594	1.58	7.15 ^{+0.22} _{-0.22}	10.02 ^{+0.92} _{-0.75}	1.40 ^{+0.11} _{-0.11}	0.32 ^{+0.05} _{-0.05}	1.22	1.00	84
ABELL 2069	70	623	1.97	6.50 ^{+0.33} _{-0.29}	8.61 ^{+1.02} _{-0.84}	1.32 ^{+0.17} _{-0.14}	0.26 ^{+0.08} _{-0.07}	1.04	0.96	71
ABELL 2111	70	592	2.20	7.13 ^{+0.29} _{-0.29}	11.10 ^{+4.67} _{-3.05}	1.56 ^{+0.71} _{-0.48}	0.13 ^{+0.19} _{-0.13}	1.06	0.88	76
ABELL 2125	70	371	2.75	2.88 ^{+0.30} _{-0.27}	3.76 ^{+0.98} _{-0.65}	1.31 ^{+0.39} _{-0.26}	0.31 ^{+0.13} _{-0.16}	1.26	1.30	61
ABELL 2163	69	751	12.04	19.20 ^{+0.87} _{-0.80}	21.30 ^{+1.77} _{-1.47}	1.11 ^{+0.11} _{-0.09}	0.10 ^{+0.06} _{-0.06}	1.37	1.26	90
ABELL 2204	70	575	5.84	8.65 ^{+0.58} _{-0.59}	10.57 ^{+1.48} _{-1.23}	1.22 ^{+0.19} _{-0.19}	0.37 ^{+0.10} _{-0.10}	0.95	1.00	90
ABELL 2218	70	558	3.12	7.35 ^{+0.39} _{-0.35}	10.03 ^{+1.26} _{-0.98}	1.36 ^{+0.19} _{-0.15}	0.22 ^{+0.07} _{-0.06}	1.01	0.90	87
ABELL 2255	71	596	2.53	6.12 ^{+0.20} _{-0.19}	8.10 ^{+0.66} _{-0.58}	1.32 ^{+0.12} _{-0.10}	0.30 ^{+0.06} _{-0.06}	1.13	0.95	76
ABELL 2259	69	480	3.70	5.18 ^{+0.46} _{-0.39}	6.40 ^{+1.33} _{-0.95}	1.24 ^{+0.28} _{-0.21}	0.41 ^{+0.14} _{-0.14}	1.05	1.01	85
ABELL 2261	69	576	3.31	7.63 ^{+0.47} _{-0.43}	9.30 ^{+1.21} _{-0.91}	1.22 ^{+0.18} _{-0.14}	0.36 ^{+0.08} _{-0.08}	0.99	0.95	90
ABELL 2294	69	572	6.10	9.98 ^{+1.43} _{-1.12}	11.07 ^{+3.19} _{-2.11}	1.11 ^{+0.36} _{-0.25}	0.53 ^{+0.21} _{-0.21}	1.07	0.95	82
ABELL 2384	70	436	2.99	4.75 ^{+0.20} _{-0.20}	6.22 ^{+0.72} _{-0.60}	1.31 ^{+0.14} _{-0.14}	0.23 ^{+0.07} _{-0.07}	1.06	0.92	81
ABELL 2409	70	511	6.72	5.94 ^{+0.43} _{-0.38}	6.77 ^{+0.99} _{-0.82}	1.14 ^{+0.19} _{-0.16}	0.37 ^{+0.13} _{-0.11}	1.13	0.96	88
ABELL 2537	69	497	4.26	8.40 ^{+0.76} _{-0.68}	7.81 ^{+1.15} _{-0.91}	0.93 ^{+0.16} _{-0.13}	0.40 ^{+0.13} _{-0.13}	0.91	0.84	46
ABELL 2631	70	631	3.74	7.06 ^{+0.84} _{-0.78}	7.83 ^{+1.45} _{-1.06}	1.11 ^{+0.24} _{-0.24}	0.34 ^{+0.18} _{-0.18}	0.97	0.88	83
ABELL 2667	70	525	1.64	6.75 ^{+0.48} _{-0.43}	7.45 ^{+1.06} _{-0.88}	1.10 ^{+0.18} _{-0.15}	0.36 ^{+0.11} _{-0.11}	1.17	1.08	76
ABELL 2670	69	451	2.88	3.95 ^{+0.14} _{-0.17}	4.65 ^{+0.42} _{-0.40}	1.18 ^{+0.11} _{-0.11}	0.42 ^{+0.08} _{-0.08}	1.13	1.07	70
ABELL 2717	70	298	1.12	2.63 ^{+0.17} _{-0.16}	3.17 ^{+0.38} _{-0.43}	1.21 ^{+0.23} _{-0.18}	0.48 ^{+0.13} _{-0.10}	0.88	0.87	55
ABELL 2744	71	647	1.82	9.18 ^{+0.68} _{-0.60}	10.20 ^{+1.38} _{-1.10}	1.11 ^{+0.17} _{-0.14}	0.24 ^{+0.10} _{-0.09}	0.99	0.90	67
ABELL 3164	70	451	2.55	2.83 ^{+0.36} _{-0.26}	3.81 ^{+1.42} _{-1.42}	1.35 ^{+0.52} _{-0.52}	0.39 ^{+0.21} _{-0.21}	0.88	0.94	29
ABELL 3376 *	70	463	5.21	4.48 ^{+0.11} _{-0.12}	5.95 ^{+0.47} _{-0.42}	1.33 ^{+0.11} _{-0.10}	0.39 ^{+0.05} _{-0.08}	1.16	1.09	63
ABELL 3921	69	535	3.07	5.70 ^{+0.24} _{-0.24}	6.65 ^{+0.65} _{-0.54}	1.17 ^{+0.12} _{-0.11}	0.31 ^{+0.08} _{-0.07}	1.02	0.96	77
AC 114	70	550	1.44	7.53 ^{+0.49} _{-0.44}	8.30 ^{+1.03} _{-0.85}	1.10 ^{+0.15} _{-0.13}	0.26 ^{+0.08} _{-0.09}	1.07	1.06	55
CL 0024+17	71	435	4.36	6.03 ^{+1.66} _{-1.10}	7.18 ^{+7.91} _{-3.16}	1.19 ^{+1.35} _{-0.57}	0.60 ^{+0.37} _{-0.33}	1.00	1.44	37
CL 1221+4918	71	445	1.44	6.62 ^{+1.24} _{-0.72}	7.11 ^{+1.73} _{-1.21}	1.07 ^{+0.33} _{-0.25}	0.34 ^{+0.20} _{-0.15}	0.94	0.93	62
CL J0030+2618	70	786	4.10	4.63 ^{+1.32} _{-1.32}	5.18 ^{+8.29} _{-1.96}	1.12 ^{+0.53} _{-0.53}	0.26 ^{+0.15} _{-0.26}	1.00	1.23	37
CL J0152-1357	70	391	1.45	7.33 ^{+2.78} _{-1.77}	7.31 ^{+3.43} _{-2.02}	1.00 ^{+0.60} _{-0.37}	0.00 ^{+0.24} _{-0.00}	0.89	1.00	36
CL J0542.8-4100	71	446	3.59	6.07 ^{+1.47} _{-1.25}	6.29 ^{+2.14} _{-1.41}	1.04 ^{+0.33} _{-0.29}	0.16 ^{+0.23} _{-0.16}	1.04	0.91	66
CL J0848+4456 *	71	319	2.53	4.53 ^{+1.57} _{-1.13}	5.52 ^{+3.28} _{-1.74}	1.22 ^{+0.84} _{-0.49}	0.00 ^{+0.45} _{-0.00}	0.92	0.93	58
CL J1113.1-2615	70	435	5.51	4.19 ^{+1.61} _{-1.02}	4.10 ^{+2.47} _{-1.44}	0.98 ^{+0.70} _{-0.42}	0.46 ^{+0.63} _{-0.44}	1.01	1.08	23
CL J1226.9+3332 *	69	450	1.37	11.81 ^{+2.25} _{-1.70}	11.29 ^{+2.45} _{-1.77}	0.96 ^{+0.20} _{-0.20}	0.21 ^{+0.11} _{-0.21}	0.81	0.86	86
CL J2302.8+0844	70	514	5.05	4.25 ^{+1.17} _{-1.32}	4.67 ^{+2.00} _{-1.80}	1.10 ^{+0.56} _{-0.54}	0.13 ^{+0.33} _{-0.13}	0.89	0.97	50
DLS J0514-4904	70	507	2.52	4.62 ^{+0.53} _{-0.47}	6.14 ^{+2.08} _{-1.34}	1.33 ^{+0.48} _{-0.32}	0.37 ^{+0.24} _{-0.20}	1.04	1.12	54
MACS J0011.7-1523 *	69	451	2.08	6.49 ^{+0.48} _{-0.43}	6.76 ^{+0.81} _{-0.66}	1.04 ^{+0.15} _{-0.12}	0.30 ^{+0.10} _{-0.09}	0.86	0.90	87
MACS J0025.4-1222 *	70	473	2.72	6.33 ^{+0.85} _{-0.70}	6.01 ^{+1.05} _{-0.85}	0.95 ^{+0.21} _{-0.17}	0.37 ^{+0.16} _{-0.15}	0.90	0.92	80
MACS J0035.4-2015	70	527	1.55	7.46 ^{+0.79} _{-0.66}	9.31 ^{+1.75} _{-1.29}	1.25 ^{+0.27} _{-0.21}	0.33 ^{+0.12} _{-0.12}	0.94	0.93	90
MACS J0111.5+0855	70	435	4.18	4.11 ^{+1.01} _{-1.05}	3.72 ^{+3.08} _{-1.29}	0.91 ^{+0.83} _{-0.39}	0.11 ^{+0.59} _{-0.11}	0.68	0.65	49
MACS J0152.5-2852	70	459	1.46	5.64 ^{+0.89} _{-0.70}	7.24 ^{+2.57} _{-1.59}	1.28 ^{+0.50} _{-0.32}	0.22 ^{+0.17} _{-0.17}	1.10	1.02	84
MACS J0159.0-3412	70	572	1.54	10.90 ^{+4.77} _{-2.53}	14.65 ^{+12.31} _{-5.39}	1.34 ^{+1.27} _{-0.58}	0.26 ^{+0.15} _{-0.26}	0.87	0.92	81
MACS J0159.8-0849 *	69	585	2.01	9.16 ^{+0.71} _{-0.63}	9.83 ^{+1.13} _{-0.96}	1.07 ^{+0.15} _{-0.13}	0.30 ^{+0.09} _{-0.09}	1.08	1.09	90
MACS J0242.5-2132	70	498	2.71	5.58 ^{+0.63} _{-0.52}	6.26 ^{+1.38} _{-0.99}	1.12 ^{+0.28} _{-0.26}	0.34 ^{+0.16} _{-0.15}	1.03	0.83	87
MACS J0257.1-2325 *	70	579	2.09	9.25 ^{+1.28} _{-1.01}	10.16 ^{+1.95} _{-1.54}	1.10 ^{+0.21} _{-0.21}	0.14 ^{+0.12} _{-0.12}	0.99	1.08	84
MACS J0257.6-2209	69	540	2.02	8.02 ^{+1.12} _{-0.88}	8.17 ^{+1.92} _{-1.30}	1.02 ^{+0.28} _{-0.20}	0.30 ^{+0.16} _{-0.17}	1.12	1.26	84
MACS J0308.9+2645	69	539	11.88	10.54 ^{+1.28} _{-1.07}	11.38 ^{+2.16} _{-1.66}	1.08 ^{+0.24} _{-0.19}	0.28 ^{+0.13} _{-0.13}	0.97	1.01	87
MACS J0329.6-0211 *	70	420	6.21	6.30 ^{+0.47} _{-0.41}	7.50 ^{+0.85} _{-0.69}	1.19 ^{+0.16} _{-0.13}	0.41 ^{+0.10} _{-0.09}	1.10	1.17	86
MACS J0404.6+1109	70	494	14.96	5.77 ^{+1.14} _{-0.88}	6.15 ^{+2.00} _{-1.30}	1.07 ^{+0.41} _{-0.28}	0.24 ^{+0.22} _{-0.20}	0.85	0.78	73
MACS J0417.5-1154	70	429	4.00	11.07 ^{+1.98} _{-1.49}	14.90 ^{+5.03} _{-3.24}	1.35 ^{+0.31} _{-0.34}	0.33 ^{+0.19} _{-0.14}	1.07	0.97	94
MACS J0429.6-0253	69	495	5.70	5.66 ^{+0.64} _{-0.54}	6.71 ^{+1.26} _{-0.98}	1.19 ^{+0.26} _{-0.21}	0.35 ^{+0.14} _{-0.13}	1.21	1.12	82
MACS J0451.9+0006	70	459	7.65	5.80 ^{+1.46} _{-1.03}	7.02 ^{+3.29} _{-1.80}	1.21 ^{+0.64} _{-0.38}	0.51 ^{+0.33} _{-0.29}	1.25	1.35	83
MACS J0455.2+0657	71	481	10.45	7.25 ^{+2.94} _{-1.33}	8.25 ^{+1.80} _{-1.10}	1.14 ^{+0.28} _{-0.26}	0.56 ^{+0.37} _{-0.33}	0.83	0.94	82
MACS J0520.7-1328	69	492	8.88	6.35 ^{+0.81} _{-0.67}	8.22 ^{+2.18} _{-1.45}	1.29 ^{+0.38} _{-0.27}	0.43 ^{+0.17} _{-0.16}	1.23	1.38	86

TABLE 5 — *Continued*

Cluster	R _{CORE}	R ₂₅₀₀	N _H	T ₇₇	T ₂₇	T _{HBR}	Z ₇₇	$\chi^2_{red,77}$	$\chi^2_{red,27}$	% Source
(1)	kpc (2)	kpc (3)	10 ²⁰ cm ⁻² (4)	keV (5)	keV (6)	(7)	Z _⊙ (8)	(9)	(10)	(11)
MACS J0547.0-3904	69	364	4.08	3.58 ^{+0.44} _{-0.37}	5.41 ^{+1.67} _{-1.18}	1.51 ^{+0.50} _{-0.36}	0.09 ^{+0.15} _{-0.09}	1.16	1.42	75
MACS J0553.4-3342	70	692	2.88	13.14 ^{+3.82} _{-2.50}	13.86 ^{+6.45} _{-3.44}	1.05 ^{+0.58} _{-0.33}	0.57 ^{+0.35} _{-0.33}	0.80	0.76	87
MACS J0717.5+3745 *	70	563	6.75	12.77 ^{+1.16} _{-1.00}	13.21 ^{+1.51} _{-1.29}	1.03 ^{+0.33} _{-0.13}	0.30 ^{+0.10} _{-0.11}	0.93	0.90	88
MACS J0744.8+3927 *	70	537	4.66	8.09 ^{+0.77} _{-0.66}	8.77 ^{+1.04} _{-0.87}	1.08 ^{+0.16} _{-0.14}	0.32 ^{+0.10} _{-0.10}	1.14	1.18	82
MACS J0911.2+1746 *	70	541	3.55	7.51 ^{+1.27} _{-0.93}	7.17 ^{+1.60} _{-1.20}	0.95 ^{+0.27} _{-0.20}	0.21 ^{+0.17} _{-0.16}	0.93	0.84	78
MACS J0949+1708	70	580	3.17	9.16 ^{+1.53} _{-1.18}	9.11 ^{+1.55} _{-1.55}	0.99 ^{+0.30} _{-0.21}	0.37 ^{+0.16} _{-0.20}	0.89	0.84	89
MACS J1006.9+3200	70	512	1.83	7.89 ^{+2.78} _{-1.74}	8.05 ^{+3.70} _{-2.45}	1.02 ^{+0.81} _{-0.38}	0.15 ^{+0.35} _{-0.15}	1.84	1.15	76
MACS J1105.7-1014	71	502	4.58	7.54 ^{+2.29} _{-1.51}	7.78 ^{+3.93} _{-1.97}	1.03 ^{+0.61} _{-0.22}	0.22 ^{+0.29} _{-0.22}	1.17	1.27	81
MACS J1108.8+0906 *	70	491	2.52	6.52 ^{+0.94} _{-0.82}	7.31 ^{+1.89} _{-1.29}	1.12 ^{+0.33} _{-0.24}	0.29 ^{+0.18} _{-0.17}	0.95	0.80	80
MACS J1115.2+5320 *	70	527	0.98	8.91 ^{+1.42} _{-1.17}	9.58 ^{+2.36} _{-1.67}	1.08 ^{+0.32} _{-0.23}	0.37 ^{+0.20} _{-0.18}	0.93	0.88	75
MACS J1115.8+0129	70	448	4.36	6.78 ^{+1.17} _{-0.91}	8.27 ^{+3.24} _{-1.16}	1.22 ^{+0.36} _{-0.36}	0.07 ^{+0.21} _{-0.07}	1.00	0.97	65
MACS J1131.8-1955	69	576	4.49	8.64 ^{+1.23} _{-0.97}	11.01 ^{+3.61} _{-2.10}	1.27 ^{+0.46} _{-0.28}	0.42 ^{+0.17} _{-0.17}	1.00	1.00	87
MACS J1149.5+2223 *	69	504	2.32	7.65 ^{+0.89} _{-0.76}	8.13 ^{+1.36} _{-1.04}	1.06 ^{+0.22} _{-0.17}	0.20 ^{+0.12} _{-0.11}	1.00	1.09	87
MACS J1206.2-0847	70	522	4.15	10.21 ^{+1.44} _{-0.97}	12.51 ^{+2.44} _{-1.87}	1.23 ^{+0.28} _{-0.22}	0.33 ^{+0.13} _{-0.13}	0.96	1.05	93
MACS J1226.8+2153	71	489	1.82	4.21 ^{+1.07} _{-0.80}	5.02 ^{+3.29} _{-1.52}	1.19 ^{+0.84} _{-0.43}	0.23 ^{+0.38} _{-0.23}	1.02	0.81	67
MACS J1311.0-0310 *	69	425	2.18	5.76 ^{+0.48} _{-0.42}	5.91 ^{+0.73} _{-0.62}	1.03 ^{+0.15} _{-0.13}	0.39 ^{+0.13} _{-0.13}	0.96	0.98	72
MACS J1319+7003	70	496	1.53	7.99 ^{+2.08} _{-1.43}	10.62 ^{+7.35} _{-3.22}	1.33 ^{+0.98} _{-0.47}	0.30 ^{+0.29} _{-0.28}	1.25	1.24	74
MACS J1427.2+4407	71	488	1.41	9.80 ^{+3.87} _{-2.53}	10.35 ^{+6.30} _{-3.26}	1.06 ^{+0.77} _{-0.43}	0.00 ^{+0.34} _{-0.00}	0.67	0.50	84
MACS J1427.6-2521	71	426	6.11	4.65 ^{+0.92} _{-0.72}	8.11 ^{+5.04} _{-2.77}	1.74 ^{+1.14} _{-0.65}	0.18 ^{+0.26} _{-0.18}	1.19	1.40	68
MACS J1621.3+3810 *	69	504	1.07	7.12 ^{+0.66} _{-0.55}	7.09 ^{+0.92} _{-0.75}	1.00 ^{+0.16} _{-0.13}	0.34 ^{+0.11} _{-0.11}	0.93	0.86	73
MACS J1731.6+2252	71	521	6.48	7.45 ^{+1.32} _{-0.99}	10.99 ^{+4.67} _{-2.46}	1.48 ^{+0.68} _{-0.38}	0.35 ^{+0.19} _{-0.17}	1.20	1.07	84
MACS J1931.8-2634	70	535	9.13	6.97 ^{+0.72} _{-0.61}	7.72 ^{+2.41} _{-0.99}	1.11 ^{+0.22} _{-0.17}	0.27 ^{+0.12} _{-0.12}	0.95	0.86	90
MACS J2046.0-3430	71	386	4.98	4.64 ^{+1.18} _{-0.82}	5.49 ^{+2.29} _{-1.47}	1.18 ^{+0.58} _{-0.38}	0.20 ^{+0.32} _{-0.20}	0.89	1.11	82
MACS J2049.9-3217	69	524	5.99	6.83 ^{+0.84} _{-0.69}	8.94 ^{+2.08} _{-1.48}	1.31 ^{+0.34} _{-0.33}	0.43 ^{+0.17} _{-0.13}	0.99	0.92	83
MACS J2211.7-0349	69	663	5.86	11.30 ^{+1.46} _{-1.17}	13.82 ^{+2.41} _{-2.41}	1.22 ^{+0.33} _{-0.25}	0.15 ^{+0.13} _{-0.14}	1.24	1.26	88
MACS J2214.9-1359 *	70	529	3.32	9.78 ^{+1.38} _{-1.09}	10.45 ^{+2.19} _{-1.56}	1.07 ^{+0.27} _{-0.20}	0.23 ^{+0.14} _{-0.14}	0.99	1.06	87
MACS J2228+2036	70	545	4.52	7.86 ^{+1.08} _{-0.88}	9.17 ^{+2.05} _{-1.46}	1.17 ^{+0.31} _{-0.22}	0.39 ^{+0.16} _{-0.16}	0.99	1.00	88
MACS J2229.7-2755	69	465	1.34	5.01 ^{+0.50} _{-0.43}	5.79 ^{+1.11} _{-0.86}	1.16 ^{+0.25} _{-0.20}	0.55 ^{+0.19} _{-0.18}	1.05	1.08	85
MACS J2243.3-0935	71	574	4.31	4.09 ^{+0.51} _{-0.45}	7.20 ^{+3.17} _{-2.12}	1.76 ^{+0.81} _{-0.55}	0.03 ^{+0.15} _{-0.03}	1.17	0.92	51
MACS J2245.0+2637	69	454	5.50	6.06 ^{+0.65} _{-0.54}	6.76 ^{+1.24} _{-0.93}	1.12 ^{+0.24} _{-0.18}	0.60 ^{+0.20} _{-0.15}	0.94	1.09	88
MACS J2311+0338	70	363	5.23	8.12 ^{+1.44} _{-1.16}	12.40 ^{+5.12} _{-2.88}	1.53 ^{+0.69} _{-0.42}	0.46 ^{+0.13} _{-0.20}	1.07	1.15	88
MKW3S	70	339	3.05	3.91 ^{+0.06} _{-0.06}	4.58 ^{+0.18} _{-0.18}	1.17 ^{+0.05} _{-0.05}	0.34 ^{+0.03} _{-0.04}	1.38	0.97	86
MS 0016.9+1609	69	550	4.06	8.94 ^{+0.71} _{-0.62}	9.78 ^{+1.09} _{-0.90}	1.09 ^{+0.13} _{-0.13}	0.29 ^{+0.09} _{-0.08}	0.91	0.88	83
MS 0451.6-0305	70	536	5.68	8.90 ^{+0.85} _{-0.72}	10.43 ^{+1.39} _{-1.26}	1.17 ^{+0.21} _{-0.17}	0.37 ^{+0.11} _{-0.11}	1.00	0.93	60
MS 0735.6+7421	69	491	3.40	5.55 ^{+0.24} _{-0.20}	6.34 ^{+0.57} _{-0.50}	1.14 ^{+0.11} _{-0.11}	0.35 ^{+0.07} _{-0.06}	1.05	1.05	62
MS 0839.8+2938	70	415	3.92	4.68 ^{+0.32} _{-0.29}	5.05 ^{+0.82} _{-0.65}	1.08 ^{+0.19} _{-0.15}	0.46 ^{+0.13} _{-0.12}	0.90	0.87	60
MS 0906.5+1110	70	616	3.60	5.38 ^{+0.33} _{-0.29}	6.76 ^{+0.92} _{-0.77}	1.26 ^{+0.19} _{-0.16}	0.27 ^{+0.09} _{-0.09}	1.21	1.08	75
MS 1006.0+1202	70	556	3.63	5.61 ^{+0.51} _{-0.43}	7.48 ^{+1.66} _{-1.27}	1.33 ^{+0.32} _{-0.27}	0.24 ^{+0.11} _{-0.11}	1.30	1.34	75
MS 1008.1-1224	70	548	6.71	5.65 ^{+0.43} _{-0.35}	9.01 ^{+1.93} _{-1.38}	1.59 ^{+0.37} _{-0.27}	0.26 ^{+0.11} _{-0.10}	1.21	0.98	78
MS 1054.5-0321	70	558	3.69	9.38 ^{+1.72} _{-1.34}	9.91 ^{+2.66} _{-1.77}	1.06 ^{+0.34} _{-0.24}	0.13 ^{+0.17} _{-0.13}	1.02	1.03	41
MS 1455.0+2232	69	436	3.35	4.77 ^{+0.13} _{-0.13}	5.37 ^{+0.36} _{-0.22}	1.13 ^{+0.08} _{-0.06}	0.44 ^{+0.05} _{-0.05}	1.29	1.10	90
MS 1621.5+2640	70	537	3.59	6.11 ^{+0.95} _{-0.76}	6.22 ^{+1.56} _{-1.10}	1.02 ^{+0.30} _{-0.22}	0.40 ^{+0.23} _{-0.21}	1.02	1.21	68
MS 2053.7-0449 *	70	561	5.16	3.66 ^{+0.81} _{-0.60}	4.07 ^{+1.23} _{-0.83}	1.11 ^{+0.42} _{-0.29}	0.39 ^{+0.38} _{-0.33}	0.97	1.07	58
MS 2137.3-2353	70	502	3.40	6.01 ^{+0.52} _{-0.46}	7.48 ^{+1.68} _{-1.09}	1.24 ^{+0.30} _{-0.20}	0.45 ^{+0.14} _{-0.14}	1.12	1.25	55
PKS 0745-191	69	651	40.80	8.13 ^{+0.37} _{-0.34}	9.68 ^{+0.83} _{-0.72}	1.19 ^{+0.12} _{-0.10}	0.38 ^{+0.06} _{-0.06}	1.02	0.98	89
RBS 0797	69	493	2.22	7.68 ^{+0.92} _{-0.77}	9.05 ^{+1.80} _{-1.33}	1.18 ^{+0.27} _{-0.21}	0.32 ^{+0.14} _{-0.13}	1.07	1.06	89
RDCS 1252-29	71	276	6.06	4.25 ^{+1.82} _{-1.14}	4.47 ^{+2.16} _{-1.29}	1.05 ^{+0.68} _{-0.41}	0.79 ^{+1.01} _{-0.62}	1.07	1.17	50
RX J0232.2-4420	69	568	2.53	7.83 ^{+0.77} _{-0.68}	9.92 ^{+2.11} _{-1.44}	1.27 ^{+0.30} _{-0.21}	0.36 ^{+0.12} _{-0.13}	1.13	1.09	85
RX J0340-4542	70	412	1.63	3.16 ^{+0.38} _{-0.35}	2.80 ^{+0.94} _{-0.57}	0.89 ^{+0.32} _{-0.21}	0.62 ^{+0.31} _{-0.25}	1.27	1.22	43
RX J0439+0520	70	474	10.02	4.60 ^{+0.64} _{-0.59}	4.95 ^{+1.28} _{-0.88}	1.08 ^{+0.32} _{-0.24}	0.44 ^{+0.29} _{-0.24}	1.03	1.14	77
RX J0439.0+0715 *	70	532	11.16	5.63 ^{+0.36} _{-0.32}	8.02 ^{+1.25} _{-0.93}	1.42 ^{+0.24} _{-0.18}	0.32 ^{+0.10} _{-0.08}	1.28	1.16	82
RX J0528.9-3927	70	640	2.36	7.89 ^{+0.59} _{-0.76}	8.91 ^{+2.30} _{-1.42}	1.13 ^{+0.32} _{-0.21}	0.27 ^{+0.14} _{-0.14}	0.92	0.93	83
RX J0647.7+7015 *	69	512	5.18	11.28 ^{+1.85} _{-1.45}	11.01 ^{+2.77} _{-1.63}	0.98 ^{+0.25} _{-0.19}	0.20 ^{+0.17} _{-0.17}	1.02	1.00	80
RX J0910+5422 *	71	246	2.07	4.53 ^{+3.02} _{-1.70}	5.98 ^{+5.30} _{-2.49}	1.32 ^{+1.46} _{-0.73}	0.00 ^{+0.73} _{-0.00}	0.90	0.71	31
RX J1347.5-1145 *	70	607	4.89	14.62 ^{+0.97} _{-0.79}	16.62 ^{+1.54} _{-1.24}	1.14 ^{+0.13} _{-0.10}	0.32 ^{+0.07} _{-0.07}	1.12	1.12	93
RX J1350+6007	71	334	1.77	4.48 ^{+2.32} _{-1.49}	5.31 ^{+3.02} _{-2.07}	1.19 ^{+0.91} _{-0.61}	0.13 ^{+1.23} _{-0.13}	0.82	0.72	57
RX J1423.8+2404 *	71	441	2.65	6.64 ^{+0.38} _{-0.34}	7.01 ^{+0.59} _{-0.51}	1.06 ^{+0.39} _{-0.07}	0.37 ^{+0.07} _{-0.07}	1.02	0.98	86
RX J1504.1-0248	70	628	6.27	8.00 ^{+0.27} _{-0.24}	8.92 ^{+0.52} _{-0.46}	1.11 ^{+0.08} _{-0.07}	0.40 ^{+0.04} _{-0.05}	1.29	1.25	91
RX J1525+0958	70	416	2.96	3.74 ^{+0.63} _{-0.45}	6.96 ^{+2.88} _{-1.73}	1.86 ^{+0.83} _{-0.51}	0.67 ^{+0.36} _{-0.29}	1.29	0.93	79
RX J1532.9+3021 *	70	458	2.21	6.03 ^{+0.42} _{-0.38}	6.95 ^{+0.88} _{-0.72}	1.15 ^{+0.17} _{-0.15}	0.42 ^{+0.11} _{-0.10}	0.94	1.05	73
RX J1716.9+6708	71	486	3.71	5.71 ^{+1.39} _{-1.06}	5.77 ^{+1.88} _{-1.28}	1.01 ^{+0.42} _{-0.29}	0.68 ^{+0.42} _{-0.35}	0.79	0.74	55
RX J1720.1+2638	69	510	4.02	6.37 ^{+0.28} _{-0.26}	7.78 ^{+0.69} _{-0.61}	1.22 ^{+0.12} _{-0.11}	0.35 ^{+0.07} _{-0.06}	1.10	1.02	90
RX J1720.2+3536 *	71	455	3.35	7.21 ^{+0.33} _{-0.46}	6.97 ^{+0.16} _{-0.59}	0.97 ^{+0.10} _{-0.10}	0.41 ^{+0.10} _{-0.10}	1.12	1.09	85
RX J2011.3-5725	71	416	4.76	3.94 ^{+0.45} _{-0.37}	4.40 ^{+1.20} _{-0.81}	1.12 ^{+0.33} _{-0.23}	0.34 ^{+0.21} _{-0.18}	0.94	1.09	76

TABLE 5 — *Continued*

Cluster	R _{CORE}	R ₂₅₀₀	N _{HI}	T ₇₇	T ₂₇	T _{HBR}	Z ₇₇	$\chi^2_{red,77}$	$\chi^2_{red,27}$	% Source
(1)	kpc (2)	kpc (3)	10 ²⁰ cm ⁻² (4)	keV (5)	keV (6)	(7)	Z _⊙ (8)	(9)	(10)	(11)
RX J2129.6+0005	70	690	4.30	5.91 ^{+0.54} _{-0.47}	7.02 ^{+1.30} _{-0.99}	1.19 ^{+0.25} _{-0.19}	0.45 ^{+0.15} _{-0.15}	1.21	1.07	80
S0463 *	70	433	1.06	3.10 ^{+0.29} _{-0.25}	3.10 ^{+0.66} _{-0.53}	1.00 ^{+0.23} _{-0.19}	0.24 ^{+0.14} _{-0.11}	1.10	1.07	47
V 1121.0+2327	70	444	1.30	3.60 ^{+0.62} _{-0.46}	4.08 ^{+1.09} _{-0.80}	1.13 ^{+0.36} _{-0.27}	0.36 ^{+0.29} _{-0.24}	1.21	1.19	66
ZWCL 1215	70	392	1.76	6.64 ^{+0.40} _{-0.35}	8.72 ^{+1.30} _{-1.07}	1.31 ^{+0.21} _{-0.18}	0.29 ^{+0.09} _{-0.09}	1.17	1.04	88
ZWCL 1358+6245	70	553	1.94	10.66 ^{+1.48} _{-1.13}	10.19 ^{+4.83} _{-3.24}	0.96 ^{+0.47} _{-0.23}	0.47 ^{+0.19} _{-0.19}	1.08	1.04	55
ZWCL 1953	69	730	3.10	7.37 ^{+1.00} _{-0.78}	10.44 ^{+3.25} _{-2.20}	1.42 ^{+0.33} _{-0.33}	0.19 ^{+0.13} _{-0.13}	0.84	0.78	74
ZWCL 3146	70	723	2.70	7.48 ^{+0.32} _{-0.30}	8.61 ^{+0.66} _{-0.58}	1.15 ^{+0.10} _{-0.09}	0.31 ^{+0.05} _{-0.06}	1.03	0.98	86
ZWCL 5247	70	635	1.70	5.06 ^{+0.85} _{-0.54}	5.91 ^{+2.09} _{-1.30}	1.17 ^{+0.46} _{-0.20}	0.22 ^{+0.21} _{-0.15}	0.83	0.72	74
ZWCL 7160	69	637	3.10	4.53 ^{+0.40} _{-0.35}	5.16 ^{+1.01} _{-0.77}	1.14 ^{+0.24} _{-0.19}	0.40 ^{+0.13} _{-0.14}	0.94	0.92	80
ZWICKY 2701	69	445	0.83	5.21 ^{+0.34} _{-0.30}	5.68 ^{+0.85} _{-0.66}	1.09 ^{+0.18} _{-0.14}	0.43 ^{+0.13} _{-0.11}	0.89	0.94	57
ZwCL 1332.8+5043	70	642	1.10	3.62 ^{+3.46} _{-1.20}	3.84 ^{+5.93} _{-1.11}	1.06 ^{+1.93} _{-0.76}	0.76 ^{+12.45} _{-0.54}	0.24	0.29	48
ZwCl 0848.5+3341	71	518	1.12	6.83 ^{+2.18} _{-1.33}	7.24 ^{+5.11} _{-2.26}	1.06 ^{+0.82} _{-0.39}	0.56 ^{+0.54} _{-0.45}	0.82	0.93	37

NOTE. — Note: “77” refers to 0.7-7.0 keV band and “27” refers to 2.0-7.0 keV band. (1) Cluster name, (2) size of excluded core region in kpc, (3) R₂₅₀₀ in kpc, (4) absorbing Galactic neutral hydrogen column density, (5,6) best-fit MEKAL temperatures, (7) T_{0.7-7.0}/T_{2.0-7.0} also called T_{HBR}, (8) best-fit 77 MEKAL abundance, (9,10) respective reduced χ^2 statistics, and (11) percent of emission attributable to source. A star (*) indicates a cluster which has multiple observations. Each observation has an independent spectrum extracted along with an associated WARF, WRMF, normalized background spectrum, and soft residual. Each independent spectrum is then fit simultaneously with the same spectral model to produce the final fit.

TABLE 6
SUMMARY OF EXCISED R₅₀₀₀ SPECTRAL FITS

Cluster	R _{CORE}	R ₅₀₀₀	N _{HI}	T ₇₇	T ₂₇	T _{HBR}	Z ₇₇	$\chi^2_{red,77}$	$\chi^2_{red,27}$	% Source
(1)	kpc (2)	kpc (3)	10 ²⁰ cm ⁻² (4)	keV (5)	keV (6)	(7)	Z _⊙ (8)	(9)	(10)	(11)
1E0657 56 *	69	487	6.53	11.81 ^{+0.29} _{-0.27}	14.13 ^{+0.58} _{-0.53}	1.20 ^{+0.06} _{-0.05}	0.29 ^{+0.03} _{-0.03}	1.22	1.10	95
1RXS J2129.4-0741 *	71	373	4.36	8.47 ^{+1.31} _{-1.04}	8.57 ^{+1.73} _{-1.27}	1.01 ^{+0.26} _{-0.19}	0.51 ^{+0.20} _{-0.19}	1.16	1.27	87
2PIGG J0011.5-2850	69	387	2.18	5.25 ^{+0.29} _{-0.27}	6.21 ^{+0.83} _{-0.68}	1.18 ^{+0.17} _{-0.14}	0.23 ^{+0.09} _{-0.08}	1.08	1.01	78
2PIGG J0311.8-2655	69	321	1.46	3.35 ^{+0.25} _{-0.22}	3.67 ^{+0.71} _{-0.54}	1.10 ^{+0.43} _{-0.18}	0.33 ^{+0.13} _{-0.11}	1.03	1.10	51
2PIGG J2227.0-3041	69	267	1.11	2.81 ^{+0.16} _{-0.16}	2.99 ^{+0.36} _{-0.28}	1.06 ^{+0.14} _{-0.11}	0.35 ^{+0.11} _{-0.08}	1.14	1.10	77
3C 220.1	71	322	1.91	7.81 ^{+7.50} _{-2.99}	7.49 ^{+11.53} _{-3.51}	0.96 ^{+0.58} _{-0.58}	0.00 ^{+0.55} _{-0.00}	0.60	0.78	36
3C 28.0	70	297	5.71	5.18 ^{+0.28} _{-0.27}	7.11 ^{+1.15} _{-0.90}	1.37 ^{+0.23} _{-0.19}	0.30 ^{+0.09} _{-0.07}	0.96	0.77	90
3C 295	69	329	1.35	5.47 ^{+0.49} _{-0.34}	5.47 ^{+0.92} _{-0.78}	1.19 ^{+0.20} _{-0.17}	0.29 ^{+0.11} _{-0.10}	1.02	1.04	87
3C 388	69	297	6.11	3.27 ^{+0.34} _{-0.21}	3.44 ^{+0.73} _{-0.51}	1.05 ^{+0.17} _{-0.17}	0.43 ^{+0.16} _{-0.13}	1.09	1.04	76
4C 55.16	69	302	4.00	4.88 ^{+0.16} _{-0.16}	5.11 ^{+0.44} _{-0.39}	1.05 ^{+0.10} _{-0.09}	0.52 ^{+0.07} _{-0.07}	0.93	0.85	71
ABELL 0013	69	404	2.03	5.39 ^{+0.28} _{-0.25}	6.41 ^{+0.84} _{-0.72}	1.19 ^{+0.17} _{-0.14}	0.37 ^{+0.09} _{-0.09}	0.96	0.95	44
ABELL 0068	70	480	4.60	9.72 ^{+1.82} _{-1.36}	10.89 ^{+5.21} _{-2.85}	1.12 ^{+0.58} _{-0.33}	0.41 ^{+0.24} _{-0.23}	1.08	1.03	87
ABELL 0119	69	399	3.30	5.86 ^{+0.28} _{-0.27}	6.20 ^{+0.74} _{-0.59}	1.06 ^{+0.14} _{-0.11}	0.44 ^{+0.10} _{-0.10}	0.98	0.89	75
ABELL 0168 *	70	281	3.27	2.56 ^{+0.13} _{-0.10}	3.37 ^{+0.48} _{-0.41}	1.32 ^{+0.20} _{-0.17}	0.32 ^{+0.07} _{-0.05}	1.03	0.97	44
ABELL 0209 *	70	430	1.68	7.32 ^{+0.65} _{-0.56}	10.05 ^{+2.33} _{-1.58}	1.37 ^{+0.34} _{-0.24}	0.21 ^{+0.11} _{-0.10}	1.07	1.15	88
ABELL 0267 *	70	385	2.74	6.46 ^{+0.51} _{-0.48}	8.46 ^{+0.52} _{-0.91}	1.31 ^{+0.13} _{-0.12}	0.37 ^{+0.12} _{-0.11}	1.18	1.29	88
ABELL 0370	69	365	3.37	8.74 ^{+0.83} _{-0.83}	10.15 ^{+2.17} _{-1.52}	1.16 ^{+0.21} _{-0.21}	0.37 ^{+0.13} _{-0.13}	1.05	1.02	50
ABELL 0383	69	300	4.07	4.95 ^{+0.30} _{-0.30}	5.92 ^{+1.05} _{-0.85}	1.20 ^{+0.22} _{-0.18}	0.43 ^{+0.12} _{-0.11}	1.12	1.10	75
ABELL 0399	69	386	8.33 ^{+0.82} _{-0.80}	7.93 ^{+0.38} _{-0.35}	8.86 ^{+0.67} _{-0.59}	1.12 ^{+0.10} _{-0.09}	0.32 ^{+0.06} _{-0.07}	1.06	0.96	87
ABELL 0401	69	454	12.48	6.54 ^{+0.20} _{-0.20}	9.37 ^{+0.91} _{-0.74}	1.43 ^{+0.15} _{-0.12}	0.29 ^{+0.07} _{-0.06}	1.53	1.10	85
ABELL 0478	69	423	30.90	7.27 ^{+0.26} _{-0.25}	8.19 ^{+0.56} _{-0.50}	1.13 ^{+0.09} _{-0.08}	0.47 ^{+0.06} _{-0.06}	1.02	0.93	95
ABELL 0514	71	365	3.14	3.57 ^{+0.24} _{-0.24}	4.30 ^{+0.84} _{-0.76}	1.20 ^{+0.25} _{-0.20}	0.25 ^{+0.11} _{-0.10}	0.99	1.01	55
ABELL 0520	70	407	1.14 ^{+1.14} _{-1.16}	9.15 ^{+0.73} _{-0.63}	10.43 ^{+1.41} _{-1.06}	1.14 ^{+0.18} _{-0.14}	0.36 ^{+0.07} _{-0.07}	1.12	1.01	91
ABELL 0521	70	394	6.17	7.31 ^{+0.79} _{-0.64}	9.01 ^{+3.73} _{-1.87}	1.23 ^{+0.53} _{-0.28}	0.48 ^{+0.17} _{-0.16}	1.11	0.95	55
ABELL 0586	70	450	4.71	6.43 ^{+0.55} _{-0.49}	8.06 ^{+1.51} _{-1.14}	1.25 ^{+0.26} _{-0.20}	0.50 ^{+0.15} _{-0.15}	0.88	0.81	87
ABELL 0611	70	370	4.99	6.79 ^{+0.51} _{-0.46}	6.88 ^{+1.23} _{-0.95}	1.01 ^{+0.20} _{-0.16}	0.32 ^{+0.10} _{-0.10}	1.04	1.07	67
ABELL 0644	70	412	6.31	7.81 ^{+0.20} _{-0.19}	8.08 ^{+0.44} _{-0.39}	1.03 ^{+0.06} _{-0.06}	0.42 ^{+0.05} _{-0.04}	1.15	1.05	92
ABELL 0665	69	436	4.24	7.35 ^{+0.40} _{-0.37}	10.43 ^{+1.76} _{-1.31}	1.42 ^{+0.25} _{-0.19}	0.29 ^{+0.07} _{-0.07}	1.07	0.94	91
ABELL 0697	69	432	3.34	9.80 ^{+0.99} _{-0.86}	13.50 ^{+2.90} _{-2.04}	1.38 ^{+0.33} _{-0.24}	0.48 ^{+0.13} _{-0.13}	1.06	0.96	93
ABELL 0773	69	434	1.46	8.09 ^{+0.75} _{-0.65}	10.52 ^{+1.92} _{-1.22}	1.30 ^{+0.27} _{-0.22}	0.37 ^{+0.12} _{-0.12}	1.03	1.04	89
ABELL 0907	69	345	5.69	5.62 ^{+0.19} _{-0.18}	6.82 ^{+0.27} _{-0.22}	1.21 ^{+0.06} _{-0.06}	0.46 ^{+0.06} _{-0.06}	1.18	1.05	92
ABELL 0963	69	384	1.39	6.97 ^{+0.35} _{-0.32}	7.65 ^{+1.00} _{-0.82}	1.10 ^{+0.15} _{-0.13}	0.29 ^{+0.08} _{-0.07}	1.13	1.12	74
ABELL 1063S	69	458	1.77	11.94 ^{+0.91} _{-0.80}	14.04 ^{+1.83} _{-1.47}	1.18 ^{+0.18} _{-0.15}	0.38 ^{+0.10} _{-0.09}	1.01	0.98	94
ABELL 1068	69	305	0.71	4.67 ^{+0.18} _{-0.18}	5.49 ^{+0.71} _{-0.58}	1.18 ^{+0.16} _{-0.13}	0.37 ^{+0.06} _{-0.07}	0.92	0.91	77
ABELL 1201	69	401	1.85	5.74 ^{+0.44} _{-0.40}	5.99 ^{+1.39} _{-0.95}	1.04 ^{+0.26} _{-0.18}	0.35 ^{+0.13} _{-0.11}	1.06	1.10	50
ABELL 1204	70	297	1.44	3.67 ^{+0.18} _{-0.16}	4.72 ^{+0.21} _{-0.17}	1.29 ^{+0.17} _{-0.17}	0.32 ^{+0.09} _{-0.09}	1.11	0.92	92
ABELL 1361	71	330	2.18	5.14 ^{+1.00} _{-0.74}	7.24 ^{+8.23} _{-2.78}	1.41 ^{+1.62} _{-0.58}	0.29 ^{+0.31} _{-0.27}	1.10	0.82	61
ABELL 1423	70	435	1.60	6.04 ^{+0.82} _{-0.68}	7.93 ^{+3.09} _{-2.20}	1.31 ^{+0.70} _{-0.39}	0.33 ^{+0.20} _{-0.17}	0.95	0.91	84
ABELL 1651	70	421	2.02	6.30 ^{+0.32} _{-0.28}	7.72 ^{+0.71} _{-0.65}	1.23 ^{+0.13} _{-0.12}	0.44 ^{+0.09} _{-0.09}	1.13	1.19	91
ABELL 1664	69	291	8.47	4.26 ^{+0.30} _{-0.26}	4.91 ^{+1.05} _{-0.80}	1.15 ^{+0.26} _{-0.20}	0.31 ^{+0.12} _{-0.11}	1.07	1.08	70

TABLE 6 — *Continued*

Cluster	R _{CORE}	R ₅₀₀₀	N _H	T ₇₇	T ₂₇	T _{HBR}	Z ₇₇	$\chi^2_{red,77}$	$\chi^2_{red,27}$	% Source
(1)	kpc (2)	kpc (3)	10 ²⁰ cm ⁻² (4)	keV (5)	keV (6)	(7)	Z _⊙ (8)	(9)	(10)	(11)
ABELL 1689 *	70	481	1.87	9.76 ^{+0.40} _{-0.38}	12.97 ^{+1.25} _{-1.05}	1.33 ^{+0.14} _{-0.12}	0.35 ^{+0.06} _{-0.05}	1.14	1.04	94
ABELL 1758	69	404	1.09	9.66 ^{+0.75} _{-0.64}	9.90 ^{+1.22} _{-1.86}	1.02 ^{+0.15} _{-0.21}	0.48 ^{+0.11} _{-0.11}	1.03	0.96	68
ABELL 1763	69	396	0.82	7.74 ^{+0.73} _{-0.64}	12.56 ^{+3.12} _{-3.12}	1.62 ^{+0.83} _{-0.42}	0.22 ^{+0.19} _{-0.12}	1.16	1.02	89
ABELL 1795	69	449	1.22	6.05 ^{+0.15} _{-0.15}	6.85 ^{+0.42} _{-0.38}	1.13 ^{+0.07} _{-0.07}	0.33 ^{+0.04} _{-0.05}	1.19	1.03	93
ABELL 1835	70	404	2.36	9.55 ^{+0.55} _{-0.51}	11.99 ^{+1.96} _{-1.90}	1.26 ^{+0.22} _{-0.17}	0.35 ^{+0.07} _{-0.08}	0.91	0.88	91
ABELL 1914	70	493	0.97	9.73 ^{+0.58} _{-0.51}	11.97 ^{+1.90} _{-1.40}	1.23 ^{+0.21} _{-0.16}	0.32 ^{+0.08} _{-0.07}	1.11	1.03	95
ABELL 1942	69	334	2.75	4.96 ^{+0.45} _{-0.39}	5.94 ^{+2.24} _{-0.99}	1.20 ^{+0.46} _{-0.22}	0.37 ^{+0.15} _{-0.14}	1.04	0.87	77
ABELL 1995	71	271	1.44	8.50 ^{+0.83} _{-0.71}	9.41 ^{+1.87} _{-1.32}	1.11 ^{+0.25} _{-0.13}	0.33 ^{+0.12} _{-0.12}	1.05	1.02	81
ABELL 2029	70	434	3.26	8.22 ^{+0.31} _{-0.30}	9.92 ^{+0.91} _{-0.73}	1.21 ^{+0.18} _{-0.10}	0.40 ^{+0.06} _{-0.06}	1.08	1.04	94
ABELL 2034	69	420	1.58	7.35 ^{+0.26} _{-0.24}	9.96 ^{+1.09} _{-0.84}	1.36 ^{+0.16} _{-0.12}	0.34 ^{+0.05} _{-0.05}	1.17	1.02	90
ABELL 2065	69	370	2.96	5.75 ^{+0.19} _{-0.17}	6.39 ^{+0.46} _{-0.41}	1.11 ^{+0.09} _{-0.08}	0.28 ^{+0.05} _{-0.05}	1.11	1.01	89
ABELL 2069	70	440	1.97	6.33 ^{+0.36} _{-0.32}	8.29 ^{+1.36} _{-1.02}	1.31 ^{+0.23} _{-0.17}	0.24 ^{+0.08} _{-0.08}	1.14	1.15	78
ABELL 2111	70	417	2.20	5.74 ^{+1.43} _{-0.97}	7.18 ^{+6.73} _{-2.52}	1.25 ^{+1.21} _{-0.49}	0.16 ^{+0.30} _{-0.16}	1.06	0.97	74
ABELL 2125	70	262	2.75	3.09 ^{+0.37} _{-0.31}	3.69 ^{+1.99} _{-0.81}	1.19 ^{+0.66} _{-0.29}	0.36 ^{+0.25} _{-0.20}	1.25	1.22	68
ABELL 2163	69	531	12.04	18.78 ^{+0.89} _{-0.83}	19.49 ^{+2.03} _{-1.86}	1.04 ^{+0.12} _{-0.11}	0.09 ^{+0.06} _{-0.05}	1.33	1.25	93
ABELL 2204 *	70	406	5.84	9.35 ^{+0.43} _{-0.41}	10.18 ^{+0.95} _{-0.77}	1.09 ^{+0.11} _{-0.10}	0.37 ^{+0.07} _{-0.07}	0.95	0.97	86
ABELL 2218	70	394	3.12	7.37 ^{+0.40} _{-0.37}	9.36 ^{+1.42} _{-1.07}	1.27 ^{+0.20} _{-0.16}	0.22 ^{+0.07} _{-0.06}	1.00	0.91	91
ABELL 2219	69	463	1.76	12.60 ^{+0.65} _{-0.61}	12.54 ^{+1.52} _{-1.21}	1.00 ^{+0.13} _{-0.11}	0.31 ^{+0.07} _{-0.07}	1.02	0.98	81
ABELL 2255	71	422	2.53	6.37 ^{+0.24} _{-0.23}	7.70 ^{+0.79} _{-0.49}	1.21 ^{+0.13} _{-0.09}	0.34 ^{+0.06} _{-0.06}	0.93	0.84	81
ABELL 2256	70	441	4.05	5.66 ^{+0.19} _{-0.17}	7.30 ^{+0.69} _{-0.63}	1.29 ^{+0.13} _{-0.12}	0.31 ^{+0.07} _{-0.07}	1.61	1.44	79
ABELL 2259	69	340	3.70	5.07 ^{+0.46} _{-0.40}	5.49 ^{+1.29} _{-0.91}	1.08 ^{+0.27} _{-0.20}	0.40 ^{+0.16} _{-0.14}	0.92	0.92	90
ABELL 2261	69	407	3.31	7.86 ^{+0.51} _{-0.47}	9.84 ^{+1.94} _{-1.30}	1.25 ^{+0.26} _{-0.18}	0.40 ^{+0.09} _{-0.09}	0.98	0.95	94
ABELL 2294	69	405	6.10	10.49 ^{+1.75} _{-1.30}	12.33 ^{+5.72} _{-3.05}	1.18 ^{+0.58} _{-0.33}	0.57 ^{+0.25} _{-0.24}	1.16	1.08	88
ABELL 2384	70	308	2.99	4.53 ^{+0.22} _{-0.21}	6.78 ^{+1.13} _{-0.89}	1.50 ^{+0.26} _{-0.21}	0.15 ^{+0.07} _{-0.06}	0.99	0.88	86
ABELL 2390	70	447	6.71	10.85 ^{+0.34} _{-0.31}	10.53 ^{+0.62} _{-0.53}	0.97 ^{+0.06} _{-0.06}	0.35 ^{+0.08} _{-0.04}	1.15	1.03	81
ABELL 2409	70	362	6.72	5.93 ^{+0.45} _{-0.39}	5.87 ^{+0.95} _{-0.76}	0.99 ^{+0.18} _{-0.14}	0.35 ^{+0.13} _{-0.11}	1.05	0.76	92
ABELL 2537	69	351	4.26	8.83 ^{+0.87} _{-0.74}	7.83 ^{+1.54} _{-1.15}	0.89 ^{+0.20} _{-0.15}	0.39 ^{+0.14} _{-0.13}	0.93	0.83	59
ABELL 2554	71	415	2.04	5.35 ^{+0.45} _{-0.40}	6.46 ^{+1.93} _{-1.24}	1.21 ^{+0.37} _{-0.25}	0.35 ^{+0.15} _{-0.13}	0.93	0.79	40
ABELL 2556	70	323	2.02	3.57 ^{+0.16} _{-0.15}	4.07 ^{+0.56} _{-0.46}	1.14 ^{+0.16} _{-0.14}	0.36 ^{+0.07} _{-0.07}	0.99	0.95	58
ABELL 2631	70	445	3.74	7.18 ^{+1.18} _{-0.94}	9.18 ^{+3.17} _{-1.96}	1.28 ^{+0.49} _{-0.32}	0.34 ^{+0.20} _{-0.12}	1.03	0.99	89
ABELL 2667	70	370	1.64	6.68 ^{+0.48} _{-0.43}	7.35 ^{+1.27} _{-1.05}	1.10 ^{+0.21} _{-0.17}	0.41 ^{+0.12} _{-0.12}	1.05	0.95	84
ABELL 2670	69	319	2.88	3.96 ^{+0.13} _{-0.13}	4.75 ^{+0.50} _{-0.43}	1.20 ^{+0.13} _{-0.11}	0.45 ^{+0.08} _{-0.07}	1.16	1.09	80
ABELL 2717	70	211	1.12	2.59 ^{+0.17} _{-0.16}	3.18 ^{+0.43} _{-0.44}	1.23 ^{+0.24} _{-0.19}	0.53 ^{+0.14} _{-0.12}	0.90	0.95	67
ABELL 2744	71	458	1.82	9.82 ^{+0.89} _{-0.77}	11.21 ^{+2.76} _{-1.81}	1.14 ^{+0.30} _{-0.20}	0.30 ^{+0.12} _{-0.12}	0.88	0.73	74
ABELL 3128	70	318	1.59	3.04 ^{+0.23} _{-0.21}	3.48 ^{+0.73} _{-0.54}	1.14 ^{+0.26} _{-0.19}	0.33 ^{+0.13} _{-0.10}	1.05	1.13	64
ABELL 3158 *	70	382	1.60	5.08 ^{+0.08} _{-0.08}	6.26 ^{+0.26} _{-0.24}	1.23 ^{+0.05} _{-0.05}	0.40 ^{+0.03} _{-0.03}	1.15	0.97	89
ABELL 3164	70	319	2.55	2.40 ^{+0.65} _{-0.48}	3.19 ^{+3.68} _{-1.41}	1.33 ^{+2.39} _{-0.64}	0.23 ^{+0.32} _{-0.19}	1.29	1.59	30
ABELL 3376 *	70	327	5.21	4.44 ^{+0.14} _{-0.13}	5.94 ^{+0.55} _{-0.47}	1.34 ^{+0.13} _{-0.13}	0.36 ^{+0.06} _{-0.08}	1.18	1.13	65
ABELL 3391	70	397	5.46	5.72 ^{+0.31} _{-0.28}	6.44 ^{+0.80} _{-0.66}	1.13 ^{+0.13} _{-0.13}	0.11 ^{+0.08} _{-0.07}	1.00	0.97	67
ABELL 3921	69	378	3.07	5.69 ^{+0.25} _{-0.24}	6.74 ^{+0.71} _{-0.58}	1.18 ^{+0.14} _{-0.11}	0.34 ^{+0.08} _{-0.07}	0.93	0.85	84
AC 114	70	389	1.44	7.75 ^{+0.56} _{-0.50}	9.76 ^{+2.28} _{-1.55}	1.26 ^{+0.31} _{-0.22}	0.36 ^{+0.10} _{-0.10}	1.01	0.95	63
CL 0024+17	71	309	4.36	4.75 ^{+1.07} _{-0.76}	7.14 ^{+3.42} _{-2.83}	1.50 ^{+1.19} _{-0.64}	0.58 ^{+0.35} _{-0.30}	1.07	0.97	44
CL 1221+4918	71	313	1.44	6.73 ^{+1.29} _{-1.03}	7.60 ^{+4.33} _{-2.01}	1.13 ^{+0.68} _{-0.34}	0.32 ^{+0.20} _{-0.19}	0.92	0.69	73
CL J0030+2618	70	555	4.10	4.48 ^{+1.43} _{-1.40}	3.77 ^{+2.22} _{-1.96}	0.84 ^{+0.51} _{-0.51}	0.00 ^{+0.00} _{-0.00}	1.01	0.85	51
CL J0152-1357	70	277	1.45	7.20 ^{+1.74} _{-1.45}	6.07 ^{+6.16} _{-2.51}	0.84 ^{+1.20} _{-0.45}	0.00 ^{+0.63} _{-0.00}	2.97	3.26	49
CL J0542.8-4100	71	313	3.59	5.63 ^{+1.21} _{-0.90}	5.93 ^{+3.52} _{-1.76}	1.05 ^{+0.66} _{-0.35}	0.25 ^{+0.24} _{-0.22}	0.67	0.58	72
CL J0848+4456 *	71	224	2.53	3.73 ^{+1.47} _{-0.85}	4.96 ^{+2.82} _{-1.81}	1.33 ^{+0.92} _{-0.57}	0.17 ^{+0.98} _{-0.17}	0.87	0.82	64
CL J1113.1-2615	70	308	5.51	4.74 ^{+1.52} _{-0.98}	4.79 ^{+1.15} _{-1.26}	1.01 ^{+0.40} _{-0.34}	0.53 ^{+0.52} _{-0.37}	1.02	1.01	32
CL J1226.9+3332 *	69	318	1.37	13.02 ^{+2.69} _{-2.00}	12.33 ^{+2.78} _{-2.13}	0.95 ^{+0.29} _{-0.22}	0.18 ^{+0.23} _{-0.18}	0.75	0.80	91
CL J2302.8+0844	70	362	5.05	5.94 ^{+1.73} _{-1.66}	6.58 ^{+8.08} _{-2.67}	1.11 ^{+1.40} _{-0.57}	0.10 ^{+0.29} _{-0.10}	0.94	1.01	56
DLS J0514-4904	70	359	2.52	4.94 ^{+0.61} _{-0.55}	6.26 ^{+2.33} _{-1.30}	1.27 ^{+0.50} _{-0.30}	0.35 ^{+0.27} _{-0.23}	0.86	1.03	63
EXO 0422-086	70	294	6.22	3.41 ^{+0.13} _{-0.13}	3.44 ^{+0.37} _{-0.31}	1.01 ^{+0.12} _{-0.10}	0.37 ^{+0.08} _{-0.08}	0.96	0.93	80
HERCULES A	69	312	1.49 ^{+2.01} _{-1.49}	5.28 ^{+0.60} _{-0.50}	4.50 ^{+0.88} _{-0.65}	0.85 ^{+0.19} _{-0.15}	0.42 ^{+0.15} _{-0.14}	0.98	0.98	70
MACS J0011.7-1523 *	69	319	2.08	6.73 ^{+0.55} _{-0.47}	7.27 ^{+0.99} _{-0.74}	1.08 ^{+0.17} _{-0.13}	0.27 ^{+0.10} _{-0.09}	0.90	0.95	92
MACS J0025.4-1222 *	70	335	2.72	6.65 ^{+1.07} _{-0.85}	6.31 ^{+1.38} _{-1.02}	0.95 ^{+0.26} _{-0.20}	0.39 ^{+0.22} _{-0.19}	0.66	0.75	86
MACS J0035.4-2015	70	372	1.55	7.72 ^{+0.88} _{-0.74}	9.39 ^{+1.91} _{-1.35}	1.22 ^{+0.28} _{-0.21}	0.39 ^{+0.14} _{-0.13}	1.02	1.05	94
MACS J0111.5+0855	70	306	4.18	4.12 ^{+1.60} _{-1.03}	4.16 ^{+2.96} _{-1.44}	1.01 ^{+0.43} _{-0.31}	0.00 ^{+0.43} _{-0.00}	0.79	1.23	62
MACS J0152.5-2852	70	324	1.46	5.75 ^{+1.03} _{-0.78}	7.70 ^{+3.21} _{-1.89}	1.34 ^{+0.61} _{-0.38}	0.28 ^{+0.92} _{-0.21}	0.84	0.58	90
MACS J0159.0-3412	70	404	1.54	10.99 ^{+5.87} _{-2.95}	12.74 ^{+12.45} _{-4.77}	1.16 ^{+1.29} _{-0.53}	0.50 ^{+0.52} _{-0.50}	1.35	1.34	85
MACS J0159.8-0849 *	69	413	2.01	9.36 ^{+0.77} _{-0.67}	10.37 ^{+1.29} _{-1.04}	1.11 ^{+0.17} _{-0.14}	0.29 ^{+0.09} _{-0.09}	1.05	1.01	94
MACS J0242.5-2132	70	352	2.71	5.48 ^{+0.62} _{-0.51}	5.99 ^{+2.04} _{-1.19}	1.09 ^{+0.39} _{-0.24}	0.32 ^{+0.16} _{-0.15}	1.08	1.06	92
MACS J0257.1-2325 *	70	409	2.09	9.42 ^{+1.37} _{-1.05}	10.76 ^{+2.05} _{-1.69}	1.14 ^{+0.27} _{-0.22}	0.14 ^{+0.13} _{-0.13}	1.03	1.13	90
MACS J0257.6-2209	69	382	2.02	8.09 ^{+1.04} _{-0.88}	7.90 ^{+1.64} _{-1.20}	0.98 ^{+0.23} _{-0.18}	0.41 ^{+0.18} _{-0.18}	1.13	1.24	90
MACS J0308.9+2645	69	381	11.88	10.64 ^{+1.38} _{-1.14}	11.12 ^{+2.23} _{-1.68}	1.05 ^{+0.25} _{-0.19}	0.37 ^{+0.15} _{-0.15}	0.96	0.97	92

TABLE 6 — *Continued*

Cluster	R _{CORE}	R ₅₀₀₀	N _H	T ₇₇	T ₂₇	T _{HBR}	Z ₇₇	$\chi^2_{red,77}$	$\chi^2_{red,27}$	% Source
(1)	kpc (2)	kpc (3)	10 ²⁰ cm ⁻² (4)	keV (5)	keV (6)	(7)	Z _⊙ (8)	(9)	(10)	(11)
MACS J0329.6-0211 *	70	297	6.21	6.44 ^{+0.50} _{-0.45}	7.55 ^{+0.88} _{-0.73}	1.17 ^{+0.16} _{-0.14}	0.40 ^{+0.10} _{-0.09}	1.12	1.16	91
MACS J0404.6+1109	70	348	14.96	6.90 ^{+0.41} _{-0.29}	7.40 ^{+3.63} _{-1.93}	1.07 ^{+0.61} _{-0.34}	0.22 ^{+0.27} _{-0.23}	0.96	0.92	80
MACS J0417.5-1154	70	304	4.00	10.44 ^{+2.08} _{-1.56}	14.46 ^{+5.92} _{-3.41}	1.39 ^{+0.63} _{-0.39}	0.41 ^{+0.21} _{-0.21}	1.10	1.17	96
MACS J0429.6-0253	69	348	5.70	5.96 ^{+0.72} _{-0.60}	7.48 ^{+2.65} _{-1.64}	1.26 ^{+0.47} _{-0.30}	0.34 ^{+0.15} _{-0.14}	1.02	0.78	89
MACS J0451.9+0006	70	325	7.65	5.76 ^{+1.77} _{-1.11}	6.68 ^{+4.50} _{-2.44}	1.16 ^{+0.86} _{-0.40}	0.47 ^{+0.46} _{-0.38}	1.03	1.33	89
MACS J0455.2+0657	71	340	10.45	6.99 ^{+2.27} _{-1.44}	8.35 ^{+3.66} _{-2.49}	1.19 ^{+0.66} _{-0.43}	0.48 ^{+0.31} _{-0.31}	1.04	1.24	88
MACS J0520.7-1328	69	348	8.88	6.77 ^{+1.01} _{-0.79}	9.41 ^{+3.38} _{-1.91}	1.39 ^{+0.54} _{-0.33}	0.33 ^{+0.16} _{-0.16}	1.22	1.33	91
MACS J0547.0-3904	69	257	4.08	3.70 ^{+0.44} _{-0.37}	5.82 ^{+2.97} _{-1.60}	1.57 ^{+0.82} _{-0.40}	0.24 ^{+0.21} _{-0.17}	1.14	1.21	83
MACS J0553.4-3342	70	490	2.88	13.90 ^{+3.89} _{-3.28}	14.59 ^{+11.6} _{-4.72}	1.05 ^{+0.92} _{-0.42}	0.38 ^{+0.39} _{-0.38}	1.22	1.10	91
MACS J0717.5+3745 *	70	398	6.75	13.30 ^{+1.44} _{-1.21}	12.82 ^{+1.70} _{-1.39}	0.96 ^{+0.17} _{-0.14}	0.32 ^{+0.12} _{-0.13}	0.91	0.87	91
MACS J0744.8+3927 *	70	381	4.66	8.58 ^{+0.85} _{-0.73}	9.32 ^{+1.20} _{-0.96}	1.09 ^{+0.18} _{-0.15}	0.30 ^{+0.11} _{-0.11}	1.14	1.19	89
MACS J0911.2+1746 *	70	382	3.55	7.71 ^{+1.53} _{-1.16}	7.88 ^{+2.11} _{-1.44}	1.02 ^{+0.34} _{-0.24}	0.22 ^{+0.20} _{-0.20}	0.77	0.77	85
MACS J0949+1708	70	411	3.17	8.94 ^{+1.57} _{-1.20}	10.29 ^{+5.60} _{-2.41}	1.15 ^{+0.66} _{-0.31}	0.48 ^{+0.23} _{-0.23}	0.74	0.58	93
MACS J1006.9+3200	70	363	1.83	7.03 ^{+2.66} _{-1.64}	6.53 ^{+4.61} _{-2.11}	0.93 ^{+0.74} _{-0.37}	0.18 ^{+0.18} _{-0.18}	1.64	1.53	81
MACS J1105.7-1014	71	356	4.58	7.73 ^{+2.83} _{-1.73}	6.61 ^{+3.02} _{-1.79}	0.86 ^{+0.50} _{-0.30}	0.20 ^{+0.32} _{-0.20}	1.27	1.08	87
MACS J1108.8+0906 *	70	345	2.52	6.80 ^{+1.21} _{-0.93}	7.52 ^{+2.39} _{-1.27}	1.11 ^{+0.40} _{-0.27}	0.24 ^{+0.20} _{-0.19}	1.08	1.01	86
MACS J1115.2+5320 *	70	372	0.98	9.58 ^{+0.85} _{-1.37}	9.80 ^{+2.74} _{-1.81}	1.02 ^{+0.35} _{-0.24}	0.37 ^{+0.22} _{-0.21}	0.94	0.91	82
MACS J1115.8+0129	70	316	4.36	6.82 ^{+1.15} _{-0.88}	9.39 ^{+4.77} _{-2.84}	1.38 ^{+0.74} _{-0.45}	0.07 ^{+0.19} _{-0.07}	0.94	0.85	77
MACS J1131.8-1955	69	407	4.49	8.64 ^{+1.32} _{-0.93}	9.45 ^{+2.32} _{-1.32}	1.09 ^{+0.34} _{-0.23}	0.49 ^{+0.19} _{-0.12}	1.07	1.02	91
MACS J1149.5+2223 *	69	358	2.32	7.72 ^{+0.93} _{-0.79}	8.36 ^{+1.91} _{-1.14}	1.08 ^{+0.24} _{-0.18}	0.25 ^{+0.12} _{-0.13}	0.87	0.94	75
MACS J1206.2-0847	70	367	4.15	9.98 ^{+1.27} _{-1.01}	11.93 ^{+2.56} _{-1.88}	1.20 ^{+0.30} _{-0.22}	0.32 ^{+0.13} _{-0.14}	1.02	1.15	95
MACS J1226.8+2153	71	347	1.82	4.86 ^{+1.58} _{-1.08}	5.84 ^{+3.45} _{-2.14}	1.20 ^{+0.81} _{-0.51}	0.00 ^{+0.00} _{-0.00}	1.32	1.36	78
MACS J1311.0-0310 *	69	301	2.18	5.73 ^{+0.46} _{-0.40}	5.92 ^{+0.70} _{-0.60}	1.03 ^{+0.15} _{-0.13}	0.44 ^{+0.12} _{-0.12}	0.93	1.00	83
MACS J1319+7003	70	351	1.53	8.08 ^{+2.14} _{-1.49}	10.12 ^{+5.50} _{-2.78}	1.25 ^{+0.76} _{-0.42}	0.10 ^{+0.25} _{-0.10}	1.00	1.07	82
MACS J1427.2+4407	71	346	1.41	8.61 ^{+2.23} _{-1.54}	8.83 ^{+5.55} _{-2.81}	1.03 ^{+0.80} _{-0.42}	0.14 ^{+0.14} _{-0.14}	0.68	0.58	90
MACS J1427.6-2521	71	302	6.11	4.44 ^{+0.86} _{-0.64}	6.17 ^{+3.18} _{-1.71}	1.39 ^{+0.77} _{-0.43}	0.21 ^{+0.26} _{-0.21}	1.07	1.39	79
MACS J1621.3+3810 *	69	358	1.07	7.49 ^{+0.73} _{-0.63}	7.75 ^{+1.12} _{-0.89}	1.03 ^{+0.18} _{-0.15}	0.35 ^{+0.13} _{-0.13}	0.98	0.92	82
MACS J1731.6+2252	71	368	6.48	8.19 ^{+1.88} _{-1.31}	10.50 ^{+4.76} _{-2.46}	1.28 ^{+0.63} _{-0.36}	0.49 ^{+0.27} _{-0.25}	1.16	0.98	87
MACS J1931.8-2634	70	378	9.13	6.85 ^{+0.73} _{-0.61}	6.86 ^{+1.58} _{-1.15}	1.00 ^{+0.25} _{-0.19}	0.23 ^{+0.12} _{-0.11}	1.02	1.07	94
MACS J2046.0-3430	71	274	4.98	5.02 ^{+1.95} _{-1.04}	6.23 ^{+2.37} _{-1.30}	1.24 ^{+0.70} _{-0.53}	0.23 ^{+0.55} _{-0.23}	1.10	1.14	89
MACS J2049.9-3217	69	370	5.99	7.88 ^{+1.22} _{-0.98}	11.48 ^{+4.02} _{-2.42}	1.46 ^{+0.56} _{-0.36}	0.37 ^{+0.18} _{-0.16}	0.94	0.90	89
MACS J2211.7-0349	69	468	5.86	11.13 ^{+1.45} _{-1.15}	13.77 ^{+3.49} _{-2.40}	1.24 ^{+0.35} _{-0.27}	0.18 ^{+0.14} _{-0.14}	1.33	1.34	93
MACS J2214.9-1359 *	70	374	3.32	9.87 ^{+1.15} _{-1.17}	9.97 ^{+2.17} _{-1.50}	1.01 ^{+0.19} _{-0.19}	0.31 ^{+0.17} _{-0.17}	1.03	1.01	92
MACS J2228+2036	70	385	4.52	7.79 ^{+1.14} _{-0.90}	10.04 ^{+3.96} _{-2.25}	1.29 ^{+0.54} _{-0.32}	0.41 ^{+0.18} _{-0.17}	0.84	0.96	92
MACS J2229.7-2755	69	327	1.34	5.25 ^{+0.54} _{-0.45}	6.07 ^{+1.76} _{-1.15}	1.16 ^{+0.36} _{-0.25}	0.59 ^{+0.20} _{-0.17}	0.98	1.02	91
MACS J2243.3-0935	71	406	4.31	5.15 ^{+0.65} _{-0.54}	8.81 ^{+4.18} _{-2.67}	1.71 ^{+0.86} _{-0.55}	0.05 ^{+0.17} _{-0.05}	1.38	1.27	66
MACS J2245.0+2637	69	320	5.50	6.05 ^{+0.66} _{-0.56}	7.05 ^{+1.31} _{-1.08}	1.17 ^{+0.25} _{-0.21}	0.64 ^{+0.21} _{-0.20}	0.78	0.95	92
MACS J2311+0338	70	257	5.23	7.66 ^{+1.65} _{-1.20}	12.19 ^{+6.04} _{-3.14}	1.59 ^{+0.86} _{-0.48}	0.44 ^{+0.24} _{-0.21}	1.22	1.10	92
MKW3S	70	239	3.05	3.93 ^{+0.06} _{-0.06}	4.58 ^{+0.19} _{-0.17}	1.17 ^{+0.03} _{-0.05}	0.35 ^{+0.02} _{-0.03}	1.28	0.93	88
MS 0016.9+1609	69	389	4.06	9.11 ^{+0.96} _{-0.79}	11.73 ^{+2.98} _{-1.84}	1.29 ^{+0.35} _{-0.25}	0.32 ^{+0.10} _{-0.09}	0.91	0.92	88
MS 0440.5+0204	71	497	9.10	5.99 ^{+0.68} _{-0.59}	4.45 ^{+1.61} _{-1.37}	0.74 ^{+0.32} _{-0.25}	0.66 ^{+0.29} _{-0.29}	0.89	0.74	28
MS 0451.6-0305	70	378	5.68	9.25 ^{+0.89} _{-0.77}	11.55 ^{+2.88} _{-1.91}	1.25 ^{+0.33} _{-0.23}	0.42 ^{+0.12} _{-0.11}	0.95	0.94	71
MS 0735.6+7421	69	348	3.40	5.54 ^{+0.24} _{-0.23}	6.47 ^{+0.75} _{-0.62}	1.17 ^{+0.14} _{-0.13}	0.35 ^{+0.07} _{-0.07}	1.09	1.08	74
MS 0839.8+2938	70	294	3.92	4.63 ^{+0.30} _{-0.28}	4.64 ^{+0.93} _{-0.71}	1.00 ^{+0.16} _{-0.16}	0.49 ^{+0.13} _{-0.13}	0.97	0.91	69
MS 0906.5+1110	70	435	3.60	5.56 ^{+0.34} _{-0.31}	6.94 ^{+1.23} _{-0.92}	1.25 ^{+0.23} _{-0.18}	0.34 ^{+0.10} _{-0.10}	1.20	0.97	82
MS 1006.0+1202	70	393	3.63	5.79 ^{+0.34} _{-0.46}	7.76 ^{+2.25} _{-1.56}	1.34 ^{+0.41} _{-0.29}	0.28 ^{+0.12} _{-0.12}	1.22	1.24	82
MS 1008.1-1224	70	389	6.71	5.76 ^{+0.56} _{-0.47}	9.88 ^{+2.34} _{-1.70}	1.72 ^{+0.47} _{-0.33}	0.24 ^{+0.11} _{-0.11}	1.29	1.08	83
MS 1054.5-0321	70	395	3.69	9.75 ^{+1.69} _{-1.28}	14.17 ^{+12.06} _{-4.93}	1.45 ^{+1.26} _{-0.54}	0.16 ^{+0.16} _{-0.16}	1.05	0.85	51
MS 1455.0+2232	69	309	3.35	4.82 ^{+0.14} _{-0.13}	5.47 ^{+0.29} _{-0.27}	1.13 ^{+0.07} _{-0.06}	0.46 ^{+0.05} _{-0.05}	1.34	1.17	94
MS 1621.5+2640	70	379	3.59	5.72 ^{+0.90} _{-0.72}	5.10 ^{+2.04} _{-1.27}	0.89 ^{+0.38} _{-0.25}	0.37 ^{+0.23} _{-0.21}	1.00	0.98	74
MS 2053.7-0449 *	70	397	5.16	4.68 ^{+1.04} _{-0.75}	5.37 ^{+1.73} _{-1.19}	1.15 ^{+0.45} _{-0.31}	0.26 ^{+0.26} _{-0.24}	0.99	0.94	65
MS 2137.3-2353	70	354	3.40	6.00 ^{+0.33} _{-0.47}	7.56 ^{+2.49} _{-1.46}	1.26 ^{+0.48} _{-0.26}	0.35 ^{+0.13} _{-0.12}	1.08	1.28	69
MS J1157.3+5531	69	272	1.22	3.28 ^{+0.36} _{-0.32}	6.57 ^{+6.42} _{-3.33}	2.00 ^{+1.97} _{-1.03}	0.76 ^{+0.30} _{-0.19}	1.22	1.15	37
NGC 6338	71	265	2.60	2.20 ^{+0.07} _{-0.06}	2.68 ^{+0.24} _{-0.20}	1.22 ^{+0.12} _{-0.10}	0.22 ^{+0.03} _{-0.04}	1.04	1.01	51
PKS 0745-191	69	460	40.80	8.30 ^{+0.93} _{-0.36}	9.69 ^{+0.84} _{-0.73}	1.17 ^{+0.10} _{-0.10}	0.42 ^{+0.07} _{-0.07}	1.01	0.97	93
RBS 0797	69	350	2.22	7.63 ^{+0.94} _{-0.77}	8.62 ^{+2.60} _{-1.69}	1.13 ^{+0.37} _{-0.25}	0.25 ^{+0.13} _{-0.13}	1.06	0.83	93
RDCS 1252-29	71	196	6.06	4.63 ^{+2.39} _{-1.41}	4.94 ^{+9.84} _{-2.82}	1.07 ^{+2.20} _{-0.69}	1.14 ^{+2.11} _{-0.83}	1.36	0.28	60
RX J0232.2-4420	69	402	2.53	7.92 ^{+0.85} _{-0.74}	10.54 ^{+2.53} _{-1.74}	1.33 ^{+0.35} _{-0.25}	0.38 ^{+0.13} _{-0.13}	1.05	0.98	91
RX J0340-4542	70	291	1.63	3.10 ^{+0.43} _{-0.38}	2.75 ^{+1.15} _{-0.67}	0.89 ^{+0.39} _{-0.24}	0.63 ^{+0.39} _{-0.28}	1.22	1.30	48
RX J0439+0520	70	336	10.02	4.67 ^{+0.38} _{-0.47}	5.37 ^{+2.03} _{-1.24}	1.15 ^{+0.46} _{-0.29}	0.36 ^{+0.22} _{-0.20}	0.91	0.81	85
RX J0439.0+0715 *	70	376	11.16	5.65 ^{+0.38} _{-0.34}	8.21 ^{+1.29} _{-0.96}	1.45 ^{+0.25} _{-0.19}	0.34 ^{+0.09} _{-0.09}	1.32	1.14	87
RX J0528.9-3927	70	454	2.36	7.96 ^{+1.01} _{-0.81}	9.84 ^{+2.92} _{-1.81}	1.24 ^{+0.40} _{-0.28}	0.26 ^{+0.14} _{-0.13}	0.96	1.04	88
RX J0647.7+7015 *	69	361	5.18	11.46 ^{+2.05} _{-1.58}	11.18 ^{+2.46} _{-1.77}	0.98 ^{+0.28} _{-0.20}	0.24 ^{+0.13} _{-0.13}	1.00	0.92	88
RX J0819.6+6336	71	322	4.11	3.92 ^{+0.46} _{-0.40}	3.24 ^{+1.26} _{-0.66}	0.83 ^{+0.34} _{-0.19}	0.16 ^{+0.17} _{-0.14}	1.00	1.00	50

TABLE 6 — *Continued*

Cluster	R _{CORE}	R ₅₀₀₀	N _H I	T ₇₇	T ₂₇	T _{HBR}	Z ₇₇	$\chi^2_{red,77}$	$\chi^2_{red,27}$	% Source
(1)	kpc (2)	kpc (3)	10 ²⁰ cm ⁻² (4)	keV (5)	keV (6)	(7)	Z _⊙ (8)	(9)	(10)	(11)
RX J0910+5422 *	71	172	2.07	4.08 ^{+3.11} _{-1.34}	5.00 ^{+5.09} _{-2.03}	1.23 ^{+1.56} _{-0.64}	0.43 ^{+1.89} _{-0.43}	0.64	0.56	42
RX J1347.5-1145 *	70	429	4.89	15.12 ^{+1.03} _{-0.86}	17.32 ^{+1.73} _{-1.40}	1.15 ^{+0.14} _{-0.11}	0.33 ^{+0.07} _{-0.08}	1.12	1.11	96
RX J1350+6007	71	236	1.77	4.22 ^{+3.13} _{-1.53}	3.29 ^{+10.32} _{-1.93}	0.78 ^{+2.36} _{-0.54}	0.63 ^{+3.75} _{-0.63}	1.00	0.14	66
RX J1423.8+2404 *	71	314	2.65	6.90 ^{+0.39} _{-0.37}	7.19 ^{+0.59} _{-0.52}	1.04 ^{+0.10} _{-0.09}	0.38 ^{+0.07} _{-0.08}	0.94	0.90	90
RX J1504.1-0248	70	445	6.27	8.02 ^{+0.26} _{-0.25}	8.52 ^{+0.38} _{-0.30}	1.06 ^{+0.08} _{-0.07}	0.39 ^{+0.04} _{-0.05}	1.25	1.17	95
RX J1525+0958	70	296	2.96	3.83 ^{+0.84} _{-0.53}	9.10 ^{+9.82} _{-3.25}	2.38 ^{+2.06} _{-0.91}	0.69 ^{+0.47} _{-0.36}	1.96	0.08	83
RX J1532.9+3021 *	70	322	2.21	6.06 ^{+0.43} _{-0.39}	7.20 ^{+0.94} _{-0.77}	1.19 ^{+0.18} _{-0.15}	0.46 ^{+0.10} _{-0.11}	0.92	1.02	83
RX J1716.9+6708	71	342	3.71	6.51 ^{+1.79} _{-1.24}	6.21 ^{+4.03} _{-2.26}	0.95 ^{+0.67} _{-0.39}	0.56 ^{+0.39} _{-0.32}	0.84	0.92	63
RX J1720.1+2638	69	359	4.02	6.33 ^{+0.29} _{-0.25}	7.71 ^{+0.84} _{-0.65}	1.22 ^{+0.14} _{-0.11}	0.37 ^{+0.07} _{-0.07}	1.04	0.96	94
RX J1720.2+3536 *	71	320	3.35	7.34 ^{+0.59} _{-0.50}	7.40 ^{+0.86} _{-0.71}	1.01 ^{+0.14} _{-0.12}	0.43 ^{+0.11} _{-0.11}	1.03	0.94	91
RX J2011.3-5725	71	295	4.76	4.10 ^{+0.47} _{-0.39}	3.93 ^{+0.98} _{-0.70}	0.96 ^{+0.26} _{-0.19}	0.41 ^{+0.24} _{-0.20}	0.95	1.08	84
RX J2129.6+0005	70	489	4.30	6.01 ^{+0.55} _{-0.46}	7.19 ^{+1.68} _{-1.21}	1.20 ^{+0.30} _{-0.22}	0.51 ^{+0.16} _{-0.15}	1.29	1.34	87
S0463 *	70	307	1.06	3.26 ^{+0.33} _{-0.38}	3.92 ^{+1.16} _{-0.94}	1.20 ^{+0.38} _{-0.32}	0.23 ^{+0.18} _{-0.15}	1.08	1.08	54
TRIANG AUSTR	71	539	13.27	8.50 ^{+0.29} _{-0.25}	12.08 ^{+1.13} _{-1.13}	1.42 ^{+0.14} _{-0.14}	0.03 ^{+0.04} _{-0.03}	0.01	1.93	83
V 1121.0+2327	70	315	1.30	4.17 ^{+0.78} _{-1.17}	4.70 ^{+3.00} _{-1.17}	1.13 ^{+0.75} _{-0.32}	0.46 ^{+0.36} _{-0.28}	1.09	0.87	74
ZWCL 1215	70	277	1.76	6.64 ^{+0.46} _{-0.38}	8.69 ^{+0.74} _{-0.80}	1.31 ^{+0.14} _{-0.14}	0.37 ^{+0.11} _{-0.11}	1.10	1.03	91
ZWCL 1358+6245	70	391	1.94	9.70 ^{+1.16} _{-0.94}	9.04 ^{+2.09} _{-1.46}	0.93 ^{+0.24} _{-0.18}	0.57 ^{+0.19} _{-0.19}	1.03	0.90	65
ZWCL 1953	69	516	3.10	8.28 ^{+1.22} _{-0.96}	11.83 ^{+4.01} _{-2.55}	1.43 ^{+0.53} _{-0.35}	0.21 ^{+0.14} _{-0.15}	0.87	0.77	82
ZWCL 3146	70	512	2.70	7.46 ^{+0.32} _{-0.30}	8.99 ^{+0.94} _{-0.78}	1.21 ^{+0.14} _{-0.12}	0.31 ^{+0.06} _{-0.05}	1.06	0.97	91
ZWCL 5247	70	449	1.70	4.89 ^{+0.86} _{-0.65}	4.39 ^{+2.40} _{-1.21}	0.90 ^{+0.50} _{-0.27}	0.37 ^{+0.30} _{-0.25}	1.09	0.93	78
ZWCL 7160	69	451	3.10	4.63 ^{+0.42} _{-0.36}	5.41 ^{+1.06} _{-0.80}	1.17 ^{+0.25} _{-0.20}	0.36 ^{+0.14} _{-0.14}	0.94	0.95	87
ZWICKY 2701	69	315	0.83	5.08 ^{+0.32} _{-0.30}	4.96 ^{+0.87} _{-0.69}	0.98 ^{+0.18} _{-0.15}	0.45 ^{+0.13} _{-0.11}	0.95	0.76	70
ZwCL 1332.8+5043	70	453	1.10	3.82 ^{+3.34} _{-1.42}	2.86 ^{+3.96} _{-1.21}	0.75 ^{+1.23} _{-0.42}	0.16 ^{+4.75} _{-0.16}	0.71	0.95	60
ZwCL 0848.5+3341	71	365	1.12	6.54 ^{+2.04} _{-1.27}	6.41 ^{+3.79} _{-1.88}	0.98 ^{+0.66} _{-0.34}	0.59 ^{+0.59} _{-0.48}	0.89	1.01	47

NOTE. — Note: “77” refers to 0.7-7.0 keV band and “27” refers to 2.0-7.0 keV band. (1) Cluster name, (2) size of excluded core region in kpc, (3) R_{5000} in kpc, (4) absorbing Galactic neutral hydrogen column density, (5,6) best-fit MEKAL temperatures, (7) $T_{0.7-7.0}/T_{2.0-7.0}$ also called T_{HBR} , (8) best-fit 77 MEKAL abundance, (9,10) respective reduced χ^2 statistics, and (11) percent of emission attributable to source. A star (*) indicates a cluster which has multiple observations. Each observation has an independent spectrum extracted along with an associated WARF, WRMF, normalized background spectrum, and soft residual. Each independent spectrum is then fit simultaneously with the same spectral model to produce the final fit.